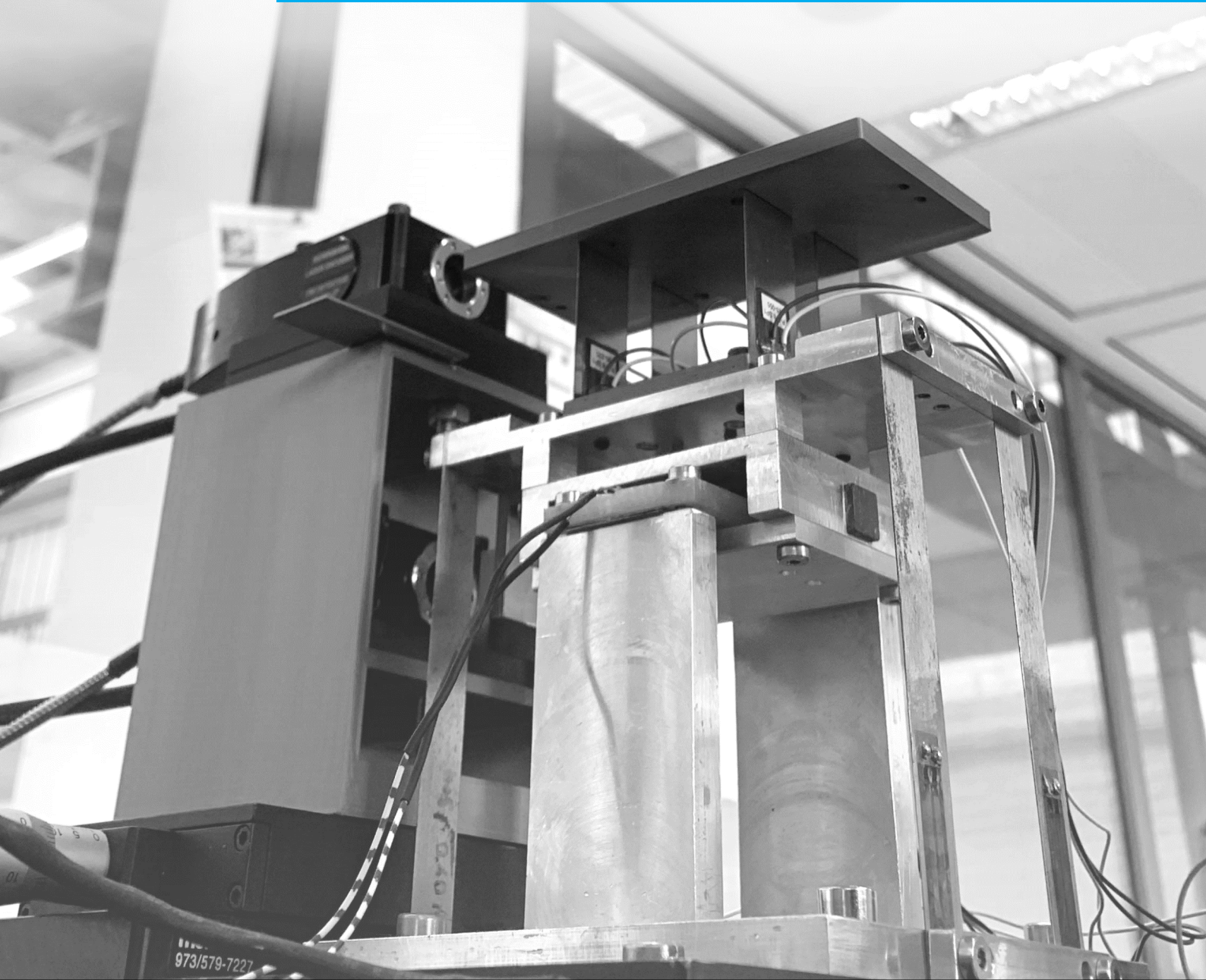


Department of Precision and Microsystems Engineering

Active Damping Control of Higher-Order Resonance Mode in Positioning Systems

Niels Dee

Report no : 2024.093
Coach : Ir. A.M. Natu
Professor : Dr. S.H. HosseinNia Kani
Specialisation : Mechatronic System Design
Type of report : Master Thesis
Date : 22 October 2024



Active Damping Control of Higher-Order Resonance Mode in Positioning Systems

Master Thesis

by

Niels Dee

to obtain the degree of Master of Science
at the Delft University of Technology,
to be defended publicly on Tuesday October 22, 2024 at 13:00.

Student number: 4952294
Thesis committee: Dr. Hassan HosseinNia Kani, Supervisor
Ir. Aditya Natu, Daily Supervisor
Dr. Hans Goosen
Dr. Mohammad Khosravi

This thesis is confidential and cannot be made public until December 31, 2025.

An electronic version of this thesis is available at <http://repository.tudelft.nl/>.

Abstract

There is an ever-increasing demand for faster and more accurate motion stages in the high-tech industry. In precision positioning systems, lightly damped higher-order resonance modes can induce undesirable vibrations that degrade system performance and accuracy. These resonances pose additional challenges in non-collocated dual-stage positioning systems, where they significantly limit control bandwidth. Although conventional notch filters are commonly used alongside tracking controllers to enhance bandwidth, they lack robustness when faced with system parameter uncertainties. Moreover, the effects of the parasitic resonance on disturbance rejection remain. Active damping control has been successfully used to mitigate issues related to the primary resonance mode, but its application to higher-order parasitic modes has not been explored. This research introduces a novel control strategy, High-Pass Positive Position Feedback (HP-PPF), designed specifically for the active damping of higher-order, non-collocated parasitic modes in positioning systems. The proposed method incorporates a second-order high-pass filter within a positive feedback loop, effectively attenuating the parasitic resonance. Integrated with a PID tracking controller in a dual-loop configuration, this method enhances disturbance rejection, noise suppression, and robustness against model uncertainties, overcoming limitations of traditional notch filter-based methods while maintaining comparable tracking performance. The proposed control architecture is validated through a proof-of-concept experimental setup that demonstrates the effectiveness of the underlying mathematical framework.

Contents

Abstract	i
1 Introduction	1
1.1 Background	1
1.2 Motivation and Problem Statement	2
1.3 State-of-the-Art	3
1.3.1 Feedback and Feedforward Control of Motion Systems	3
1.3.2 Structural-based Damping	4
1.3.3 Active Damping Control of Parasitic Resonances	4
1.4 Research Objectives	8
1.5 Thesis Outline	9
2 Literature Preliminaries	10
2.1 Dynamics	10
2.2 Collocation and Non-collocation	12
2.3 Spillover	13
2.4 Active Damping Control	13
2.4.1 Loop shaping	14
2.4.2 Active Damping Control Algorithms	15
2.4.3 Active Damping Control Table Overview	24
2.5 Motion Control	26
2.5.1 Closed-loop performance measures	26
2.5.2 Resonance Limiting Control Bandwidth	27
2.5.3 Notch Filters	27
2.6 Motion Control and Active Damping Control	28
3 Active Damping Control of Higher-Order Resonance Mode in Positioning Systems	30
4 Results & Discussion	49
4.1 Stability of Inner HP-PPF Active Damping Loop	49
4.1.1 Attenuating Feedback Noise using Band-Pass Filter	51
4.2 Closed-Loop Disturbance Rejection	52
4.2.1 Case Study: Floor Vibration Disturbances	53
4.3 Real Error Contributions	54
4.4 Exploration of Non-minimum Phase Filters	56
5 Conclusions & Recommendations	59
5.1 Conclusions	59
5.2 Recommendations	60
References	61
A	69
A.1 Experimental Setup	69
A.2 LabVIEW Project	70
A.2.1 FPGA.vi	70
A.2.2 RT_Main.VI	73
A.2.3 Host.VI	76
A.3 System Identification	77
B Optimization Algorithm	80

Introduction

1.1. Background

Moore's Law, formulated by Gordon Moore in 1965, has become a guiding principle in the field of high-tech engineering. Moore predicted that the number of transistors on a microchip would double approximately every two years, leading to exponential growth in computational power and efficiency [1].

While it is important to note that Moore's Law is not physical or mathematical, the concept describes the rapid progress and evolution of computing technology. As the density of transistors increases, so does the need for more advanced machinery capable of producing these microchips. There is an ever-increasing demand for faster and more accurate high-precision positioning systems, such as those used in lithography machines produced by ASML [2–5]. Figure 1.1 gives an impression of the reticle and wafer stage used for lithography in the ASML machines, critical positioning stages that require extreme positioning accuracy, precision and speed.

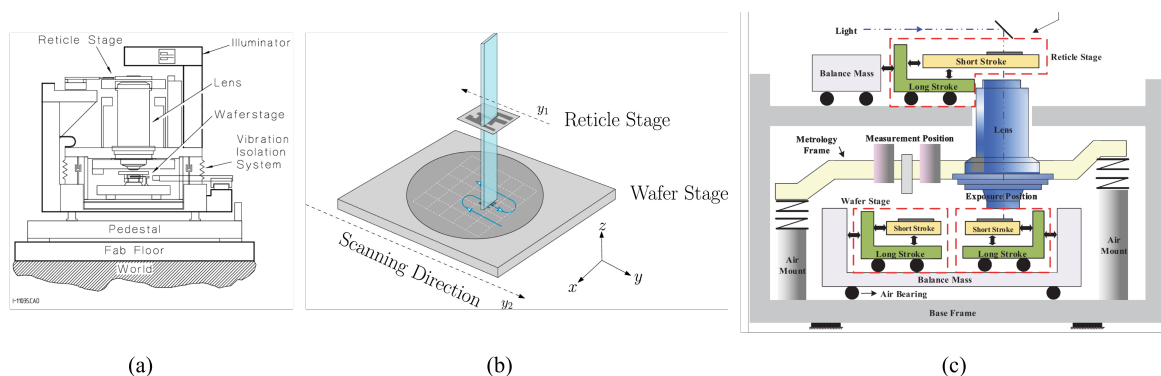


Figure 1.1: Impression of wafer scanner stages used in lithography machines (a) [3] (b) [4] (c) [5].

This drive for increased performance extends beyond the semiconductor industry, encompassing diverse high-precision applications like scanning-probe microscopy [6, 7], micromanipulators [8–10], nanomanufacturing [11], precision optics [12, 13] and precision pick-and-place machines [14].

These systems often require up to nanometer-level positioning accuracy, high response speed, compact designs, and large travel ranges [15]. The performance of the positioning stages is directly influenced by the bandwidth of the driving control architecture, with higher bandwidth yielding greater speed and accuracy [16–18]. Moreover, vibrations present in the system degrade the positioning accuracy. As a result, enhancing performance involves continuously pushing the control bandwidth of these positioning systems to the stability limits while minimizing the impact of vibrations.

1.2. Motivation and Problem Statement

To capture the predominant dynamics of positioning systems, they are often analytically simplified into mass-spring-damper models. Typically, higher-order modes are assumed to be sufficiently distant to be negligible and unlikely to induce vibrations or errors. However, in systems with flexure-based guiding mechanisms, these higher-order modes can occur at relatively low frequencies, close to the rigid-body mode, and may lead to errors when excited. In high-precision applications, compliant flexures are commonly employed to mitigate issues like friction, hysteresis, and micro-slip, which can otherwise cause significant inaccuracies [19, 20]. To minimize stress concentrations and resistance, flexures are designed with low structural stiffness, which results in very low damping and lightly damped vibration modes at relatively low frequencies [21, 22]. When excited by high-frequency reference or disturbance signals, these higher-order modes generate unwanted vibrations that degrade positioning accuracy [18, 23].

In industrial applications like dual-stage positioning systems, such as dual wafer stages and reticle stages used in lithography machines [5], these higher-order modes pose an even more significant challenge. These systems, typically operating in Single-Input Single-Output (SISO) configurations with a single actuator and sensor, are approximated by fourth-order dynamics, dominated by two primary modes. The double-mass-spring-damper system, shown in Figure 1.2, effectively models these two dominant resonance modes, capturing the essential dynamics of single-axis dual-stage positioning systems. Due to the often complex geometries of these systems, a mechanical connection between the actuated base stage and the end-effector leads to non-collocated dynamics. The position of the end-effector (x_2) is controlled by actuating the base stage (m_1), representing this non-collocated actuator-sensor configuration (x_2/F_a). The second resonance peak in the frequency response, illustrated in Figure 1.3, corresponds to the resonance mode related to the connection between the base stage and the end-effector (m_2). The minimum phase behaviour of this non-collocated parasitic mode induces a phase drop beyond -180° , which, in addition to causing unwanted vibrations, also restricts the control bandwidth of the positioning system to only a small fraction of the parasitic mode [24, 25].

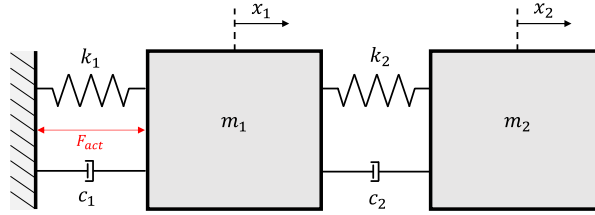


Figure 1.2: Analytical double-mass-spring-damper representation

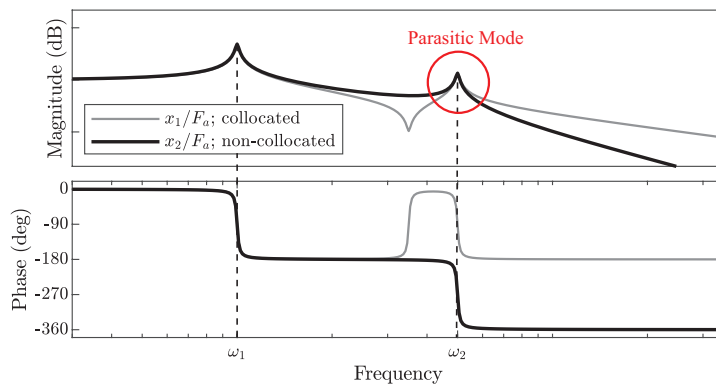


Figure 1.3: General non-collocated (x_2/F_a) and collocated (x_1/F_a) frequency response of single-axis positioning systems represented by double-mass-spring damper model

Overall, the presence of higher-order resonance modes introduces unwanted vibrations, limiting positioning accuracy. In non-collocated dual-stage systems, these higher-order resonances impose further constraints on control bandwidth, significantly restricting the overall performance of these positioning systems.

Improving the performance of high-precision positioning systems offers meaningful industrial, societal, and economic benefits. In the semiconductor industry, enhanced positioning accuracy and speed in lithography machines directly translates into increased manufacturing efficiency and higher throughput, enabling the production of more powerful and energy-efficient microchips [26]. This improvement facilitates advancements in technologies like artificial intelligence, 5G, and quantum computing, which have significant implications for industries ranging from healthcare [27] to communications [28]. In addition to semiconductors, advancements in precision systems influence a wide range of applications, including medical devices [29, 30], robotics [31], and renewable energy technologies [32], thereby driving innovation across these sectors.

1.3. State-of-the-Art

The previous section outlined the challenges posed by higher-order dynamics in positioning systems, which can appear at relatively low frequencies, emphasizing the need to address these issues. This section will provide a brief overview and analysis of the strategies used in existing literature to deal with these challenges.

1.3.1. Feedback and Feedforward Control of Motion Systems

Depicted in Figure 1.4, is a block diagram of a general motion control architecture, involving both feedforward and feedback control. The A/D and D/A converters translate analogue signals into time-discrete signals and vice versa, as they are almost always used in motion control systems in industry. Several disturbances on the control loop are indicated as well, which play a large role in determining what requirements the controllers need to fulfil. A typical feedback controller for motion control often employs a PID controller, which can be designed to enhance the robustness and stabilization of the system [33].

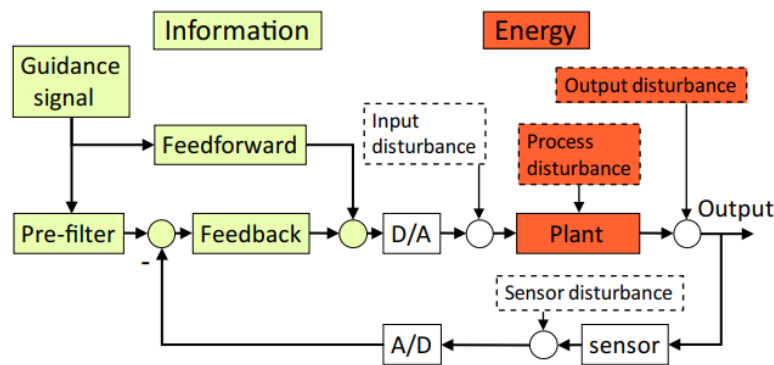


Figure 1.4: Block diagram of general motion control system [33]

Feedforward control offers notable benefits, such as compensating for known disturbances, but it requires the plant to be stable and may lead to instability if applied to a non-minimum phase plant [33]. Various techniques, including feedforward [17, 34], input shaping [35], inversion [36], and notch filters [37–39], have been successfully combined with conventional PID controllers to address parasitic resonances. However, these methods, while effective in systems with precise models and known disturbances, may lack robustness when faced with parameter uncertainties and external disturbances [25, 40]. Feedforward methods rely on a predefined system model, in the case of a notch filter to precisely place the filter at the frequency of the parasitic resonance mode. If the actual resonance mode deviates from this model, notching performance can significantly degrade, limiting the control bandwidth and potentially leading to instability. This poses significant challenges in applications where there are uncertainties in the system model or, for instance, when the load mass of the end-effector varies during operation, affecting the respective resonance frequency. Moreover, while notch filters can increase control bandwidth by attenuating the resonance, the effect of this parasitic vibration mode is still observed in closed-loop disturbance rejection performance [25].

Because of their sensitivity to uncertainties, inversion-based controllers are typically limited to niche applications where the resonance frequency remains stable, or where continuous re-calibration of the controller is feasible [41].

1.3.2. Structural-based Damping

A common engineering strategy for addressing resonance modes is to shift the problematic resonance to a higher frequency by modifying structural properties like stiffness and mass. This adjustment aims to achieve a larger control and reduce vibrations induced by the mode. The process involves modifying either the modal mass or modal stiffness of the specific mode [23], which is referred to as *de-tuning* [42]. Another method is to move the sensitive part of a mechanical structure towards a node of the harmful vibration mode (or vice versa) [23], which is referred to as *nodalising* [42]. However, strict constraints on workspace dimension, mass and parasitic motion generally limit the design freedom. Rather than physically shifting the parasitic mode to higher frequencies, an alternative strategy is to introduce additional damping characteristics to the undesired mode. This approach includes both structural modifications (passive damping) and controller-based solutions (active damping).

Damping in mechanical systems involves dissipating vibrational energy to reduce resonance peaks in the frequency responses. Adding damping can be done by using highly damped materials, such as polymers, or by increasing friction or viscous damping. However, friction is often a significant source of inaccuracy, which is why high-precision machinery is usually designed to minimize friction, resulting in low damping characteristics [23]. Constrained Layer Damping (CLD) [43] is a frequently employed passive damping technique in which a viscoelastic material is placed between two rigid sheets, serving as a vibration damper, illustrated in Figure 1.5.a. Rather than complete structural re-design, in some situations, the simplest way to reduce vibrations is to introduce a single mass, a stiffener, or a combination of both ('vibration absorber') attached to a specific point of the structure [23]. Such a vibration absorber, referred to as a tuned mass damper (TMD), should be carefully tuned to match the resonance of the structure, which results in true absorption of the vibration rather than damping [44]. A TMD configuration for a flexure is illustrated in Figure 1.5.b. In general, passive damping methods do not require any external energy source or sensors, which makes them simple to implement. Though being effective for high-frequency vibration suppression and single resonance frequency damping, passive methods are not well-suited for broad-range frequency suppression. To dampen multiple modes, multiple CLDs or TMDs are required. Moreover, in high-precision positioning systems minimizing mass is a crucial design objective, making the addition of mass for damping purposes in practice an unsuitable solution.

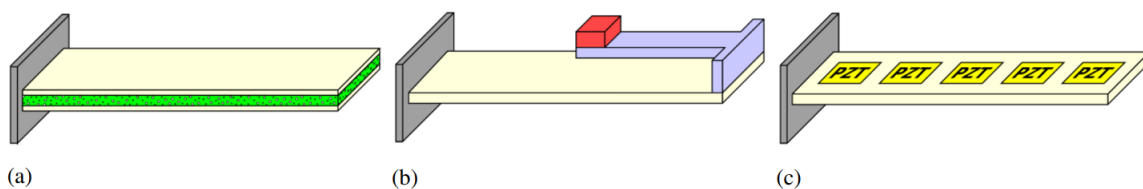


Figure 1.5: Schematic overview of different damping methods (a) Constrained Layer Damping; (b) Tuned Mass Damper; (c) PZT Active Damping Control [45]

1.3.3. Active Damping Control of Parasitic Resonances

An alternative approach involves mitigating the effects of resonance modes through active damping control, which employs feedback compensators to actively control resonant modes. Controlling these modes through feedback is especially appealing since it requires no adaptation time or reference signal. While it requires sensors, control systems, and an external energy source, this implies that the dissipation of energy occurs outside the system, enabling the activation of damping whenever necessary. Piezoelectric Transducers (PZT) are commonly employed to realize active damping, as illustrated in Figure 1.5.c. Active damping can effectively dampen multiple vibration modes while contributing significantly less mass to the overall structure compared to passive methods. Moreover, it often achieves superior damping performance, facilitates easy tuning of the damping and the impact of variations in system parameters can be reduced through sensitivity reduction [46].

The major aspects of feedback and feedforward control of vibration modes are summarized in Figure 1.6 [34]. Active damping controllers within feedback loops are commonly employed to address the damping of parasitic resonance modes in motion control systems, to reduce vibrations and improve bandwidth. These fixed-structure controllers are designed to be inherently robust and easy to tune, using general knowledge of the dynamics of a plant [46, 47]. This makes implementation relatively easy compared to model-based and feedforward alternatives.

Type of Control	Advantage	Disadvantage
Feedback		
Active damping	<ul style="list-style-type: none"> • Simple to implement and requires fewer computation • Does not require accurate model of the plant • Guaranteed stability when actuators and sensors are collocated 	<ul style="list-style-type: none"> • Effective only near resonance
Model Based (LQG, H_∞ , ...)	<ul style="list-style-type: none"> • Global method • Requires accurate model of the plant • Attenuates all disturbance within the control bandwidth 	<ul style="list-style-type: none"> • Limited bandwidth • Requires low delay for wide bandwidth • Spillover
Feedforward		
Adaptive filtering of reference (x-filtered LMS)	<ul style="list-style-type: none"> • No model is necessary • Robust to inaccuracies in plant estimate and to change in plant transfer functions • More effective for narrowband disturbance 	<ul style="list-style-type: none"> • Reference/error signal is required • Local method and may amplify vibration somewhere else • Large amount of real-time computations

Figure 1.6: Comparison of vibration control strategies as presented in [34]

Commonly employed active damping controllers include direct velocity feedback (DVF) [48], integral resonance control (IRC) [49], integral force feedback (IFF) [50], negative position feedback (NPF) [51], positive position feedback (PPF) [52], positive velocity and position feedback (PVPF) [53], and positive acceleration, velocity and position feedback (PAVPF) [54]. Among these, PPF, PVPF, and PAVPF are widely adopted due to their ease of implementation, effective roll-off characteristics, ability to suppress multiple modes [55], and robustness against parameter variations [56].

Parasitic resonance modes not only induce unwanted vibrations but also limit the control bandwidth in many applications. Therefore, the remainder of this section focuses on the application of active damping control in motion systems, where active damping controllers are commonly combined with tracking controllers. This section distinguishes between active damping controllers used to target the first resonance mode, analytically characterized by an inherently collocated second-order transfer function, and those applied to dampen the primary higher-order non-collocated resonance mode, characterized by the fourth-order dynamics. Different solutions consist of Single-Input-Single-Output (SISO) configurations, utilizing a single actuator and sensor for both motion and damping control and Multiple-Input-Multiple-Output (MIMO) where additional sensor and/or actuators are added to provide active damping control. Figure 1.7 provides an overview of different control architectures to combine motion control (MC) and active damping control (ADC).

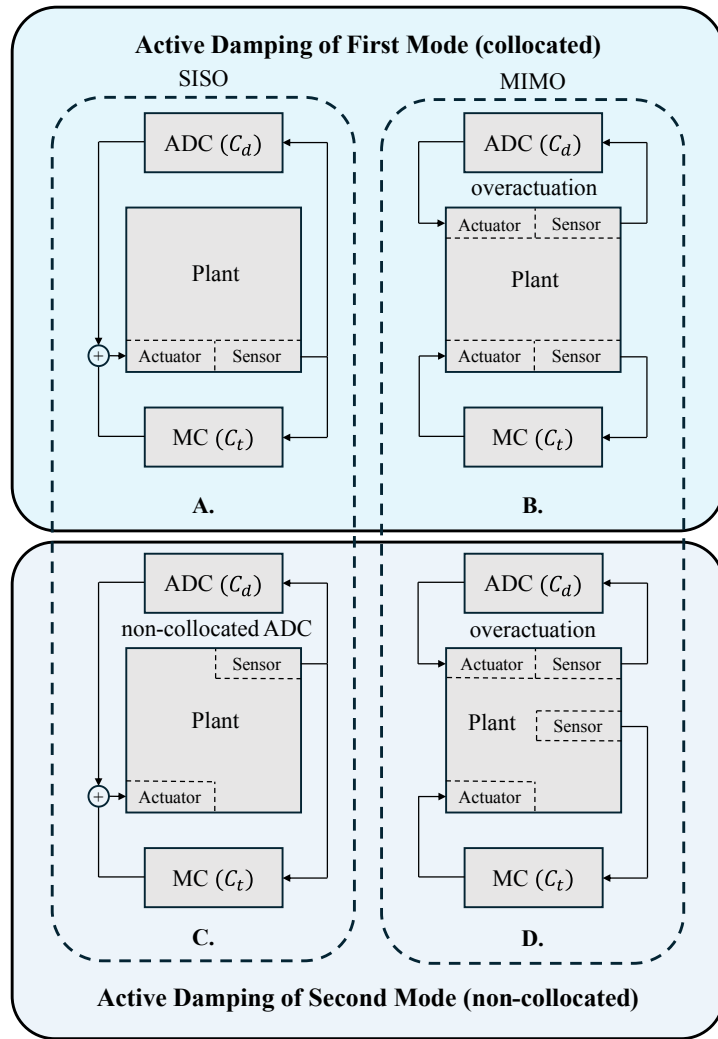


Figure 1.7: Active damping and motion control architectures, where active damping is targeted at first resonance (A., B.) and where active damping is targeted at higher-order non-collocated mode, i.e. second mode (C., D.)

Active Damping of First Mode

The configuration in Figure 1.7.A represents the most common motion control architecture where active damping control is implemented. In this setup, the active damping controller specifically targets the primary resonance mode, which can be analytically described by a second-order transfer function. This system inherently exhibits a collocated relationship between the sensor and actuator due to the single body involved in the simplified model. In certain applications, this primary resonance mode is the limiting factor for control bandwidth. To achieve both damping and tracking control with a single actuator and sensor (SISO), a dual-loop control architecture is often employed [57, 58]. This approach integrates motion control and active damping control, as shown in Figure 1.8.

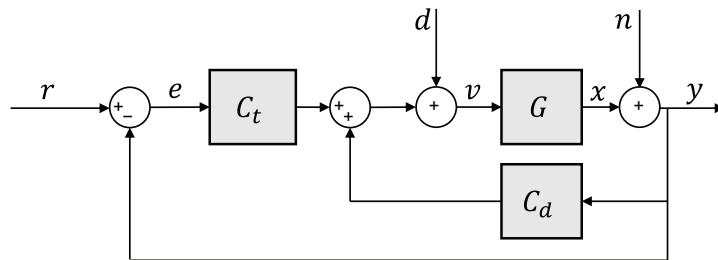


Figure 1.8: Generalized SISO dual-loop control architecture for tracking and active damping control

An IRC damping controller with integral tracking control is applied to a scanning probe microscope in [59]. Greater than ten times improvement in tracking bandwidth is demonstrated with experimental results. The IRC method is also applied on a nanopositioning stage in [60] in combination with feedforward inversion control. In [61, 62] IFF is applied to enhance control bandwidth and is experimentally validated for its application in a nanopositioner model in [50]. Optimal IFF with a feedthrough term is applied in [63] to improve tracking control for the application in objective lens positioners. In [64] a PPF damping control and proportional-integral (PI) tracking control is presented for a piezoelectric tube scanning AFM. Experimental results showed significant scanning-image quality improvement with the addition of PPF damping control. Besides positioning systems, the PPF controller is also used for vibration control in thin beam and plate-like structures [65, 66]. In [67] a PVPF damping controller is used to increase motion control bandwidth, which resulted in better tracking performance for a nanopositioning stage. In [68] a PAVPF damping controller with PI tracking controller for broadband control of a piezo-actuated nanopositioning stage is used to improve control bandwidth. However, PPF and PVPF require collocated actuator-sensor configurations, as they are designed specifically for second-order systems [57]. Third-order models, which better represent the dynamics of nanopositioning stages [69, 70], have led to the development of the PAVPF damping controller, proven effective in enhancing bandwidth when combined with tracking control [57, 58].

In [71], an additional actuator and sensor are integrated into the control loop to implement active damping, resulting in an architecture as shown in Figure 1.7.B. This configuration enables independent operation of both controllers, following the high authority/low authority control (HAC-LAC) approach. In this scheme, the low authority control (LAC) handles active damping, while the high authority control (HAC) is dedicated to motion control [24, 72].

Active Damping of Higher-Order (non-collocated) Mode

As previously highlighted, also higher-order modes can introduce unwanted vibrations when they occur at relatively low frequencies. Moreover, in dual-stage positioning systems, the higher-order non-collocated mode poses limitations on the control bandwidth, rather than the primary resonance mode.

In modal control, the dynamics of systems with dominating higher-order modes can be decomposed in modal signals in the modal domain, which enables the application of existing active damping control methods similar to the approach used for controlling a single DOF oscillator [73]. However, modal control techniques rely on accurate models of the system's modal properties, such as natural frequencies and mode shapes. If the system is not perfectly modelled, or if there are changes in system dynamics the controller's performance can degrade significantly [74, 75]. Additionally, when modes are closely spaced, it becomes challenging to isolate and control specific modes, which can lead to unintentionally exciting other modes [76]. In modal control, it is often assumed that modes are well separated [73], a condition that may not always hold in practice. The approach also requires precise placement of sensors and actuators to effectively target specific modes, which poses difficulties in systems with complex geometries or strict design requirements.

In [25] the concept of overactuation —using more actuators than the number of rigid body modes to be controlled [77]— is applied to target the higher-order parasitic mode in a motion system. The damping controller is implemented in an isolated inner feedback loop to achieve collocated active damping control in a non-collocated motion control loop. This approach involves adding (multiple) collocated piezoelectric actuator/sensor pairs for active damping to the structure, as schematically illustrated in the block scheme in Figure 1.7.D and Figure 1.9. Despite the non-collocated nature of motion control dynamics in the presented application, conventional active vibration control techniques, relying on collocated dynamics, can still be effectively applied through overactuation by introducing a collocated actuator-sensor pair. The proposed methodology in [25], employing positive position feedback to reduce the parasitic resonant mode, allowed for a higher control bandwidth and improved disturbance rejection. Moreover, increasing the number of active actuators enhances the damping performance, resulting in greater suppression of the targeted resonance peak.

However, this overactuation approach requires the addition of extra sensors and actuators, which may not always be practical or desirable in real-world applications. This limitation restricts the solution to only specific cases where additional piezo patches can be integrated. Furthermore, it complicates the control architecture by creating a MIMO system, where managing cross-coupling effects between controllers can be challenging, thus making the overall controller design more difficult.

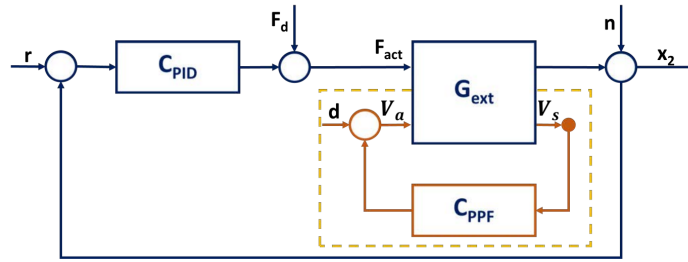


Figure 1.9: Control architecture implementing active damping control using overactuation [25].

In contrast, implementing active damping control within the tracking control loop as shown in the dual-loop architecture in Figure 1.8 and Figure 1.7.C, enables the use of the same sensor and actuator already employed for tracking control, thereby maintaining a straightforward SISO configuration. This approach allows for the direct integration of the active damping controller without the need for structural modifications, such as adding actuator-sensor pairs, to the system. However, at present, no generally applicable active damping control strategy specifically addresses higher-order parasitic resonance modes, which limit positioning accuracy and, in certain applications, even tracking control bandwidth.

1.4. Research Objectives

The previous section highlighted the advantages of active damping control over inversion techniques, such as notch filters, and model-based methods. While active damping is commonly used to improve the damping of a system's primary mode, reducing vibrations and enabling higher control bandwidth when combined with tracking control in nanopositioning applications, it has yet to be applied to higher-order, non-collocated parasitic modes. These higher-order vibration modes typically limit positioning accuracy, and in dual-stage positioning systems with fourth-order non-collocated dynamics, they impose additional constraints on control bandwidth. This underscores the need for active damping of these higher-order undesired modes. This research gap forms the foundation of the scientific contribution of this thesis. Accordingly, the general research question is formulated as follows:

How can active damping control be extended to higher-order modes of positioning systems to enhance damping and motion performance?

To address this research question, this thesis proposes a novel fixed-structure controller approach for active damping of the first dominant higher-order mode in positioning systems while preserving the simplicity of a SISO configuration. The primary focus of this work is on the non-collocated higher-order parasitic mode in dual-stage positioning systems, as it imposes an additional constraint on control bandwidth. However, it is important to emphasize that the general framework of the proposed solution can be applied to achieve active damping of any higher-order mode that introduces unwanted vibrations in positioning systems. The key contributions of this work are as follows:

1. This research provides a general solution for active damping of higher-order parasitic modes, enhancing disturbance rejection and noise suppression at those frequencies.
2. The novel active damping control method enhances control bandwidth when combined with conventional tracking controllers in dual-stage positioning systems, achieving comparable tracking performance to a notch filter-based method.
3. The proposed solution demonstrates robust performance against model uncertainties, particularly concerning resonance frequency variations within a defined range, offering significant improvements in robustness compared to a notch filter-based method.

The research objectives outlined below aim to provide a comprehensive demonstration, encompassing both mathematical and experimental aspects, of the contributions made by this work.

1. Develop a fixed-structure controller for active damping control of a higher-order non-collocated mode.

- Demonstrate its effectiveness in attenuating the parasitic mode with numerical simulations.
 - Numerically evaluate the performance of the novel controller against that of state-of-the-art methods, such as notch filters, in both frequency and time domains.
 - Develop a generalized mathematical framework to demonstrate the work contributions.
2. Experimentally validate the contributions as a proof-of-concept.
 - Adjust the experimental setup and LabVIEW architecture from [78] to allow for the implementation of the proposed active damping control.
 - Perform accurate system identification of the setup to determine control parameters.
 - Implement real-time digital closed-loop control and conduct measurements to experimentally validate contributions.

1.5. Thesis Outline

The remainder of the thesis report is outlined as follows:

- Chapter 2 presents a summarized literature review, covering key concepts and foundational knowledge required to understand the research conducted in this thesis.
- Chapter 3 contains the main research contributions, presented in the format of a scientific journal paper.
- Chapter 4 provides a more in-depth discussion of some of the key results obtained during the research.
- Chapter 5 summarizes the research findings and offers recommendations for future work in this field.

2

Literature Preliminaries

This chapter provides a comprehensive overview of the fundamental concepts and preliminary knowledge from the literature that are essential for understanding the research presented in this thesis. It includes a detailed examination of existing active vibration control techniques used to improve damping characteristics of resonance modes.

2.1. Dynamics

Mechanical structures are defined by their mass, stiffness, and damping properties, which vary with dimensions and materials. These properties create an infinite number of degrees of freedom (DOFs) and vibration modes in the dynamic behaviour [23]. To describe a structure's dynamic response fully would be computationally impractical, so it is often approximated by a finite number of flexible modes that adequately capture its behaviour.

A common and efficient method for approximating the dynamic response of flexible structures is modal coordinates. Modal control involves extracting and controlling target mode signals in the modal domain, in a similar way to controlling a single DOF oscillator. This approach simplifies controller design, enables global vibration reduction through local feedback at discrete positions, and is robust to uncontrolled modes. Modal control can be applied regardless of whether sensors and actuators are collocated or non-collocated [73]. Thus, the dynamics of a flexible structure can be approximated by summing N single DOF modes.

$$G = \sum_{i=1}^N \frac{k_i}{s^2 + 2\zeta_i\omega_i s + \omega_i^2} + R \quad (2.1)$$

Here k_i , ζ_i and ω_i represent the modal displacement constant of the corresponding mode, the damping ratio and eigenfrequency, respectively. A constant feedthrough term R can be added to account for the influence of truncated modes at higher frequencies [24]. When the first resonance is dominant and higher-order modes are sufficiently distant from the first mode [79], the dynamics can be represented by a damped single mass-spring system, as shown in Figure 2.1, representing the single DOF mode. This representation is used, for instance, to characterize the dynamics of flexure-based nanopositioning stages [67, 80], flexible manipulators [81], disc-drive actuators [82], high-density memory storage devices [53], and more [79].

However, in the application of precision mechatronic systems, performance limitations often arise as a result of parasitic dynamics of higher-order modes that also occur at relatively low frequencies. Modal decomposition into separate single DOF modes presents its own challenges, as previously discussed. This highlights the need for an analytical representation that incorporates higher-order modes in addition to the primary resonant mode. The predominant system dynamics can be therefore be represented by a collocated or non-collocated double mass-spring-damper system [16], schematically illustrated in Figure 2.2. This effectively represents the behaviour of the system's first two modes of interest.

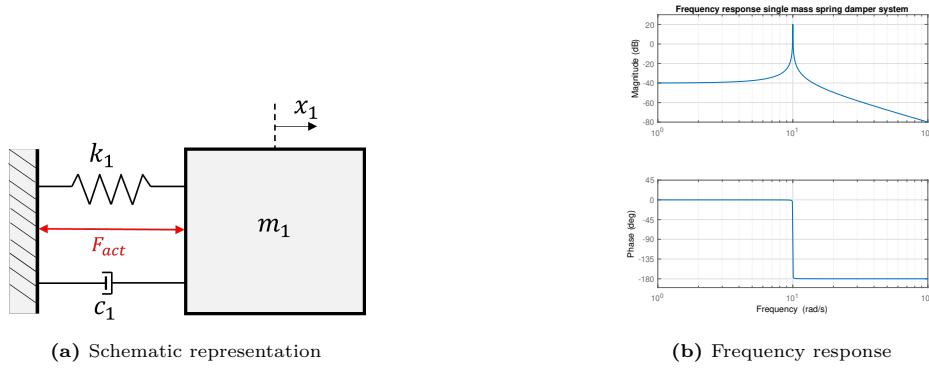


Figure 2.1: Single mass-spring-damper system

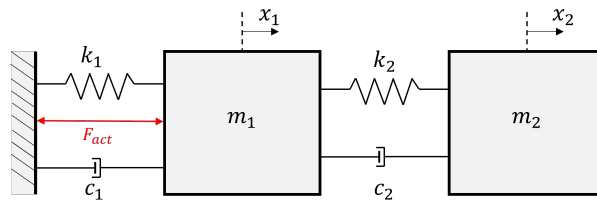


Figure 2.2: Schematic of a double mass-spring-damper system

The system has two position outputs, x_1 and x_2 , that both can be measured and used for feedback. Placing the sensor at the first mass (m_1) results in a collocated transfer function, Equation (2.2).a, while sensing at the second mass (m_2), results in a non-collocated transfer function, Equation (2.2).b. The frequency responses of both collocated and non-collocated transfer functions are depicted in Figure 2.3a and Figure 2.3b respectively.

$$G_{col} = \frac{x_1}{F} = \frac{m_2 s^2 + c_2 s + k_2}{(m_2 s^2 + c_2 s + k_2) [m_1 s^2 + (c_1 + c_2) s + (k_1 + k_2)] - (c_2 s + k_2)^2} \quad (2.2a)$$

$$G_{ncol} = \frac{x_2}{F} = \frac{c_2 s + k_2}{(m_2 s^2 + c_2 s + k_2) [m_1 s^2 + (c_1 + c_2) s + (k_1 + k_2)] - (c_2 s + k_2)^2} \quad (2.2b)$$

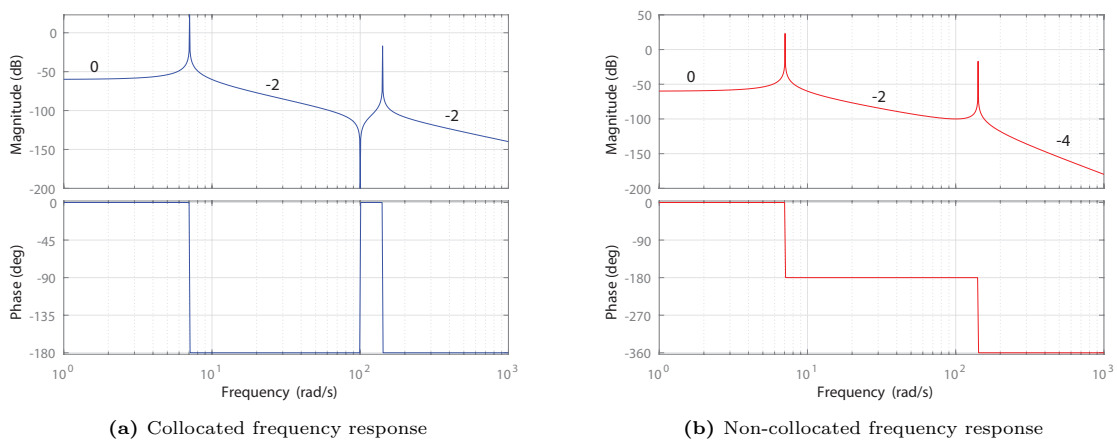


Figure 2.3: Frequency response of double mass-spring-damper system

The non-collocated transfer function in Equation (2.2).b can be expressed in general form, with unity gain at 0 Hz, as

$$G(s) = \frac{\omega_1^2 \omega_2^2}{(s^2 + 2\zeta_1 \omega_1 s + \omega_1^2)(s^2 + 2\zeta_2 \omega_2 s + \omega_2^2)} \quad (2.3)$$

where ω_1 and ω_2 are the resonance frequencies with corresponding damping ratios ζ_1 and ζ_2 respectively. Since this research focuses on the parasitic higher-order mode and its limitations on control bandwidth, the frequency range of interest can be simplified to include only this resonance, as shown in Figure 2.4a. Conceptually, this can be represented by a 'contactless' two-degree-of-freedom system, meaning no spring or damper connects the system to a fixed reference. This concept is illustrated in Figure 2.4b. This simplified system's frequency response is characterized by the generalized non-collocated transfer function in Equation (2.4).

$$G_p(s) = \frac{\omega_2^4}{s^2(s^2 + 2\zeta_2 \omega_2 s + \omega_2^2)} \quad (2.4)$$

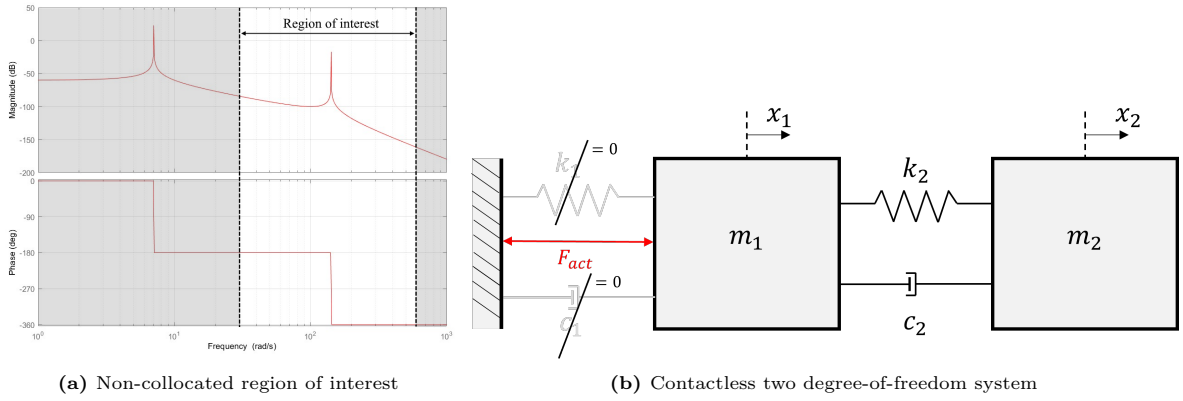


Figure 2.4: Simplification to parasitic higher-order resonance mode

2.2. Collocation and Non-collocation

The previous section already introduced the terms 'collocated' and 'non-collocated'. For a system to be collocated, both the actuator and sensor must be affixed to the same degree of freedom. Additionally, the sensor-actuator pair must be dual [24]. This means that the product of the actuator signal and the sensor signal should accurately reflect the energy exchange between the structure and the control system. Examples of this include a force actuator paired with a displacement sensor or a rotation sensor combined with a torque-providing actuator.

In an undamped collocated system, the open-loop FRF can be described by:

$$G = \sum_{i=1}^n \frac{\phi_i^2(k)}{\mu_i(\omega_i^2 - \omega^2)} + R_{kk} \quad (2.5)$$

where R_{kk} again represent the truncated modes, which in this case is a positive constant [24].

An important property of perfectly collocated systems is that they have alternating poles and zeros on the imaginary axis, referred to as pole-zero interlacing [24]. In the case that there is no damping present in the system, the poles and zeros lie perfectly on the imaginary axis, whereas in the case of light damping the poles and zeros move slightly into the left half plane, as can be seen in Figure 2.5.

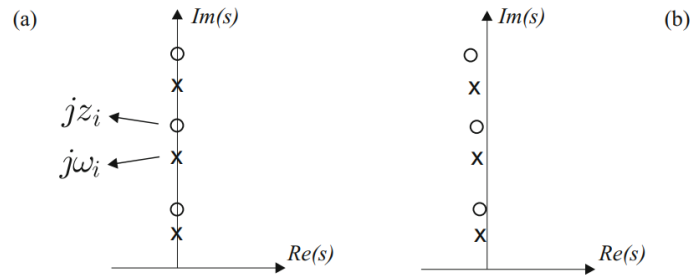


Figure 2.5: Pole-zero interlacing of an undamped collocated system (a) and a lightly damped collocated system (b) [24]

An imaginary pole introduces a 180° phase lag at the pole location and an imaginary zero a 180° phase lead at the zero location. The alternating pole-zero pattern therefore results in a phase response that is always contained between 0 and -180° . This guarantees the asymptotic robust stability of this collocated system, even if the system parameters are subject to big variations or disturbances. Furthermore, collocated systems are always closed-loop stable with respect to out-of-bandwidth dynamics [24], which is why most of the research focuses on collocation. However, for systems with time delays, this property does not hold and may lead to instability if neither the controller nor the system has high-frequency roll-off characteristics or if the system is not sufficiently damped [47].

As described before a perfectly collocated system exhibits pole-zero interlacing, a property that guarantees asymptotic robust stability. For a non-collocated system, this interlacing property does not exist and therefore robust stability cannot be guaranteed. In fact, the occurrence of pole-zero flipping, when the sequence of poles and zeros on the imaginary axis is reversed, results in a phase uncertainty of 360° . The frequency where interlacing stops and pole-zero flipping occurs decreases as the distance between the sensor and actuator, i.e. the non-collocation, increases [24].

Due to installation convenience or to achieve high degrees of observability and controllability, a non-collocated sensor/actuator configuration is often unavoidable [73].

2.3. Spillover

In practice, flexible structures possess an infinite number of modes, which necessitates the use of a reduced model for controller synthesis. However, the residual modes, that are beyond the controller's bandwidth and truncated in the model, can still influence the closed-loop response. This phenomenon is known as spillover and can be categorized into observation spillover and control spillover.

- Observation spillover takes place when sensor output signals are influenced by the measured response of residual modes.
- Control spillover occurs when residual modes are excited by the feedback control. Due to the intrinsic low damping of flexible structures, there is a danger that a feedback controller based on a reduced model destabilizes the residual modes [24].

The optimal performance of an active vibration controller would involve targeting a specific mode while leaving the response of all other modes unaffected. However, practical limitations arise due to spillover. Uncontrolled modes may experience changes in magnitude, and their resonance frequency can shift, posing challenges in tuning controllers for multimodal control. Additionally, the control action may lead to magnitude amplification in the quasi-static region of the closed-loop response [24]. The impact of spillover is heavily dependent on the chosen feedback control scheme.

2.4. Active Damping Control

Traditional optimal controller design techniques like LQG [83], H_2 [84], and H_∞ [85] are well-documented but can lead to high-order controllers with poor stability margins [49]. In contrast, controllers designed for collocated mechanical systems offer better robustness, performance, and easier implementation. This section reviews state-of-the-art active damping control techniques, known as fixed-structure controllers, which are inherently robust, easy to tune, and suitable for high-sample-rate hardware implementation [47, 80].

2.4.1. Loop shaping

The primary objective of active damping is to increase the negative real part of the system poles while maintaining the natural frequencies essentially unchanged. The effect of modifying the pole location on the frequency response is visualized in Figure 2.6.

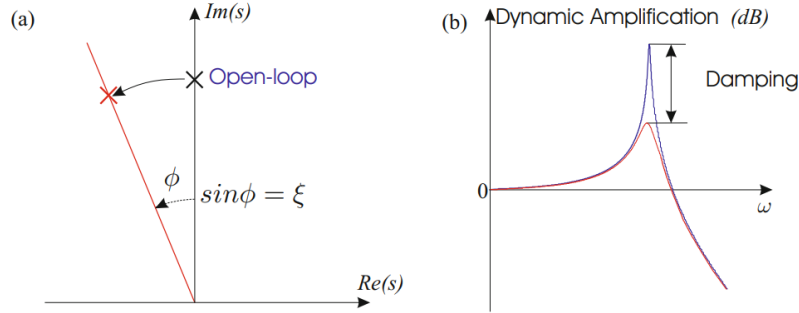


Figure 2.6: Role of damping on system poles (a) and frequency response (b) [24]

Often pole-zero maps, root-locus plots and pole placement are used to design active damping controllers. However, a more intuitive way to understand the objective of active damping is by considering the frequency domain. In [46] the advantage of loop-shaping in the frequency domain compared to pole placement and LQR control is presented. From a loop-shaping perspective, the objective of active vibration control in collocated systems can be described as a reduction in the amplitude of the sensitivity function [46]. In the frequency domain, this objective can be formulated by defining the desired shapes of the closed-loop and open-loop transfer functions. To define these transfer functions a general feedback control scheme, presented in Figure 2.7, is considered.

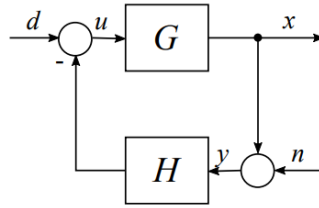


Figure 2.7: General feedback control loop used for active vibration control [47]

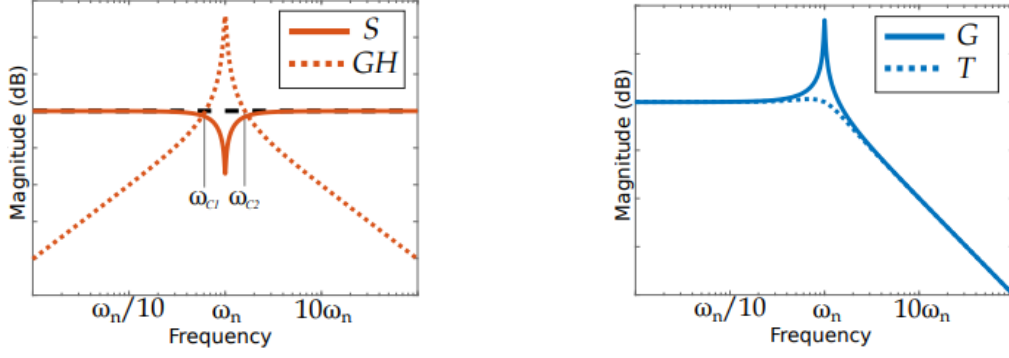
The closed-loop dynamics from disturbance d and noise n inputs to the performance output x and measurement y are given in Equation (2.6) [47]. Here G and H represent the system and controller transfer functions respectively.

$$S = \frac{y}{n} = \frac{1}{1 + GH} \quad (2.6a)$$

$$T_n = \frac{x}{n} = \frac{-GH}{1 + GH} = S - 1 \quad (2.6b)$$

$$T = \frac{x}{d} = \frac{G}{1 + GH} = GS \quad (2.6c)$$

In [47] the following argumentation is proposed to define the loop shaping requirements for active damping control. To prevent the amplification of measurement noise n , the transfer function T_n should be as small as possible. At the target mode, $|T| \ll |G|$ is required, while $|T| \approx |G|$ should be maintained at all other frequencies to prevent influencing other dynamics of the system. This results in the desired sensitivity function S having the shape of a notch, as visualized in Figure 2.8a. At resonance $|S| \ll 1$, since the sensitivity acts as the vibration reduction ratio, and at all other frequencies $|S| \approx 1$.



(a) Desired dynamics of Sensitivity S and open-loop GH (b) Desired damped response of the closed-loop dynamics T

Figure 2.8: Illustration of the concept of loop-shaping in frequency domain [47]

The loop shaping can be summarized in the following two requirements relating to the gain and the phase of the open-loop [47]:

1. **Gain requirement:** As the sensitivity function S should have the shape of a notch, the ideal loop shape of the open-loop gain GH is triangular, illustrated in Figure 2.8a.
2. **Phase requirement:** The open-loop gain GH results in two crossover frequencies, ω_{c1} and ω_{c2} in Figure 2.8a. To achieve the desired closed-loop response, as presented in Figure 2.8b, the sensitivity at these crossover frequencies should be $|S| \leq 1$. Moreover, to prevent the occurrence of peak splitting, sufficient phase margin at both crossovers is required, which means the open-loop phase should satisfy

$$\phi(\omega_{c_i}) = \angle G(\omega_{c_i})H(\omega_{c_i}) \geq -120^\circ \quad (2.7)$$

In the following section different existing active vibration control techniques will be presented and evaluated based on the described loop-shaping requirements.

2.4.2. Active Damping Control Algorithms

While extensive research has focused on using fixed-structure controllers to damp primary resonant modes, their application to higher-order non-collocated modes has received limited attention. This section reviews fixed-structure controllers based on the collocated dynamics of second-order systems as discussed in the existing literature.

Lead Control

Lead compensators have a general transfer function of the form [24]:

$$H(s) = g \frac{Ts + 1}{\alpha Ts + 1} \quad (\alpha < 1) \quad (2.8)$$

This compensator introduces a phase lead between its pole and zero and thus active damping for every mode within this band, see Figure 2.9. Given that collocated systems have a phase that is always contained between 0° and -180° , results in the desired phase of 90° when it lies in this band for damping of the mode. From the frequency response of this compensator, it is evident that it does not have high-frequency roll-off. According to [24] the maximum achievable modal damping is given by

$$\zeta_{max} \simeq \frac{z_i - \omega_i}{2\omega_i} \quad (\omega_i > z_i/3) \quad (2.9)$$

Where ω_i and z_i represent the open-loop pole and zero respectively. The maximum achievable damping thus depends on the separation between this pole and zero.

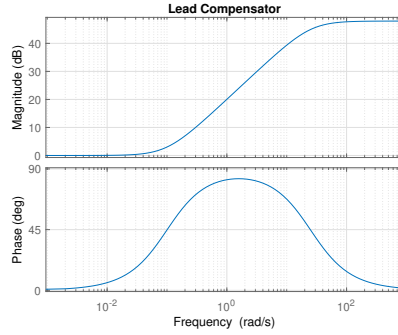


Figure 2.9: Bode frequency response Lead Compensator (Equation (2.8))

Direct Velocity Feedback (DVF)

Direct Velocity Feedback (DVF) for active vibration control was first introduced by Balas [48]. The measured velocity signal is directly fed back into the control loop in negative sense. The only control element is a static gain g multiplied with the velocity signal, as presented in Figure 2.10. For a collocated system, where the phase is contained within 0° and -180° , DVF implements pure viscous damping with a phase margin of 90° [49]. Figure 2.11 presents the implementation of DVF on a single degree-of-freedom plant. Direct Velocity Feedback can guarantee unconditional closed-loop stability for; [86, 87]

$$g > 0 \quad (2.10)$$

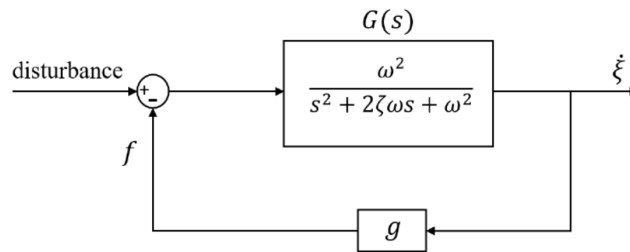


Figure 2.10: Direct Velocity Feedback control scheme [78]

According to [24] the maximum achievable modal damping depends on the spacing between the open-loop pole ω_i and nearby zero z_i , which can be mathematically described as

$$\zeta_{max} \simeq \frac{\omega_i - z_i}{2z_i} \quad (z_i > \omega_i/3) \quad (2.11)$$

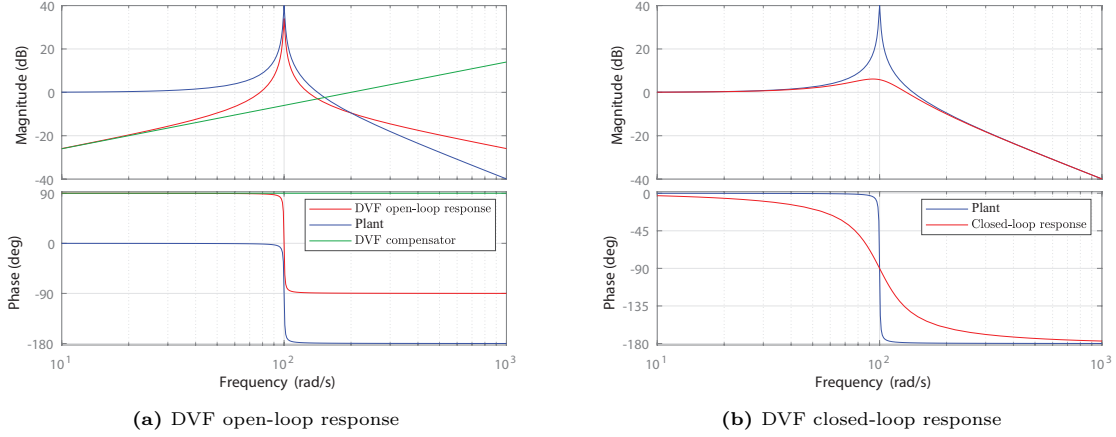


Figure 2.11: Active vibration control using Direct Velocity Feedback

One of the most fundamental drawbacks of DVF, with the control being a static gain, is the absence of both low- and high-frequency roll-off [88]. Although DVF does not prevent spillover, this does not cause closed-loop instability [89]. Moreover, note that DVF can satisfy both requirements presented in Section 2.4.1. However, the finite bandwidth of actuators can cause instability of modes outside of this bandwidth [52]. With the controller input signal being velocity and the often-used strain sensors that measure displacement, it calls for the need for a differentiator between the sensor and the controller. Including a differentiator in the control loop is not preferable as it increases signal noise. Another concern of DVF is the high-control effort at all frequencies, which can lead to actuator saturation and reduced efficiency [89]. This high gain of the controller at high frequencies may also lead to the amplification of noise and introduce the risk of system destabilization, particularly in the presence of time delays and parasitic dynamics [47].

Integral Force Feedback (IFF)

Integral Force Feedback (IFF) utilizes a force sensor and a displacement actuator, where an integral controller is used to directly augment the damping of the target mode [50]. In the specific case of an actuator/sensor pair made of a displacement actuator and force sensor, zero-pole interlacing occurs, rather than the previously discussed pole-zero interlacing for collocated systems. The closed-loop system is unconditionally stable, for all values of integrator gain g [24]. The maximum achievable modal damping with IFF is [24]

$$\zeta_{max} \simeq \frac{\omega_i - z_i}{2z_i} \quad (z_i \geq \omega_i/3) \quad (2.12)$$

The major advantages of IFF are the simplicity, guaranteed stability and robustness to variation of resonance frequency. However, the performance of IFF is depending on the system's stiffness relative to the actuator stiffness, which means some systems exhibit insufficient damping with the use of IFF. Moreover, the control gain of the integrator decreases at higher frequencies, which makes it less effective for high-frequency modes. In [90] a feed-through term, like in Integral Resonance Control, is added, which allows for an arbitrary damping ratio to be achieved for a mechanical system. From an analytical perspective, this optimal IFF is identical to IRC, but IRC provides greater opportunities for enhancement [91].

Integral Resonance Control (IRC)

It is common to truncate the model of the system to include only the modes that are to be controlled. However, this truncation can introduce significant errors, as the in-bandwidth zeros are dependent on the out-of-bandwidth poles [49]. It is therefore that Integral Resonance Control (IRC) includes a constant feedthrough term D , see Equation (2.13), of which has been shown that it is sufficient to model the effect of high-frequency modes on low-frequency zeros [92].

$$G = \sum_{i=1}^N \frac{k_i}{s^2 + 2\zeta_i \omega_i s + \omega_i^2} + D \quad (2.13)$$

By choosing D sufficiently large and negative, a pair of zeros below the frequency of the first resonant mode is added [93], changing the pole-zero interlacing property to zero-pole interlacing. A typical pole-zero plot of the collocated transfer function before and after addition of the feed-through term D is shown in Figure 2.12. Note that the pole locations are not affected by adding the feed-through term.

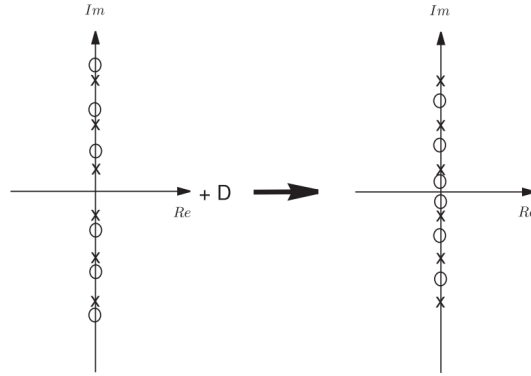


Figure 2.12: Effect of feed-through term on poles and zeros of the collocated transfer function [49]

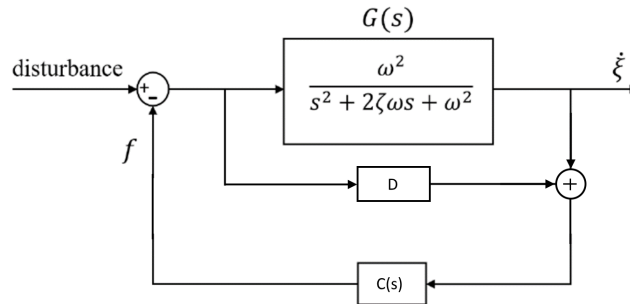


Figure 2.13: Closed loop control scheme of Integral Resonance Control

The zero-pole interlacing property keeps the open-loop phase between 0° and -180° . Using a negative integral controller in negative feedback ensures a phase margin of 90° and infinite gain margin, as the controller adds a constant 90° phase lead. As the controller gain increases, the poles initially move away from the imaginary axis, increasing damping, until they approach the zeros [49]. While direct integral control is well-researched [24], it can cause high sensitivity at low frequencies, leading to actuator saturation. To address this, lossy integrators and band-pass filters have been introduced [49], though they slightly reduce the phase margin. Integral control (IRC) has been successfully applied in nanopositioning and flexible beams with collocated properties [93–95], but its high control effort at low frequencies remains a drawback. Additionally, arbitrary feedthrough term assignment limits closed-loop pole placement [91], and the method does not address non-minimum phase behaviour in non-collocated systems.

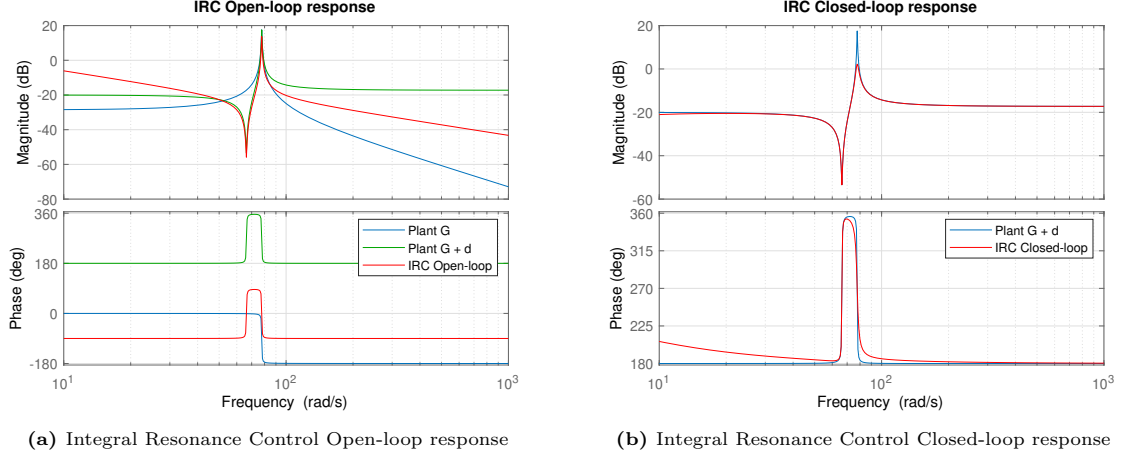


Figure 2.14: Active Damping Control with Integral Resonance Control

Negative Position Feedback (NPF)

Negative Position Feedback (NPF) involves the feedback of a measured position signal through a second-order high-pass filter, which can be written as

$$C(s) = \frac{gs^2}{s^2 + 2\zeta_f\omega_f s + \omega_f^2} \quad (2.14)$$

In the literature, Negative Position Feedback (NPF) is often referred to as Resonant Control (RC). However, to avoid confusion with other resonance control techniques, this report specifically refers to it as NPF.

The closed-loop control scheme of an NPF controller is shown in Figure 2.15. The s^2 term differentiates the position signal to provide acceleration feedback, with the high-pass filter cutoff frequency (ω_f) tuned to match the resonant mode. By shifting the system's poles deeper into the left half-plane, NPF adds active damping [87]. It ensures stability for $g > 0$ [51], even in the presence of out-of-bandwidth modes [49].

As shown in Figure 2.16a, NPF adds 90° of phase at resonance, resulting in the desired -90° for damping in the closed-loop response. The gain g and damping ratio ζ_f can be adjusted to control peak attenuation, though improper tuning can cause peak splitting [47].

NPF is the electrical equivalent of a mechanical dynamic vibration absorber, such as a tuned mass damper or skyhook damper [73]. Using multiple electrical dynamic absorbers (EDAs) tuned to different modes, multiple vibrations in a flexible structure can be efficiently suppressed [56].

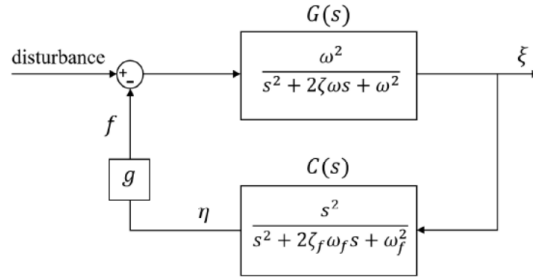


Figure 2.15: Negative Position Feedback scheme [78]

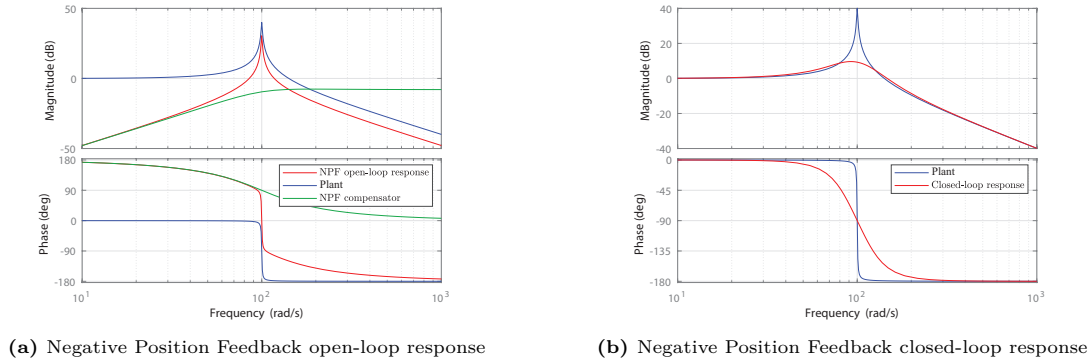


Figure 2.16: Active damping control with Negative Position Feedback

The use of a high-pass filter as compensator introduces spillover to higher order modes, as it lacks high-frequency roll-off [88]. Because of this high-frequency spillover, lower frequency modes must be tuned prior to higher frequency modes when using multiple compensators in parallel [96]. In practice, the use of NPF is not appealing since actuators and sensors typically exhibit high-frequency dynamics which are not neglected due to the characteristics of the high-pass filter and can consequently destabilize the system.

Negative Derivative Feedback (NDF)

Negative Derivative Feedback (NDF), proposed in [97], consists of a second-order band-pass filter, with negative velocity feedback, and has the following transfer function

$$C(s) = \frac{g\omega_c s}{s^2 + 2\zeta_c\omega_c s + \omega_c^2} \quad (2.15)$$

The cut-off frequency of the compensator (ω_c) is tuned to the resonance frequency of the target mode. The other control parameters, ζ_c and g , can be tuned to achieve the desired damping. The NDF-controller is closed-loop stable for feedback gain $g > 0$. Figure 2.17 presents the implementation of an NDF controller to dampen a primary resonant mode. This control algorithm was developed to overcome the high-frequency spillover and low-frequency amplification problems of other resonant controllers, like NPF and PPF. As a result, the open-loop response can satisfy both the gain- and phase requirement stated in Section 2.4.1. Because of the band-pass compensator, better performance and robustness are achieved compared to other resonant control techniques. However, for this control architecture, a displacement signal has to be differentiated to a velocity signal, which in view of noise amplification is not favorable.

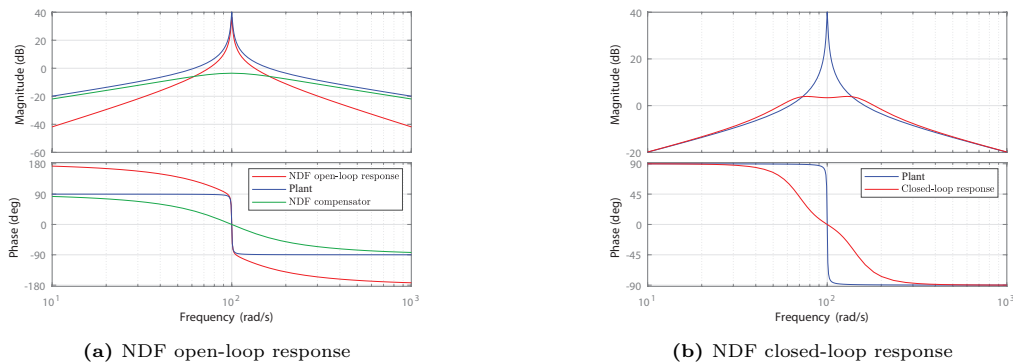


Figure 2.17: Active vibration control with Negative Derivative Feedback

Positive Position Feedback (PPF)

Positive Position Feedback (PPF) was first introduced by Goh and Caughey [52], originally developed to overcome the shortcomings of Direct Velocity Feedback, and was implemented first in 1987 by Fanson [98]. Ever since it has been one of the most utilized control methods in active damping control of collocated systems. PPF uses a measured displacement signal that is positively fed back through a second-order low-pass compensator. The cut-off frequency of this low-pass filter is tuned to match the resonance frequency of the structure, to provide active damping of this mode. Figure 2.18 presents a PPF control scheme. Following the Routh-Hurwitz stability criterion PPF is closed-loop stable for feedback gain g is [98];

$$0 < g < 1 \quad (2.16)$$

When the feedback gain exceeds 1, a pole moves into the right half plane causing instability. Since the instability occurs for large gains which are not used in practice, the PPF can be regarded as unconditionally stable [24]. Figure 2.19 shows the implementation of PPF as presented in the control scheme in Figure 2.18.

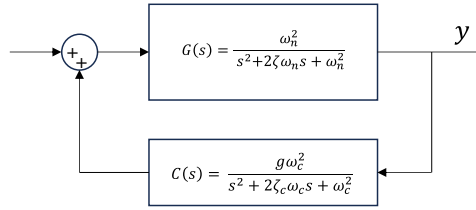


Figure 2.18: Positive Position Feedback control scheme

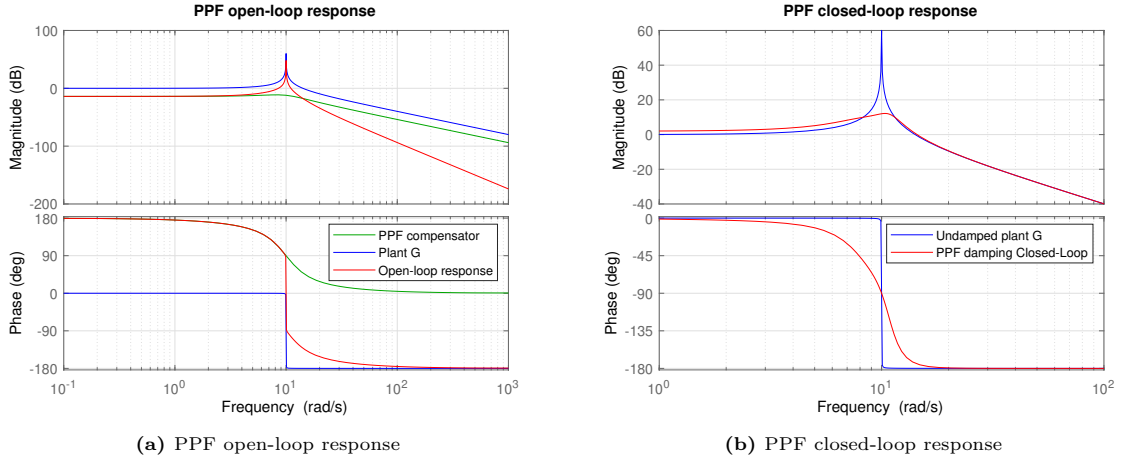


Figure 2.19: Active Vibration Control with Positive Position Feedback

The PPF compensator has two tunable parameters, the gain g and damping ratio ζ_c , both significantly affect the stability and performance of the control system. The resulting effective damping at the resonance (ζ_e), depends on the damping of the structure (ζ) and both control parameters (g, ζ_c), and can be described by; [99]

$$\zeta_e = \zeta + \frac{g}{4\zeta_c} \quad (2.17)$$

Figure 2.20 shows the influence of feedback gain g on both the open-loop and closed-loop response. The magnitude of the open-loop is increased at all frequencies as the gain is increased, the phase does not change [100], which can also be seen in Figure 2.20a. From the closed-loop response, in Figure 2.20b, it becomes evident that increasing the gain results in more vibration attenuation. For large feedback gains, the rise of new resonance peaks is observed in the closed-loop response, which is also described in [100]. The difference between the frequencies of the new peaks increases as the gain is increased.

The closed-loop response in Figure 2.20b also shows the unstable response for a gain g larger than 1. The low-pass characteristics of the PPF controller play a role of stiffness at frequencies lower than the resonance. For an increasing gain, this stiffness reduces [100], which can be observed in the open-loop response in Figure 2.20a. A larger gain thus results in better peak attenuation but at the cost of an increase of active flexibility, i.e. spillover.

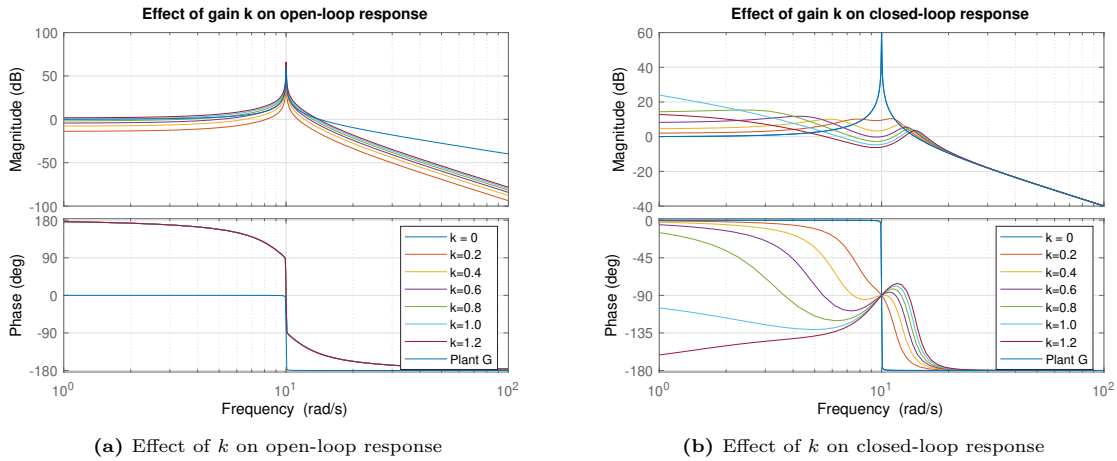


Figure 2.20: Varying feedback gain k , whilst damping ratio is kept constant ($\zeta_c = 0.3$)

Figure 2.21 shows the influence of damping ratio ζ_c on both the open- and closed-loop response, whilst the feedback gain is kept constant at an arbitrary stable value ($g = 0.2$). In Figure 2.21a it can be observed that the magnitude of the open-loop around the resonance decreases as the damping ratio is increased, as also described in [100]. In the closed-loop, Figure 2.21b, the rise of two new resonance peaks can be observed for small damping ratios. This phenomenon was also observed in the control of a sandwich plate with PPF in [66]. The rise of these two resonances can be explained by a violation of the loop shaping phase requirement in Section 2.4.1. At both crossover frequencies in the open-loop transfer function, sufficient phase margin is required to prevent the appearance of two new resonance peaks [47]. An increase of damping ratio results in sufficient open-loop phase margin and therefore makes the controller more robust with respect to uncertain modal frequencies [101], but at the cost of a decrease in peak attenuation and increased flexibility at lower modes [56].

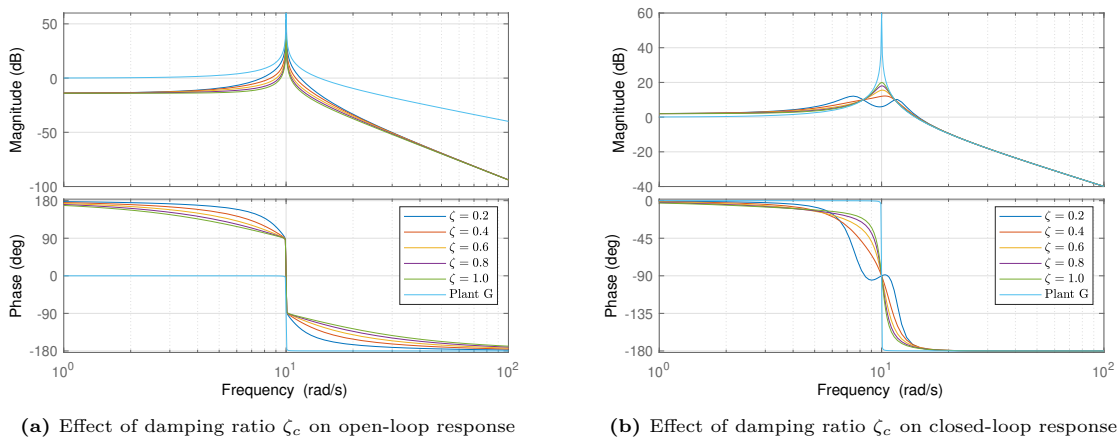


Figure 2.21: Varying damping ratio ζ_c , whilst feedback gain is kept constant ($g = 0.2$)

One PPF filter may control more than one mode if the modes are closely spaced [55]. To control the resonances of multiple modes, multiple PPF controllers can be used in a parallel setup as illustrated in

Figure 2.22. Close spacing between the poles and zeros reduces the achievable damping, enhances the coupling between them and can thus result instability through spillover [102].

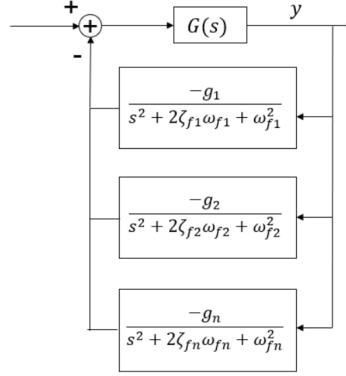


Figure 2.22: Parallel setup of multiple PPF compensators [45]

The PPF-controlled system is robustly stable, even in the presence of time delays [56] and parasitic dynamics of higher order modes [96, 103]. However, note that PPF does not provide roll-off at lower frequencies and therefore does not satisfy the gain requirement presented in Section 2.4.1. In fact, PPF increases the active flexibility at frequencies below the tuned mode. When multiple modes are to be controlled it is because of this spillover that PPF must be tuned from higher to lower order modes [96, 100].

Various modifications to conventional positive position feedback (PPF) have been proposed. In [104], an adaptive PPF controller effectively suppresses vibrations in a flexible manipulator with unknown natural frequencies. Modal Positive Position Feedback, using a "time-sharing" strategy to allocate limited actuators across multiple modes, is applied to complex structures [105–107]. Hybrid Positive Feedback (HPF) combines second- and first-order compensators for displacement and velocity feedback, showing superior performance in controlling cantilever beam vibrations [108]. A modified PPF version using first- and second-order compensators for damping and vibration suppression is presented in [109]. Gain optimization techniques such as LQR and M-norm improve Multimode Modified PPF (MMPPF) controllers [110]. The H_∞ modified PPF strategy offers enhanced vibration reduction for flexible collocated structures [111], while [112] optimizes PPF parameters for damping based on H_2 -norm. Experimental applications of PPF in sandwich plates are validated in [66, 113]. A compensated PPF method with negative feedback improves performance by introducing roll-off at low frequencies [114].

Positive (Acceleration) Velocity Position Feedback (PVPF)

The Positive Velocity and Position Feedback (PVPF) control scheme, introduced in [53] as an extension of the PPF controller, is extensively applied in lightly damped resonant systems featuring collocated sensor-actuator pairs. The PVPF controller has transfer function

$$C_{PVPF}(s) = \frac{\Gamma_2 s + \Gamma_1}{s^2 + 2\zeta_c \omega_c s + \omega_c^2} \quad (2.18)$$

where ζ_c , ω_c , Γ_1 and Γ_2 are controller design parameters. With the Routh-Hurwitz stability criterion the following closed-loop stability conditions are determined:

$$0 < \Gamma_2 < 2\omega_n(\zeta_c + \zeta) \quad \text{and} \quad 0 < \Gamma_1 < \omega_n^2 \quad (2.19)$$

The addition of a velocity term allows for arbitrary pole placement and thus achieves a chosen damping ratio [91]. In the comparison conducted in [67] evaluating NPF, PPF, and PVPF for their application in nanopositioning stages in relation to noise rejection performance, PVPF was identified as the preferred choice.

In the context of piezo-actuated nanopositioner applications, when examining the dynamics of the voltage amplifier and the capacitive displacement sensor within the closed-loop, the precise dynamics representation is achieved through third-order transfer functions rather than second-order transfer functions [70]. These third-order models prove unsuitable for PPF and PVPF control designs, consequently, Positive Acceleration Velocity and Position Feedback (PAVPF) was introduced and validated in [54]. The PAVPF has transfer function

$$C_{PAVPF}(s) = \frac{\Gamma_3 s^2 + \Gamma_2 s + \Gamma_1}{s^2 + 2\zeta_c \omega_c s + \omega_c^2} \quad (2.20)$$

where ζ_c , ω_c , Γ_1 , Γ_2 and Γ_3 are design parameters. The addition of the acceleration term enables unrestricted pole placement in the case of third-order system dynamics.

Fractional Order Controllers

The use of fractional-order (FO) calculus is commonly used in several engineering applications, such as improving the performance of controllers. Although most literature on FO control focuses on high-authority control, there are several examples where fractional-order calculus has been applied to low-authority controllers for active vibration control [47]. In [115], an FO Integral Resonant Controller (IRC) has been developed to increase the achievable bandwidth compared to integer-order IRC implementations. A fractional-order PPF controller is proposed in [96] to increase the roll-off at high-frequencies, with the goal of reducing the spillover of the filter. In [47] a FO negative position feedback (NPF) controller for active damping is proposed to satisfy both gain and phase loop-shaping requirements from Section 2.4.1, which showed to provide greater attenuation of a resonance mode than the integer order equivalent. Several more implementations of FO calculus for active damping exist [116, 117], which are mostly FO generalisations of second-order filters [118].

Higher-order controllers

The above-mentioned fixed-structure controllers are appealing because of their low computation consumption and easy implementation. To further improve phase and gain margin, many more complex higher-order active damping methods have been proposed. In [119] a robust H_∞ -based controller is synthesized and implemented for resonance damping. Inserting a time-delayed term into a feedback control is proven to improve damping of the system [120]. Based on this, position-delayed feedback (PDF) is proposed in [121], recursive PDF in [122], and recursive acceleration-delayed feedback (ADF) in [123], to dampen resonance modes.

2.4.3. Active Damping Control Table Overview

An overview of active damping control methods found in the existing literature, is provided in Table 2.1, where the benefits and drawbacks are summarized.

Table 2.1: Active Damping Controllers in state of the art

Methods	Controller	Stability	Modal Damping	Properties
Lead Control [24]	$g \frac{T_s+1}{\alpha T_s+1}$	Unconditionally stable	$\zeta_{max} \simeq \frac{z_i - \omega_i}{2\omega_i}$	<ul style="list-style-type: none"> • Dampens all modes within band • No high-frequency roll-off
DVF [48]	gs	$g > 0$	$\zeta_{max} \simeq \frac{\omega_i - z_i}{2z_i}$	<ul style="list-style-type: none"> • 90° phase margin • Dampens all modes • Differentiator required • High control effort at all frequencies
IFF [50]	$\frac{g}{K_a s}$	Unconditionally stable	$\zeta_{max} \simeq \frac{\omega_i - z_i}{2z_i}$	<ul style="list-style-type: none"> • Robust to variation of resonance • Dampens all modes • Depending on stiffness of structure • Less effective for high-frequency modes
IRC [49]	$\frac{-g}{s-gD}$	$g > 0$	Depends on g and D	<ul style="list-style-type: none"> • 90° phase margin • Dampens all modes • High control-effort at low frequencies
NPF [51]	$\frac{gs^2}{s^2+2\zeta_c\omega_c s+\omega_c^2}$	$g > 0$	Depends on g and ζ_c	<ul style="list-style-type: none"> • Closed-loop stable in presence of out-of-bandwidth modes • Dampens designated mode • No high-frequency roll-off
NDF [97]	$\frac{g\omega_c s}{s^2+2\zeta_c\omega_c s+\omega_c^2}$	$g > 0$	Depends on g and ζ_c	<ul style="list-style-type: none"> • Reduced low- and high-frequency spillover • Dampens designated mode • Noise amplification because of differentiator
PPF [52]	$\frac{-g\omega_c^2}{s^2+2\zeta_c\omega_c s+\omega_c^2}$	$0 < g < 1$	Depends on g and ζ_c	<ul style="list-style-type: none"> • High-frequency roll-off • Robustly stable in presence of time delays and higher-order dynamics • Dampens designated mode • Low-frequency spillover
PVPPF [53]	$\frac{\Gamma_2 s + \Gamma_1}{s^2+2\zeta_c\omega_c s+\omega_c^2}$	$0 < \Gamma_2 < 2\omega_n(\zeta_c + \zeta)$, $0 < \Gamma_1 < \omega_n^2$	Depends on Γ_1 , Γ_2 and ζ_c	<ul style="list-style-type: none"> • Arbitrary pole placement • Dampens designated mode • Low-frequency spillover

2.5. Motion Control

Based on the loop-shaping requirements outlined in [16, 33], three elements are necessary to build a linear motion controller. Firstly, a lag element to provide high gain at low frequency. Secondly, a lead element to provide phase margin at the crossover region. To prevent amplification of high-frequency, this lead element is tamed at the end of the crossover region. Finally, a low-pass filter (LPF) can be added depending on the system requirements and noise levels. Combining these elements yields a so-called PID controller, where PID stands for a proportional-integral-differential filter. Although many developed motion control algorithms outperform PID controllers, they remain the dominant approach for designing motion controllers due to their straightforward mode of operation and simple implementation. In [33] a rule-of-thumb method is presented for designing the PID control parameters, based on the desired suitable control bandwidth (ω_c). The PID controller is given by

$$C_{PID} = k_p \left(1 + \frac{\omega_i}{s} \right) \left(\frac{s/\omega_d + 1}{s/\omega_t + 1} \right) \quad (2.21)$$

where k_p represents the proportional gain, and the various frequency bands are computed as follows:

$$\omega_d = \frac{\omega_c}{3} \quad , \quad \omega_t = 3\omega_c \quad , \quad \omega_i = \frac{\omega_c}{10} \quad (2.22)$$

$$k_p = 0.33 \left| \frac{1}{G(\omega_c)} \right| \quad (2.23)$$

In the case of adding an LPF to the PID controller, it is typically set to a frequency 10 times higher than the bandwidth. The bode plot of an arbitrary PID controller, designed with Equation (2.21), is depicted in Figure 2.23. Following the application of the rule-of-thumb, the next stage involves fine-tuning the parameters to ensure robustness and stability, outlined in [16].

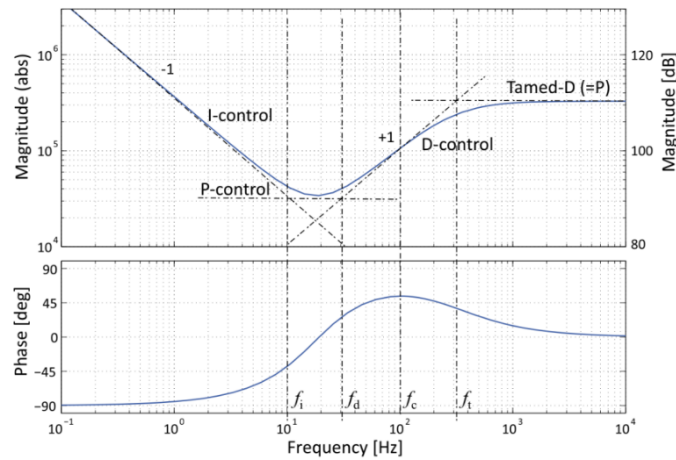


Figure 2.23: Bode plot of rule-of-thumb PID-controller [33]

2.5.1. Closed-loop performance measures

In the evaluation of motion control feedback systems, it is important to not only evaluate its performance in being able to track a given reference position but also consider disturbance rejection and noise sensitivity. Several standard sensitivity functions have been defined to quantify the performance of feedback-controlled systems. They are derived from a simplified version of the generic motion control feedback loop as shown in Figure 2.24.

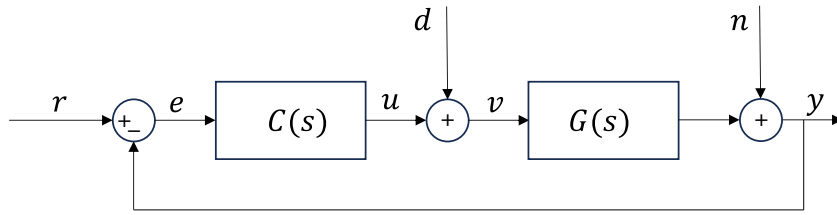


Figure 2.24: Generic motion control feedback loop

Sensitivity Function

The sensitivity function represents the sensitivity of the output (y) to a disturbance (n) on the output (y). In motion systems it is generally a displacement, for example caused by external vibrations [33].

$$S(s) = \frac{y}{n} = \frac{1}{1 + G(s)C(s)} \quad (2.24)$$

Process Sensitivity Function

The process sensitivity function describes the sensitivity of the output (y) to disturbances inside and before the system (d).

$$GS(s) = \frac{y}{d} = \frac{G(s)}{1 + G(s)C(s)} \quad (2.25)$$

Complementary Sensitivity Function

The complementary sensitivity function, also more commonly referred to as *closed-loop response*, represents the ability of the system to follow a given reference signal (r). The name complementary is based on the fact that $T(s)$ and $S(s)$ add to unity, $T(s) + S(s) = 1$.

$$T(s) = \frac{y}{r} = \frac{G(s)C(s)}{1 + G(s)C(s)} \quad (2.26)$$

2.5.2. Resonance Limiting Control Bandwidth

Resonance is one of the main performance-limiting factors in industrial motion systems. For high-performance motion systems, typically a PID-type controller is present in the motion control loop [71]. When the gain of the PID controller is increased, these resonances will cause vibrations or even instability. The resonance mode often restricts the bandwidth of the motion system to between 1% and 10% of the resonance frequency [50], and thus its performance. When higher-order modes are sufficiently distant and the dynamics of the first resonance mode can be represented by a unity-gain second-order low-pass system, the maximum bandwidth is described by [50];

$$\omega_{c_{max}} < 2\omega_n\zeta, \quad (2.27)$$

where ω_n is the natural frequency of the system, and ζ the damping ratio of the structure. In higher-order systems the control bandwidth is limited by the higher-order non-collocated mode [24].

By introducing damping to the resonance of the system, the maximum achievable bandwidth can be increased [80, 124]. This improvement is primarily attributed to the reduction of the dominant resonant peak, leading to an increased gain margin, enabling much higher gain to be used for reference tracking [50, 79]. Furthermore, by adding damping to the resonance mode of the system, oscillations can be damped faster, resulting in a shorter settling time [71].

2.5.3. Notch Filters

Inversion techniques, such as notches, are popular as they are simple to implement and can provide an excellent closed-loop bandwidth, up to or greater than the resonance frequency [41]. Many applications of notch filters for vibration attenuation are present in literature [37, 41, 125–127]. Effectively attenuating the peak response can be achieved by strategically placing a notch, as depicted in Equation (2.28), at the resonance frequency of the system.

$$N = \frac{\left(\frac{s}{\omega_n}\right)^2 + \frac{s}{Q_1\omega_n} + 1}{\left(\frac{s}{\omega_n}\right)^2 + \frac{s}{Q_2\omega_n} + 1} \quad (2.28)$$

The notch filter requires precise tuning to align with the resonance intended for attenuation, leading to a lack of robustness. The fraction $\frac{Q_1}{Q_2}$ determines the 'depthness' of the notch, whereas the individual values of Q_1 and Q_2 influence the 'widthness' of the notch. Figure 2.25 shows several notch filters where the Q factor is kept constant, but the wideness of the notch is varied. To attenuate a rather uncertain resonance, i.e. increase robustness, a wide notch filter is required. As is evident from the frequency response, a broader notch comes at the expense of a notable rise in phase lag, which can result in closed-loop instability. Moreover, when multiple modes are to be controlled, the use of multiple notches rapidly increases the computational complexity [128].

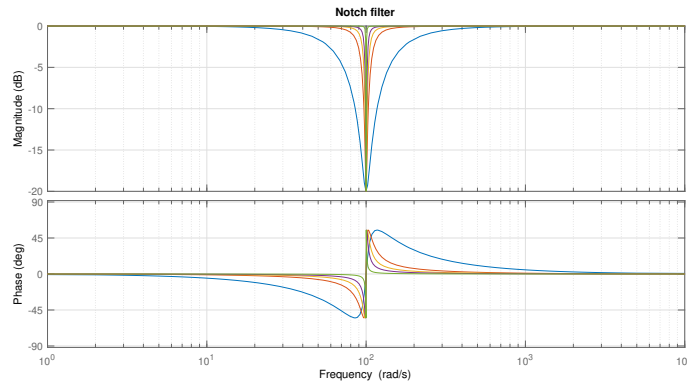


Figure 2.25: Notch filters

The major disadvantage of using notch filters is the requirement for an accurate system model, i.e. the lack of robustness. If the system resonance frequency significantly changes, a high gain inversion-based feedback controller can become unstable [50]. Due to this sensitivity, inversion methods are limited to niche applications where the resonance frequency remains stable or the feedback controller can be continuously recalibrated [41]. Consequently, inversion methods are frequently deemed impractical.

2.6. Motion Control and Active Damping Control

As an alternative to using notch filters or inversion techniques, fixed-structure active damping controllers, discussed in Section 2.4.2, are employed to increase bandwidth in numerous applications. The incorporation of an active damping controller (C_d) into the motion control loop offers various implementation possibilities, depending on the mode to be damped and the sensor/actuator configuration.

Currently, most of the research on active damping to enhance motion control bandwidth is centred around applications where the first resonant mode is dominant and higher-order modes are sufficiently distant from the first mode. The primary mode can be described by a single mass-spring-damper (1DOF) system, which is inherently collocated and allows for the application of existing active vibration control techniques to enhance damping characteristics of the undesired mode.

In [64] a PPF damping control and proportional-integral (PI) tracking control is presented for a piezoelectric tube scanning AFM. Experimental results showed significant scanning-image quality improvement with the addition of PPF damping control. An IRC damping controller with integral tracking control is applied to a scanning probe microscope in [59]. Greater than ten times improvement in tracking bandwidth is demonstrated with experimental results. The IRC method is also applied on a nanopositioning stage in [60] in combination with feedforward inversion control. In [61, 62] IFF is applied to enhance control bandwidth and is experimentally validated for its application in a nanopositioner model in [50]. Optimal IFF with a feedthrough term is applied in [63] to improve tracking control for the application in objective lens positioners. In [67] a PVPF damping controller is used to increase motion control bandwidth, which resulted in better tracking performance for a nanopositioning stage. In

[68] a PAVPF damping controller with PI tracking controller for broadband control of a piezo-actuated nanopositioning stage is used to improve control bandwidth. In [40] a state-feedback-based-dual-loop controller (SFDLC) is proposed for realizing high-bandwidth and high-accuracy control of a nanopositioning stage. An optimization method is employed to simultaneously design the inner and outer loop controllers, for increasing the damping ratio and suppressing tracking error respectively.

In Figure 2.26, a schematic illustration of a combined loop encompassing both active damping and motion control is presented. Here, C_d denotes the damping controller, and its signal can be fed back either positively or negatively, depending on the used controller. Additionally, a tracking controller C_t is employed for reference tracking, typically adopting a simple proportional-integral controller for 1DOF systems.

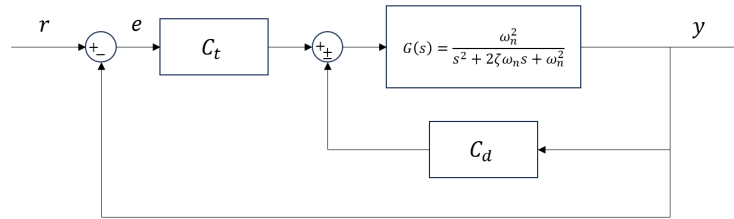


Figure 2.26: Active damping and tracking control scheme

When introducing PPF (Section 2.4.2.7) as a damping controller on the single-degree-of-freedom system presented in, employing a proportional-integral controller for reference tracking results in a significantly larger bandwidth compared to leaving the resonance undamped. In the context of the undamped system, the upper limit for the achievable bandwidth is constrained by Equation (2.27). A comparison between an undamped system and a PPF-damped system is depicted in Figure 2.27. It is important to note that the parameters of the PPF controller are not optimized in this implementation, serving merely as an illustrative example. The open-loop response, showcased in Figure 2.27a, underscores the substantial increase in bandwidth achieved with the actively damped system (ω_{c2}) in contrast to the undamped systems's bandwidth (ω_{c1}). In this instance, the bandwidth can be increased by a factor larger than 10. The effect of this increased bandwidth can be observed in the decreased rise- and settle time in Figure 2.27b.

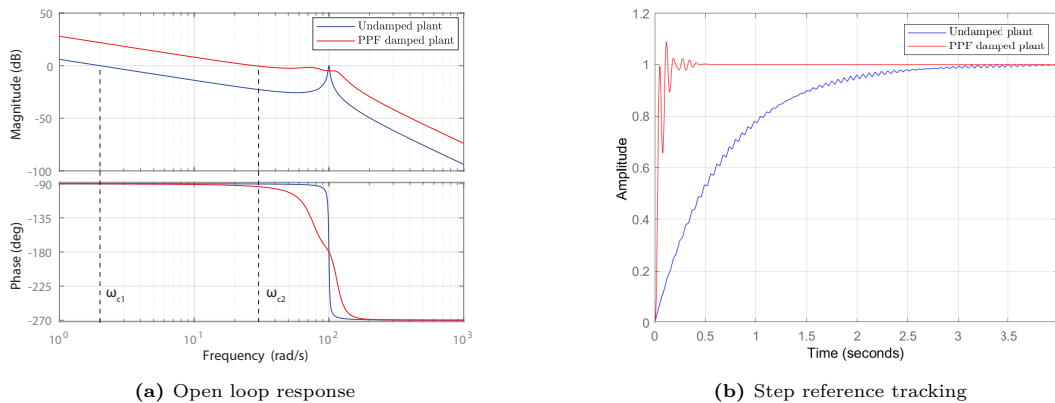


Figure 2.27: Integral reference tracking of single-degree-of-freedom system, with and without PPF damping

Although damping controllers alone cannot increase the closed-loop bandwidth beyond the resonance frequency, they have the advantage of being insensitive to variations in resonance frequency [50]. In addition, as damping controllers suppress, rather than invert, the mechanical resonance, they provide better rejection of external disturbances than inversion-based systems [17].

3

Active Damping Control of Higher-Order Resonance Mode in Positioning Systems

This chapter presents the main scientific contributions of this research, presented in a scientific paper format. The paper introduces a novel active damping control strategy designed specifically for the active damping of higher-order, non-collocated parasitic modes in positioning systems.

Active Damping Control of Higher-Order Resonance Mode in Positioning Systems

N.J. Dee, A.M. Natu, S.H. HosseinNia

Abstract—In precision positioning systems, lightly damped higher-order resonance modes can induce undesirable vibrations that degrade system performance and accuracy. These resonances pose additional challenges in non-collocated dual-stage positioning systems, where they significantly limit control bandwidth. Although conventional notch filters are commonly used alongside tracking controllers to enhance bandwidth, they lack robustness when faced with system parameter uncertainties. Moreover, the effects of the parasitic resonance on disturbance rejection remain. Active damping control has been successfully used to mitigate issues related to the primary resonance mode, but its application to higher-order parasitic modes has not been explored. This paper introduces a novel control strategy, High-Pass Positive Position Feedback (HP-PPF), designed specifically for active damping of higher-order, non-collocated parasitic modes in positioning systems. The proposed method incorporates a second-order high-pass filter within a positive feedback loop, effectively attenuating the parasitic resonance. Integrated with a PID tracking controller in a dual-loop configuration, this method enhances disturbance rejection, noise suppression, and robustness against model uncertainties, overcoming limitations of traditional notch filter-based methods while maintaining comparable tracking performance. The proposed control architecture is validated through a proof-of-concept experimental setup that demonstrates the effectiveness of the underlying mathematical framework.

Index Terms—Active Damping Control, High-Pass Filter, Higher-Order, PPF, PID, Positioning Stage, Non-collocated, Robustness.

I. INTRODUCTION

The high-tech industry experiences an ever-increasing demand for improved performance of motion stages, particularly in terms of accuracy and speed. This demand encompasses diverse high-precision applications like scanning-probe microscopy [1], micromanipulators [2], nanomanufacturing [3] and precision optics [4]. These stages require nanometer-level positioning accuracy, high response speed, compact structures, and large travel ranges [5]. The bandwidth of the control architecture driving the motion stages directly affects its speed and accuracy, with increasing bandwidth typically leading to improved performance [6]. However, increasing bandwidth comes with trade-offs, especially in linear control systems, where the waterbed effect limits performance enhancements. In addition, higher-order vibration modes in positioning systems introduce further constraints, as they generate unwanted vibrations when excited by high-frequency reference or disturbance signals [6, 7]. In non-collocated dual-stage systems, these higher-order parasitic resonances impose additional restrictions on the control bandwidth, as the minimum-phase

behaviour of non-collocated dynamics limits achievable bandwidth to a fraction of the higher-order resonance frequency [8].

Approaches such as feedforward [9], input shaping [10], inversion [11], and the application of notch filters [12, 13] have successfully been employed in combination with conventional tracking controllers to mitigate the effects of parasitic resonances. Despite their potential effectiveness in systems with precise models and known references, these methods lack robustness against system parameter uncertainties and external disturbances [14]. Moreover, while notch filters can extend control bandwidth and enhance the rejection of low-frequency disturbances, such as floor vibrations, when used alongside tracking controllers, the effects of parasitic resonance still degrade the closed-loop disturbance rejection performance [15]. This residual effect can lead to errors, for example in cases where cross-couplings in multi-degree-of-freedom systems introduce additional disturbances around this frequency into the system.

An alternative approach involves active damping control of resonant modes through the use of feedback compensators. These fixed-structure active damping controllers are designed to be inherently robust and easy to tune, using general knowledge of the dynamics of a system [16]. Common controllers include direct velocity feedback (DVF) [17], integral resonance control (IRC) [18], integral force feedback (IFF) [19], negative position feedback (NPF) [20], positive position feedback (PPF) [21], positive velocity and position feedback (PVPF) [22], and positive acceleration, velocity and position feedback (PAVPF) [23]. Among these, PPF, PVPF, and PAVPF are widely adopted due to their ease of implementation, effective roll-off characteristics, ability to suppress multiple modes [24], and robustness against parameter variations [25]. However, PPF and PVPF require collocated actuator-sensor configurations because they are designed specifically for second-order systems [26]. Third-order models, which describe the dynamics of nanopositioning stages [27], have led to the development of the PAVPF damping controller, proven effective in enhancing bandwidth when combined with tracking control [26].

Despite these advances, current methods mainly focus on damping the primary resonance mode, typically assuming that higher-order modes are far enough away to be considered negligible and unlikely to induce vibrations and errors. However, these higher-order modes can show at relatively low frequencies in vicinity of the dominant mode, for example in systems incorporating flexure-based guiding mechanisms, where they contribute to errors when being excited. In industrial applications like dual-stage positioning systems, such as

wafer stages and reticle stages used in lithography machines [28], these higher-order modes pose an even more significant challenge. These systems, typically employing Single-Input Single-Output (SISO) configurations with a single actuator and sensor, can be simply represented by fourth-order dynamics, characterized by two dominant modes that capture the primary modal behaviour. The higher-order non-collocated parasitic mode not only introduces positioning errors but also directly limits the control bandwidth. Research has explored the concept of overactuation, which involves employing more actuators than there are rigid body modes to be controlled, to achieve active damping of higher-order modes [15]. However, this approach requires additional actuators, which might not always be feasible in practical applications and adds complexity to the system and its control architecture. At present, no generally applicable active damping control strategy specifically addresses higher-order parasitic resonance modes, which limit positioning accuracy and, in certain applications, even tracking control bandwidth.

A. Contributions

This paper proposes a novel fixed-structure controller approach for active damping of the first dominant higher-order mode in positioning systems while preserving the simplicity of a SISO configuration. The primary focus of this work is on the non-collocated higher-order parasitic mode in dual-stage positioning systems, as it imposes an additional constraint on control bandwidth. However, it is important to emphasize that the general framework of the proposed solution can be utilized to achieve active damping of any higher-order mode that introduces unwanted vibrations in positioning systems. The key contributions of this work are as follows:

- (1) This paper provides a general solution for active damping of higher-order parasitic modes, enhancing disturbance rejection and noise suppression at those frequencies.
- (2) The novel active damping control method enhances control bandwidth when combined with conventional tracking controllers in dual-stage positioning systems, achieving comparable tracking performance to a notch filter-based method.
- (3) The proposed solution demonstrates robust performance against model uncertainties, particularly concerning resonance frequency variations within a defined range, offering significant improvements in robustness compared to a notch filter-based method.

This paper is organized as follows. Section II presents an overview of the system dynamics and the experimental setup used as a proof-of-concept. Section III introduces the proposed active damping controller designed to address higher-order parasitic resonance modes. Section IV details the integration of the active damping controller into a motion control loop for application in a dual-stage positioning system. Section V presents an experimental comparison between the novel active damping control and a notch filter-based solution, focusing on process disturbance and noise rejection, robustness against model uncertainties, and reference tracking performance. Finally, conclusions are drawn in Section VI.

II. SYSTEM DESCRIPTION

A. System Modelling

The dynamics of positioning systems are typically characterized by a rigid-body mode followed by one or more higher-order resonance modes. To describe the dynamics of a general mechanical structure containing a resonance, the following transfer function is introduced:

$$\frac{x_s}{F_a} = \frac{1}{ms^2} + \frac{\alpha}{ms^2 + k}, \quad (1)$$

where α represents the high-frequency contribution of the first higher-order mode relative to that of the rigid-body motion [29]. Non-collocated dynamics are found for $\alpha = -1$; for instance, this situation arises in a two-body mass-spring-damper system where the position is measured at body 2 while actuating at body 1. This double-mass-spring-damper system, illustrated in Figure 1, effectively captures the behaviour of the first two dominant resonance modes, representing the principal dynamics of single-axis dual-stage positioning systems. In this simplified model, the position of the end-effector (m_2) is controlled by actuating the base stage (m_1), resulting in a non-collocated actuator-sensor configuration. The non-collocated system dynamics, $G(s)$, which describe the transfer function from the actuator force (F_{act}) to the displacement of the second mass (x_2) can be approximated by the following fourth-order transfer function [15]:

$$G(s) = \frac{c_2 s + k_2}{(m_2 s^2 + c_2 s + k_2)(m_1 s^2 + (c_1 + c_2)s + (k_1 + k_2)) - (c_2 s + k_2)^2} \quad (2)$$

With two pole-pairs observed at $\omega_1 \approx \pm j \sqrt{\frac{k_1}{m_1 + m_2}}$ and $\omega_2 \approx \pm j \sqrt{\frac{k_2(m_1 + m_2)}{m_1 m_2}}$.

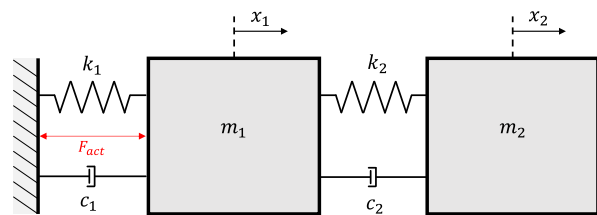


Figure 1: Analytical double-mass-spring-damper representation

The non-collocated transfer function in Equation (2) can be expressed in general form, with unity gain at 0 Hz, as

$$G(s) = \frac{\omega_1^2 \omega_2^2}{(s^2 + 2\zeta_1 \omega_1 s + \omega_1^2)(s^2 + 2\zeta_2 \omega_2 s + \omega_2^2)} \quad (3)$$

where ω_1 and ω_2 are the resonance frequencies with corresponding damping ratios ζ_1 and ζ_2 respectively. The corresponding frequency response is depicted in Figure 2, where the spacing between the modes is denoted with n , such that $\omega_2/\omega_1 = n$. This mode spacing depends on the relative modal gains of the two resonance modes, which are governed by the stiffness and mass properties of the two stages, as described in Equation (4).

$$n = \frac{\omega_2}{\omega_1} \approx \sqrt{\frac{k_2 (m_1 + m_2)^2}{k_1 m_1 m_2}} \quad (4)$$

The higher-order non-collocated mode is characterized by a -20 dB/dec slope before and -40 dB/dec slope after resonance. The minimum phase behaviour is observed as a phase shift from -180° to -360° at the resonance frequency, corresponding to the magnitude slopes. The height of the parasitic resonance peak is approximately equal to $1/(2\zeta_2)$ [15], indicating that increasing the modal damping coefficient reduces the peak height in the frequency domain. In the following sections a methodology will be proposed to improve the damping characteristics of this mode through an active damping control feedback loop, effectively reducing the peak height of the undesired resonance mode.

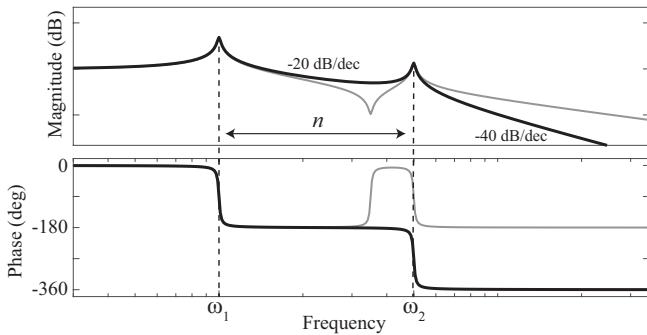


Figure 2: General non-collocated x_2/F_a (black) and collocated x_1/F_a (grey) frequency response of double-mass-spring-damper configuration, representing the dynamics of a single-axis dual-stage positioning system

B. Proof-of-Concept Experimental Setup

The experimental setup described in this paper is the single-axis dual-stage compliant micro-motion system from [15], illustrated in Figure 3. This prototype serves as a proof-of-concept for a non-collocated dual-stage positioning system, aimed at experimentally validating the contributions presented in this paper.

The system consists of a base stage and an end-effector stage connected by four parallel guiding flexures. A second set of parallel flexures links the base stage to a fixed reference ground, enabling translational movement of the stages while restricting other degrees of freedom. To minimize external disturbances, the entire setup is mounted on a vibration isolation platform. Actuation of the base stage is achieved using a race-coil Lorentz actuator, which generates a bidirectional force proportional to the input current. Input voltage signals are amplified and converted into the necessary current by a current amplifier, which maintains a constant gain factor during amplification up to a cutoff frequency of approximately 10 kHz. The position of the end-effector is measured using a laser interferometer, with a resolution of 39.5 nm, and an optical mirror, mounted on the end-effector stage to replicate the non-collocated dynamics. By accurately controlling the

input current to the Lorentz actuator, precise actuation and control of the system is achieved.

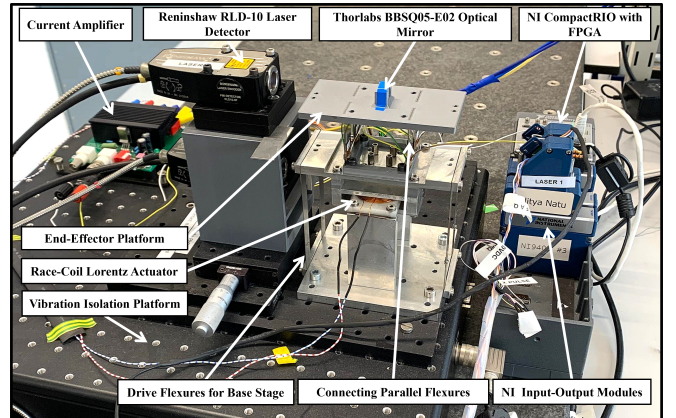


Figure 3: Experimental setup

To perform system identification of the experimental setup, a sine sweep with increasing amplitude, ranging from 1 to 1000 Hz, is applied as the input signal to the Lorentz actuator. The position of the end-effector is measured, allowing the transfer function to be estimated based on the relationship between the input and output signals. The resulting identified transfer function is shown in Figure 4, along with the analytical model from Figure 3. The first mode appears at 6 Hz and the first dominant higher-order mode at 78 Hz. The gain of the analytical model is compensated to account for the stiffness of bottom flexures connecting the base stage to the ground, as well as the dynamics of the actuator and amplifier. Additionally, the phase is compensated to account for the 180° phase offset resulting from the inversion caused by the operational amplifier used in the setup.

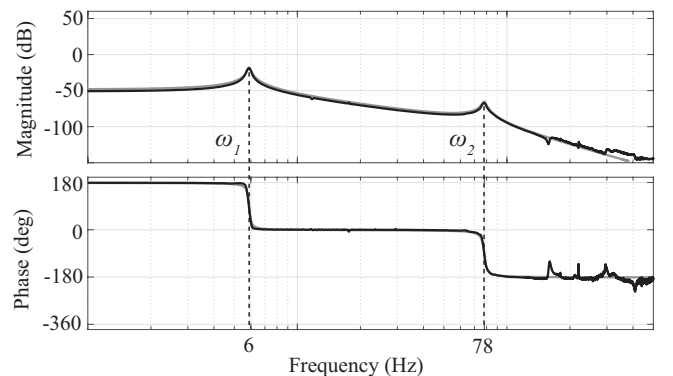


Figure 4: Identified frequency response of experimental setup (black) and compensated analytical model of system dynamics (grey)

III. ACTIVE DAMPING USING HIGH-PASS POSITIVE POSITION FEEDBACK (HP-PPF)

As previously stated, the remainder of this paper concentrates on the active damping of a higher-order non-collocated mode to fully illustrate the potential contributions, although the general framework applies to any higher-order mode. In

addition to generating unwanted vibrations, the higher-order non-collocated mode also imposes limitations on the control bandwidth. As illustrated in Figure 5, when feedback gain is added to the higher-order mode, which is typically done with tracking controllers to improve the bandwidth, the resonance peak emerges above 0 dB. This results in two additional crossover frequencies in the open-loop response, for which the phase lies below -180° , leading to system instability. Due to the minimum phase behaviour of the non-collocated mode, the phase inevitably crosses -180° at this frequency. Therefore, to ensure stability within a conventional tracking control architecture, the resonance peak must remain below 0 dB in the open-loop response. This constraint limits the amount of gain that can be applied and, consequently, the maximum achievable control bandwidth. It is therefore of significant interest to increase the damping characteristics of this higher-order mode, which can be achieved through the implementation of a novel active damping control-based solution. This enhances the damping properties and effectively reduces the peak height associated with the undesired resonance mode.

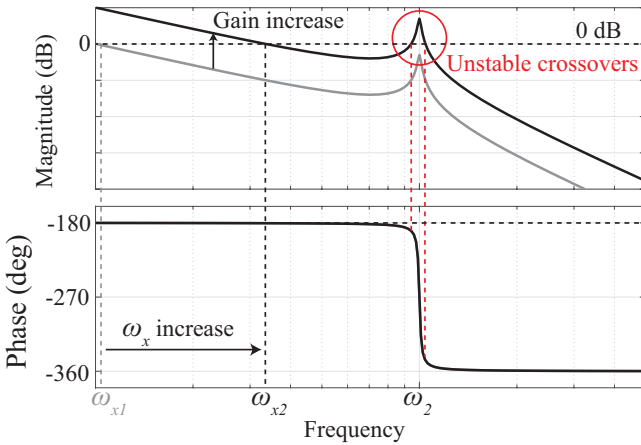


Figure 5: Higher-order non-collocated mode with increased feedback gain to increase bandwidth (ω_x), resulting in unstable crossover frequencies in open-loop response.

When the rigid-body dynamics are neglected, the higher-order parasitic mode can be simplified to the following generalized transfer function:

$$G_p(s) = \frac{\omega_2^4}{s^2 (s^2 + 2\zeta_2\omega_2 s + \omega_2^2)} \quad (5)$$

where ω_2 and ζ_2 are the resonance frequency and corresponding damping ratio respectively. This simplification describes the system dynamics in the region of interest around the higher-order parasitic resonance mode, for the frequency range ($\omega > \omega_1$, where ω_1 is the rigid-body mode frequency).

Active damping control of the primary mode is commonly achieved using various control techniques, such as employing a second-order low-pass filter within a positive feedback loop, as seen in PPF. Figure 6a illustrates a general feedback loop

employing an active damping controller (C_d) to dampen the resonance peak of the system (G).

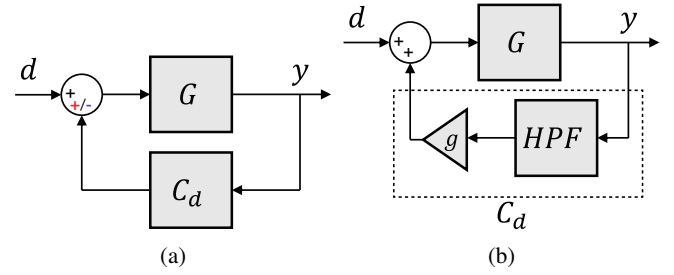


Figure 6: (a) General active damping control loop with positive feedback (red) or negative feedback (blue). (b) Active damping control loop employing second-order high-pass filter (HPF) in positive feedback (HP-PPF).

The frequency response of the higher-order non-collocated mode differs from that of the primary mode, as it exhibits a -20 dB/dec slope before resonance, as shown in Figure 2, which arises from the influence of the rigid-body mode at lower frequencies. The minimum phase behaviour of the higher-order non-collocated mode, which involves a phase shift from -180° to -360° , makes the direct implementation of active damping methods like PPF and NPF infeasible. These methods make use of second-order low-pass filters (LPF) and second-order high-pass filters (HPF), where in the case of PPF a positive feedback sign is used. By inverting the feedback sign, the open-loop response is effectively multiplied by -1 , introducing a 180° phase shift. This phase shift can be used to achieve a positive phase margin in the open-loop damping response, a key requirement for stability as outlined in [16].

Figure 7 shows the open-loop response of the active damping architecture (Figure 6a) for the higher-order non-collocated mode described in Equation (5), comparing a second-order LPF and second-order HPF used as damping controllers, with phase margins indicated. The 2nd-order LPF results in an open-loop phase between -180° and -360° (indicated in grey), resulting in two negative phase margins. Positive feedback shifts the phase by 180° , which moves the phase from 0° to -360° , meaning the second crossover (φ_{m2}) still exhibits negative phase margin, leading to an unstable closed damping loop.

Using a second-order HPF initially places the open-loop phase between 0° and -360° (shown with solid black line) with negative phase margin at the second crossover. However, applying positive feedback shifts the phase by 180° (indicated with the black dashed line), bringing the open-loop phase into the stable region between 180° and -180° , resulting in positive phase margins at both crossover frequencies, fulfilling the stability phase requirement. This open-loop phase analysis shows that only the second-order HPF within a positive feedback loop can result in a stable closed damping loop.

This analysis can be mathematically validated using the Routh-Hurwitz criterion to evaluate the stability of the closed damping loop. The characteristic equations for both the closed

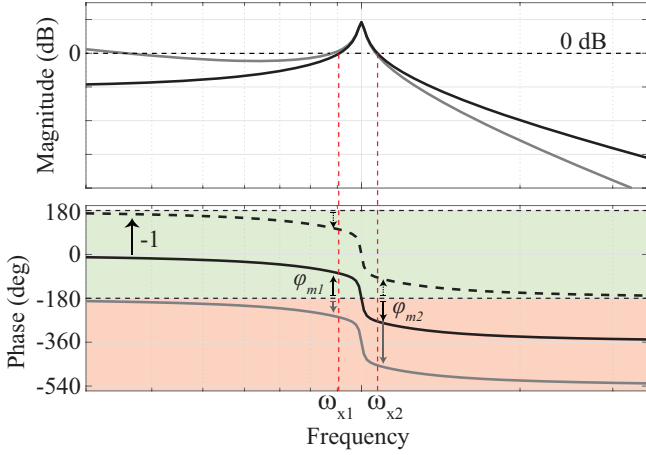


Figure 7: Active damping open-loop ($G_p(s) \cdot C_d(s)$) response; higher-order non-collocated mode with second-order LPF (grey) and second-order HPF (black) as damping controller. Positive feedback shifts phase with 180° (black dashed line) into stable region.

damping loops employing second-order LPF and HPF controllers, with positive and negative feedback signs, are derived in Appendix A. The general form of the characteristic equation can be expressed as follows:

$$a_n s^n + a_{n-1} s^{n-1} + a_{n-2} s^{n-2} + \dots + a_0 s^0 = 0 \quad (6)$$

The necessary Routh-Hurwitz criterion states that for stability all coefficients of the characteristic polynomial must be positive and greater than zero. The coefficients derived from the characteristic equations in Appendix A are summarized in Table I. Notably, when using the second-order LPF as active damping controller, the a_1 coefficient is always zero, regardless of the feedback sign, indicating the presence of an unstable pole. This instability correlates with the negative phase margin seen in Figure 7.

In contrast, the coefficients suggest that the second-order high-pass filter with both positive and negative feedback yields a stable closed-loop system under the conditions $1 - g_n > 0$ and $1 + g_n > 0$, respectively. However, this does not align with the instability seen in the open-loop phase analysis for the negative feedback case. The discrepancy arises because this necessary condition does not guarantee stability. To ensure stability, the sufficient conditions of the Routh-Hurwitz criterion must also be met.

Appendix A derives these conditions for the second-order HPF in both feedback cases using the Routh array, summarized in Table II. For the negative feedback loop with the second-order HPF, the first column of the Routh array shows two sign changes, indicating the presence of two right-half-plane poles, confirming instability. Conversely, for the positive feedback loop, all coefficients in the first column remain of the same sign when $1 - g_n > 0$, ensuring stability.

It is important to note that the negative feedback loop becomes stable when $g_n < 4\zeta_2\zeta_c$. However, given that the values of ζ_2

and ζ_c are typically small, this condition would only be met when g_n is very small. As g_n directly influences the damping performance, achieving sufficient peak attenuation generally requires g_n to be greater than $4\zeta_c\zeta_2$. Therefore, in practical terms, only the second-order high-pass filter in a positive feedback loop can achieve a stable closed damping loop.

Table I: Coefficients of the characteristic equation for active damping of the higher-order non-collocated mode using a 2nd-order LPF and 2nd-order HPF with both positive and negative feedback signs.

	2nd-order LPF (\mp Feedback)	2nd-order HPF (\mp Feedback)
a_6	1	-
a_5	$2\omega_2(\zeta_c + \zeta_2)$	-
a_4	$2\omega_2^2(1 + 2\zeta_c\zeta_2)$	1
a_3	$2\omega_2^3(\zeta_c + \zeta_2)$	$2\omega_2(\zeta_c + \zeta_2)$
a_2	ω_2^4	$2\omega_2^2(1 + 2\zeta_c\zeta_2)$
a_1	0	$2\omega_2^3(\zeta_c + \zeta_2)$
a_0	$\pm g_n \omega_2^6$	$\omega_2^4 \pm g_n \omega_2^4$

Table II: Coefficients of the first column of Routh array for active damping of the higher-order non-collocated mode using a 2nd-order HPF with both positive and negative feedback signs.

	Negative Feedback	Positive Feedback
a_4	1	1
a_3	$2\omega_2(\zeta_2 + \zeta_c)$	$2\omega_2(\zeta_2 + \zeta_c)$
b_1	$\omega_2^2(4\zeta_2\zeta_c + 1)$	$\omega_2^2(4\zeta_2\zeta_c + 1)$
c_1	$-\frac{2\omega_2^3(g_n - 4\zeta_2\zeta_c)(\zeta_2 + \zeta_c)}{4\zeta_2\zeta_c + 1}$	$\frac{2\omega_2^3(g_n + 4\zeta_2\zeta_c)(\zeta_2 + \zeta_c)}{4\zeta_2\zeta_c + 1}$
a_0	$\omega_2^4(g_n + 1)$	$\omega_2^4(1 - g_n)$

The active damping control loop utilizing a second-order high-pass filter in positive feedback (HP-PPF) is shown in Figure 6b. The damping is tuned using gain parameter g , which for mathematical brevity is normalized to g_n , such that the open-loop response has unity gain, i.e., $|G_p(i\omega) \cdot g_n \cdot HPF(i\omega)|_{\omega=0} = 1$. The resulting HP-PPF controller is given by

$$C_d(s) = g_n \cdot \frac{s^2}{s^2 + 2\zeta_c\omega_c s + \omega_c^2} \quad (7)$$

where ω_c equals the frequency of the higher-order resonance mode to be damped. The effective damping is then determined by the damping ratio ζ_c and the normalized feedback gain g_n of the controller. The resulting closed damping loop is described by:

$$CL_d(s) = \frac{y}{d} = \frac{G_p(s)}{1 - G_p(s)C_d(s)}. \quad (8)$$

Based on the closed-loop transfer function, the closed-loop damping ratio, as derived in Appendix B, can be expressed as

$$\zeta_{CL_d} = \zeta_2 + \frac{g_n}{4\zeta_c}, \quad (9)$$

demonstrating an increase in the effective closed-loop damping ratio when $g_n > 0$ and $\zeta_c > 0$. This underscores the effectiveness of the HP-PPF controller in improving the damping characteristics of the higher-order non-collocated mode. It is important to note that this equation holds specifically at the resonance frequency. While a combination of high gain (g_n) and low damping (ζ_c) can reduce the magnitude at the exact resonance frequency, it also results in peak splitting, limiting the overall peak reduction. When tuning g_n and ζ_c the phase requirements outlined in [16] should be taken into account.

The open-loop response depicted in Figure 8.a shows the resulting phase margins (φ_{mi}) at both crossover frequencies (ω_{xi}), which can be tuned with control parameter ζ_c . Meanwhile, the closed-loop response shown in Figure 8.b demonstrates the attenuation of the non-collocated resonance peak with the proposed HP-PPF active damping control architecture.

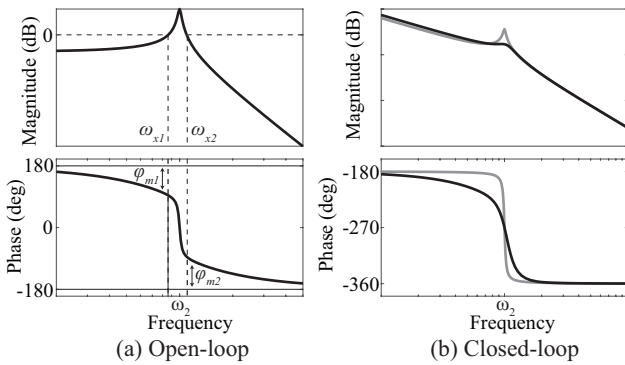


Figure 8: HP-PPF active damping control (black) of higher-order non-collocated mode (grey).

As detailed in Appendix A, the Routh-Hurwitz stability criterion indicates that the damping loop using the HP-PPF is stable when the condition $0 < g_n < 1$ is satisfied.

IV. ACTIVE DAMPING CONTROL OF DUAL-STAGE POSITIONING SYSTEMS

A. Combining Active Damping Control and Motion Control

The preceding section demonstrated the effectiveness of the HP-PPF active damping in attenuating a higher-order parasitic mode. This method can be effectively implemented in a single-axis dual-stage positioning system to suppress its undesired mode. The remainder of this paper focuses on applying the proposed active damping control method to two-degrees-of-freedom positioning systems as a case study. However, as previously shown, the solution is adaptable and can be applied to the second mode of any higher-order system.

To simultaneously achieve damping and tracking control, commonly a dual-loop control architecture is utilized [26, 30], integrating motion control and active damping control, as depicted in Figure 9.

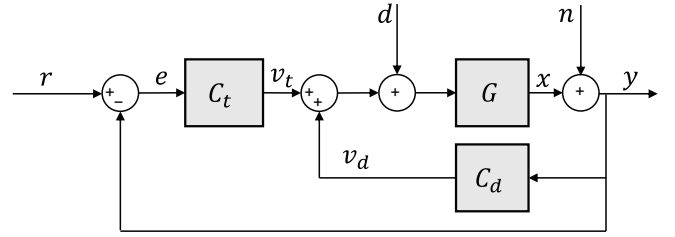


Figure 9: Dual-loop architecture incorporating motion control and active damping control

The control architecture features two distinct loops: an outer feedback loop utilizing a tracking controller (C_t), typically a tamed PID controller, to achieve accurate motion tracking, and an inner feedback loop that incorporates an active damping controller (C_d). In the proposed HP-PPF solution, the inner loop uses a second-order high-pass filter within a positive feedback configuration to actively dampen the higher-order parasitic mode. The dual-stage positioning system (G) is represented by the transfer function in Equation (3), which corresponds to the double-mass-spring-damper system in Figure 1. The dual closed-loop transfer function is given by:

$$CL(s) = \frac{GC_t}{1 + G(C_t - C_d)} \quad (10)$$

where the inner closed damping loop is described by Equation (8). The standard tamed PID controller is defined as follows

$$C_{PID}(s) = k_p \underbrace{\left(1 + \frac{\omega_i}{s}\right)}_{\text{Integrator}} \underbrace{\left(1 + \frac{s}{\omega_d}\right)}_{\text{Lead}} \underbrace{\left(1 + \frac{s}{\omega_t}\right)}_{\text{Lag}}^{-1} \underbrace{\left(\frac{\omega_l}{s + \omega_l}\right)}_{\text{LPF}} \quad (11)$$

where k_p is the proportional gain that defines the open-loop crossover frequency ω_x , i.e. open-loop bandwidth. The frequency ω_i is where integral action stops and ω_d is the frequency at which derivative action begins, thereby introducing a phase lead at crossover. The frequency ω_t indicates where the derivative action is tamed to prevent the amplification of high-frequency noise. The cutoff frequency of the low-pass filter (LPF), denoted by ω_l , ensures the further suppression of high-frequency noise and unmodeled higher-order system dynamics. The various frequency bands are computed as follows [31]:

$$\begin{aligned} \omega_d &= \frac{\omega_x}{3} \quad , \quad \omega_t = 3\omega_x \quad , \quad \omega_i = \frac{\omega_x}{10} \\ \omega_l &\geq 10\omega_x \quad , \quad k_p = 0.33 \left| \frac{1}{G(i\omega_x)} \right| \end{aligned} \quad (12)$$

The PID tracking controller is designed to ensure stability and robustness by achieving sufficient gain margin ($GM \geq 6\text{dB}$) and phase margin ($PM \geq 30^\circ$) in open-loop.

B. Stability of Inner Closed Damping Loop

Active damping is achieved in the inner loop of the dual-loop control architecture, as shown in Figure 9. The stability of the active damping loop was previously analyzed for the

simplified system $G_p(s)$, where the rigid-body mode was neglected. However, in the dual-stage positioning system, the dynamics are governed by the fourth-order transfer function in Equation (3), where the rigid-body mode cannot be ignored. This suggests that the stability condition of the inner active damping loop, derived earlier, may be affected by the presence of the rigid-body mode.

The characteristic equation of the inner closed damping loop, considering the fourth-order system dynamics and HP-PPF control, is worked out in Appendix C. Based on the necessary condition from the Routh-Hurwitz criterion for closed-loop stability, the following condition emerges:

$$0 < g_n < \underbrace{4\zeta_2\zeta_c + n^2 + 4n\zeta_1\zeta_2 + 4n\zeta_1\zeta_c + 2}_k \quad (13)$$

The factor denoted with k can be approximated as $k \approx n^2 + 2$ due to the typically small values of ζ . This factor compensates for the modal gain variation leading to further spaced modes. Since the modal gains of higher-order modes are relatively low compared to the primary mode, the intersection between the rigid-body mode and the higher-order mode becomes more spaced. The spacing between the modes (n) is directly related to the gain of the higher-order mode relative to the primary mode, as described by Equation (1).

According to the gain criterion outlined in [16], the open-loop gain of the active damping loop must peak above 0 dB, leading to two crossover frequencies, to reduce sensitivity at resonance and therewith enhance the damping characteristics of the mode. When the modes are further separated, the relatively lower modal gain of the higher-order mode necessitates a higher gain in the damping controller (g_n), which is essentially described by factor k , to meet this criterion for effective active damping. To simplify the formulation, the gain of the active damping controller is adjusted to account for this modal gain dependency, such that $g_k = k \cdot g_n$, resulting in the following expression for the active damping controller:

$$C_d(s) = g_k \cdot \frac{s^2}{s^2 + 2\zeta_c\omega_c s + \omega_c^2}. \quad (14)$$

Upon re-evaluation of the characteristic equation with compensated gain g_k (Appendix C), a necessary stability condition for the damping loop emerges as $0 < g_k < 1$, independent of n . This condition underscores the role of k in compensating for the modal gain difference.

However, even with the inclusion of $k \approx n^2 + 2$ in the HP-PPF controller, the stability of the inner damping loop remains influenced by the spacing between the two modes. The open-loop responses in Figure 10 illustrate the application of the same HP-PPF controller, which satisfies the condition in Equation (13), to two systems with different mode spacing. In this example, the active damping controller achieves a stable closed damping loop when $n = 25$, but leads to an unstable closed damping loop when $n = 15$. This illustrates that closer spacing between the rigid-body and higher-order mode

increases the likelihood of destabilizing the inner damping loop.

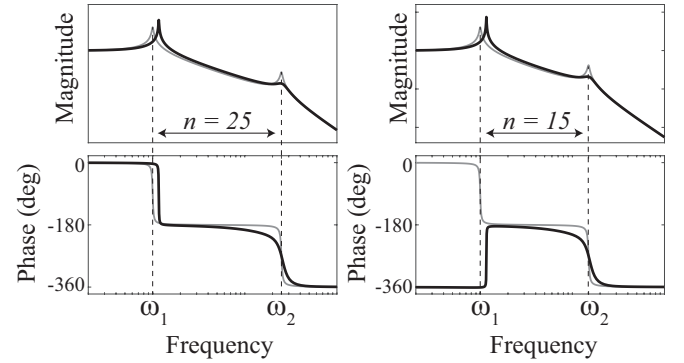


Figure 10: Closed inner active damping loop using same HP-PPF controller is stable when mode spacing $n = 25$ and unstable when $n = 15$

The root-locus plot in Figure 11 illustrates that the closed-loop poles associated with the first resonance mode (ω_1) in the right-half-plane (RHP) shift to more negative real values as n increases, retaining stability of the inner closed-loop system, as those system poles initially lie in the RHP. This indicates that when the modes are closely spaced, the active damping controller can destabilize the closed-loop poles of the first resonance mode. The larger angle between the real axis and the closed-loop pole trajectories corresponding to the second mode (ω_2) reflects an increase in the damping ratio of this mode. Note that this angle, and consequently the damping ratio, remains constant as n varies.

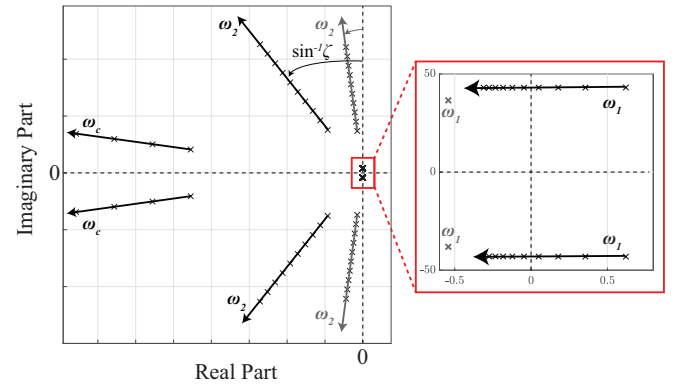


Figure 11: Trajectories of closed damping loop poles (black) and system poles (grey) for increasing values of n

The instability of the inner damping loop is not a significant concern, as tracking controllers, such as PID controllers, are commonly used in motion control to stabilize otherwise unstable systems [29]. Similarly, in cases where the inner active damping loop becomes unstable due to closely spaced resonance modes, a PID controller can stabilize the system by shifting the unstable poles to the left-half-plane. In the frequency domain, this stabilization can be visualized through the derivative (D) action of the PID controller, which introduces an additional phase lead of approximately 45° at the

crossover frequency [29]. This phase lead effectively raises the phase above -180° at crossover, ensuring system stability and providing sufficient phase margin. The outer open-loop response in Figure 12 of the control architecture in Figure 9, represented by $C_t \cdot CL_d$, demonstrates how a standard tamed PID controller adds phase lead at crossover (ω_x), retaining stability of the outer closed-loop system.

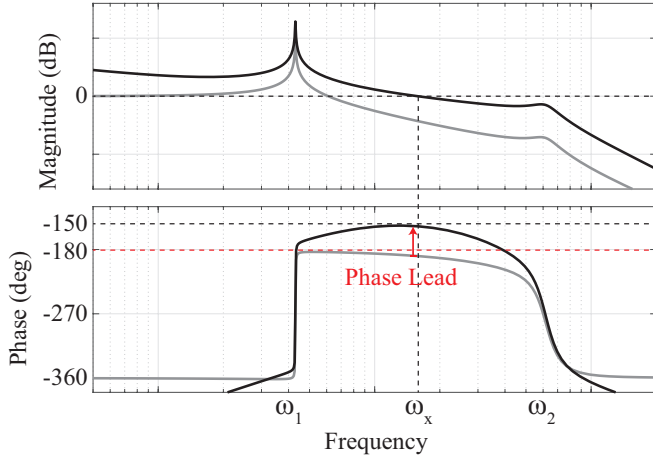


Figure 12: Added phase at crossover in open-loop response $C_t \cdot CL_d$ (black), representing PID controller combined with the unstable inner damping loop (grey)

Figure 13 illustrates the stability of both the inner damping loop and the outer closed-loop with the PID tracking controller, as a function of the HP-PPF controller feedback gain (g_k) and the mode spacing (n). The blue region represents combinations of g_k and n where the inner closed damping loop remains stable. In contrast, the grey region indicates where the inner closed-loop is unstable, but the PID controller, when properly tuned to introduce phase lead at crossover according to the design rules in Equation (12), stabilizes the overall closed-loop system. As n increases, the stable region converges towards $g_k = 1$, in line with the derived Routh-Hurwitz stability condition. It is important to note that this plot assumes a fixed damping control parameter ζ_c set to 0.3, and the PID controller is tuned based on standard rules-of-thumb (Equation (12)).

C. Control Parameter Tuning

The performance of the dual closed-loop system is primarily determined by the three control parameters of the HP-PPF controller, which provides active damping, together with the desired crossover frequency input of the PID controller (Equation (12)). The cut-off frequency of the second-order high-pass filter (ω_c) used in HP-PPF is specifically tuned to the frequency of the mode to be damped, which is 78 Hz in the presented experimental setup. Increasing the damping of the controller leads to greater peak attenuation, however, this comes at the cost of increased phase lag, which limits the maximum achievable control bandwidth. Thus, a trade-off between peak attenuation and the resulting maximum control

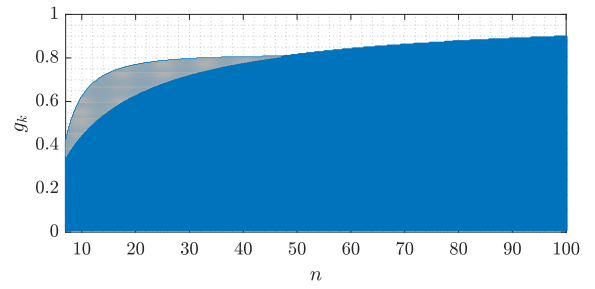


Figure 13: Stability regions as a function of g_k and n ($\zeta_c = 0.3$), indicating where both the inner damping loop and outer closed-loop are stable (blue), and the region where the inner damping loop is unstable but the outer closed-loop with the PID tracking controller becomes stable (grey)

bandwidth complicates the parameter tuning process. Simultaneous design of control parameters in a dual-loop architecture through optimization has proven significantly more effective than the sequential design of the damping controller and tracking controller [26].

To simultaneously determine the control parameters for both the damping and tracking controller (g_k , ζ_c , and ω_x respectively), a gradient-based optimization method utilizing the sequential quadratic programming (SQP) algorithm is employed [32]. The optimization aims to maximize the open-loop bandwidth (crossover frequency ω_x) of the dual-loop, under the constraints of maintaining sufficient gain and phase margin. The objective function is normalized by scaling the crossover frequency ω_x relative to the frequency of the higher-order parasitic mode ω_2 , making the objective function dimensionless. The optimization problem is formulated as follows:

$$\begin{aligned} \min_{\mathbf{x}} \quad & -\frac{\omega_x(\mathbf{x})}{\omega_2} \\ \text{subject to} \quad & GM(\mathbf{x}) - 6\text{dB} \geq 0 \\ & PM(\mathbf{x}) - 30^\circ \geq 0 \\ \text{and} \quad & 0 < g_k < 1 \\ & 0 < \zeta_c < 1 \\ & \omega_1 < \omega_x < \omega_2 \end{aligned}$$

$$\text{where } \mathbf{x} = (g_k, \zeta_c, \omega_x)^T$$

$$|L(\omega_x, \mathbf{x})| = |C_t(\omega_x, \mathbf{x}) \cdot CL_d(\omega_x, \mathbf{x})| = 0$$

The optimization process is employed to determine the control parameters that achieve maximum open-loop bandwidth for damping and tracking control of the identified frequency response of the experimental setup (Figure 4). This results in $g_k = 0.2618$, $\zeta_c = 0.7185$ and $\omega_x = 25\text{Hz}$.

D. Attenuating Feedback Noise using Band-Pass Filter

The high-pass active damping controller lacks roll-off beyond its cut-off frequency, which can amplify high-frequency noise present in practical applications. This noise amplification increases power demands, potentially causing the amplifier to overheat, saturate, or produce distorted output, ultimately degrading system performance and lifespan.

Mathematically, the signal entering the amplifier through the inner feedback loop can be represented as $\frac{v_d}{y} = C_d(s)$, which simplifies to $v_d = C_d \cdot n$ in the context of noise n . At high frequencies, where noise becomes predominant, the noise entering the amplifier through the inner feedback loop can be expressed as:

$$v_d = \lim_{s \rightarrow \infty} C_d(s) \cdot n \approx g_k \cdot n \quad (15)$$

This emphasizes the importance of high-frequency roll-off in the damping controller to reduce the magnitude of the high-frequency component of the transfer function.

To address this issue, a low-pass filter can be introduced, which provides high-frequency roll-off and effectively transforms the damping controller into a band-pass filter, as illustrated in Figure 14 for the case where the width of the band-pass α is set to 10. Depending on the required high-frequency roll-off, a higher-order low-pass filter may be utilized.

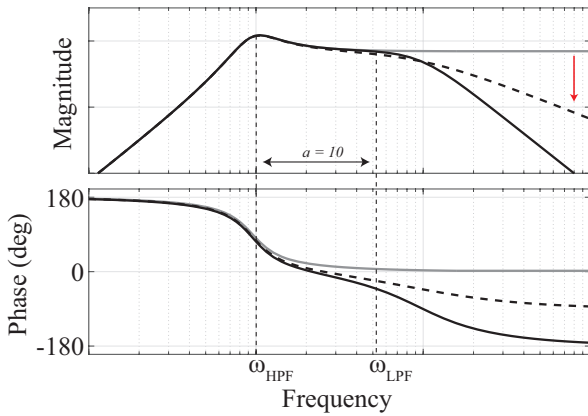


Figure 14: Second-order HPF (grey) with added first-order LPF (black-dotted) and second-order LPF (black)

The band-pass active damping controller can be mathematically represented as follows:

$$C_d(s) = g_k \cdot \frac{s^2}{s^2 + 2\zeta_c \omega_c s + \omega_c^2} \cdot \left(\frac{\omega_{LPF}}{s + \omega_{LPF}} \right)^m \quad (16)$$

where m denotes the order of the low-pass filter, and $\omega_{LPF} = \alpha \cdot \omega_c$.

However, placing a low-pass filter too close to the high-pass filter of the HP-PPF controller can adversely affect the effective damping performance. This relative distance between the individual cut-off frequencies is described by the width of the resulting band-pass filter, denoted by α .

Appendix D provides a mathematical proof demonstrating that the damping performance is impacted by α , particularly in the case of using a second-order low-pass filter for noise attenuation. This highlights the need for careful tuning of the low-pass filter frequency, as a trade-off arises between effective damping performance and high-frequency noise attenuation.

In the practical application presented in this paper, α is set to 10 to ensure that the damping performance of the HP-PPF remains unaffected, as this is the primary objective. For the

proper tuning of α , methods such as dynamic error budgeting can be utilized [33].

V. EXPERIMENTAL IMPLEMENTATION

The proposed HP-PPF active damping controller, with parameters optimized for the experimental setup and added low-pass filter for noise attenuation, is implemented in real-time by discretizing the continuous-time controller using the Tustin method (bilinear transformation). The selected control parameters, tuned to achieve maximal open-loop bandwidth, and the closely spaced modes result in an unstable inner damping loop. The introduced tamed PID controller stabilizes the outer closed-loop system. Following this, a closed-loop system identification is conducted. By dividing the used PID controller out of the measured transfer function, the frequency response of the inner damping loop can be isolated, which is illustrated in Figure 15. The results demonstrate a significant reduction ($\sim 16dB$) of the parasitic resonance peak. The primary resonance mode ω_1 is shifted from 6 Hz to 7.5 Hz in the closed damping loop response, yet it remains sufficiently below the crossover frequency ω_x .

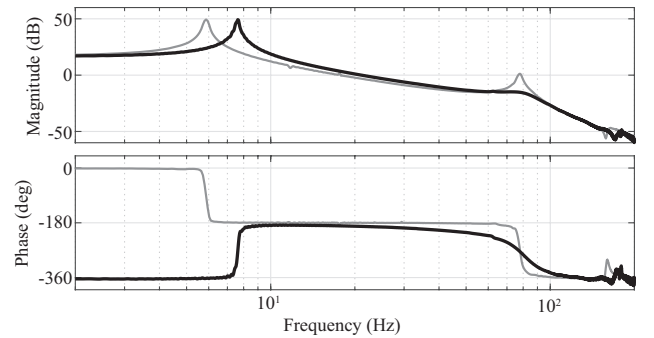


Figure 15: Experimentally identified inner closed damping loop CL_d (black) and identified frequency response of experimental setup (grey)

To demonstrate the benefits of implementing HP-PPF active damping control, an experimental comparison is conducted across three scenarios. In each case, the controllers are designed to achieve maximum open-loop bandwidth while maintaining stability and robustness margins. The performance of these three cases will be compared and evaluated throughout the remainder of this paper.

In the first scenario, only a tamed PID controller (C_t) is employed for tracking control, leaving the parasitic resonance undamped, as represented by the control architecture in Figure 16.a. This configuration yields a maximum open-loop bandwidth of 12 Hz, limited by the higher-order non-collocated resonance. In the second scenario, a conventional notch filter (N), described in Equation (17), is introduced, as illustrated in Figure 16.b.

$$N(s) = \frac{s^2 + \frac{2\zeta_N}{Q}s + \omega_N^2}{s^2 + 2\zeta_N s + \omega_N^2} \quad (17)$$

The notch filter is tuned to reduce the parasitic resonance peak to a level comparable to that of the active damping

controller with similar phase lag, resulting in a maximum open-loop bandwidth of 22 Hz. Finally, in the third scenario, the dual-loop architecture shown in Figure 16 incorporates the optimized HP-PPF controller, achieving an open-loop bandwidth of 25 Hz.

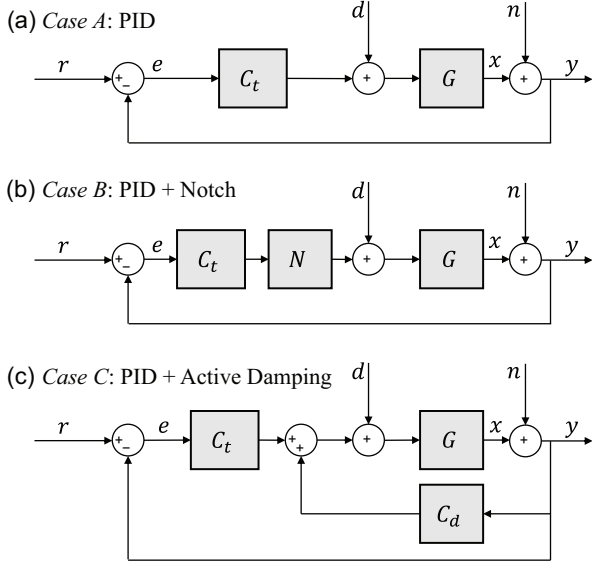


Figure 16: (a) Control architecture for standard tracking control, (b) Control architecture for tracking control with notch filter, (c) Dual-loop control architecture employing active damping control and tracking control

The tuned control parameters, resulting open-loop bandwidths and stability margins for the three cases are presented in Table III. The corresponding experimental open-loop frequency responses are shown in Figure 17. This comparison illustrates that the HP-PPF active damping control architecture can achieve open-loop bandwidths and stability margins comparable to those of an industry-standard notch filter-based architecture, which will be further discussed in Section V-C.

Table III: Control parameters, open-loop bandwidth and corresponding margins for three cases presented in Figure 16

	Control Parameters	0 dB Crossover	GM	PM
Case A	—	12 Hz	13 dB	37°
Case B	$Q = 7, \zeta_N = 0.15$	22 Hz	6 dB	30°
Case C	$g_k = 0.26, \zeta_c = 0.71$	25 Hz	6 dB	30°

A. Disturbance and Noise Attenuation Performance

The preceding section demonstrated the practical implementation of the novel active damping control method, showing that it can achieve control bandwidth improvements comparable to those obtained with an industry-standard notch filter. However, the primary objective of this novel approach is not to exceed the bandwidth achieved with standard solutions, but rather to provide an alternative that addresses the inherent limitations of notch filters. While notch filters effectively enhance control bandwidth by attenuating parasitic resonance in the closed-loop response, their impact on disturbance rejection remains

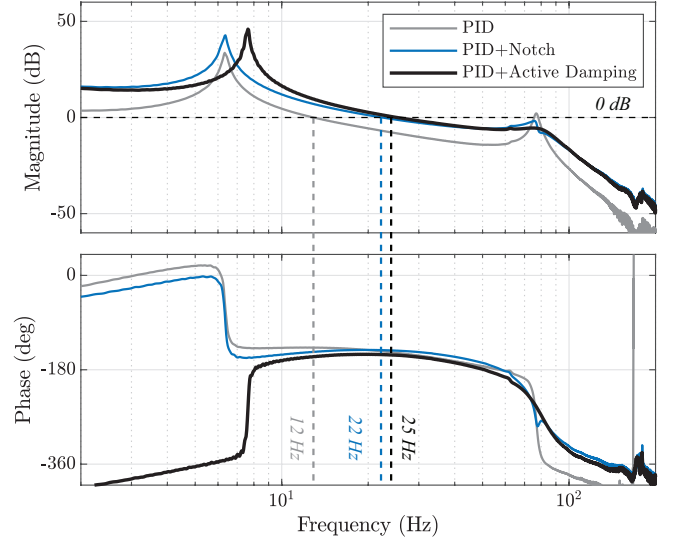


Figure 17: Experimentally identified open-loop response indicating 0 dB crossover frequencies for three comparison cases

limited, as the effect of the parasitic resonance is still noticeable in the closed-loop disturbance rejection [15].

The dual closed-loop process sensitivity function, which describes disturbance rejection when implementing active damping control, denoted as PS_{ADC} , can be determined by

$$PS_{ADC} = \frac{y}{d} = \frac{G}{1 + G(C_t - C_d)} = \frac{G_d}{1 + G_d C_t} \quad (18)$$

Here, the inner active damping loop from Equation (8) is represented by an equivalent plant (G_d), incorporating the damped parasitic mode. In practice, a notch filter (N) can be implemented to obtain similar peak attenuating in the open-loop around the frequency of the higher-order parasitic mode (ω_2) and thus

$$|G_d(i\omega)| = \left| \frac{G(i\omega)}{1 - G(i\omega)C_d(i\omega)} \right| = |G(i\omega) \cdot N(i\omega)| \Big|_{\omega=\omega_2} \quad (19)$$

The closed-loop process sensitivity when using the notch filter, denoted as PS_N , can be calculated as follows

$$PS_N = \frac{G}{1 + GNC_t} \quad (20)$$

Combining Equation (19) and Equation (20) gives:

$$|PS_N(i\omega)| \approx \left| \frac{G(i\omega)}{1 + G_d(i\omega)C_t(i\omega)} \right| \Big|_{\omega=\omega_2} \quad (21)$$

The ratio of the two process sensitivity functions, as derived in Appendix E, can be expressed as:

$$\frac{|PS_{ADC}|}{|PS_N|} = |N|_{\omega=\omega_2} < 1 \quad (22)$$

As demonstrated by Equation (22), the implementation of active damping control results in a reduced process sensitivity around the frequency of the higher-order parasitic mode, indicating better disturbance rejection, which is not achieved when using a notch filter.

This reduction around the parasitic resonance is clearly observed in the experimentally obtained process sensitivity frequency responses in Figure 18, where the parasitic mode remains present when a notch filter is employed. At low frequencies, both the active damping control architecture and notch filter architecture reduce the process sensitivity due to the higher gains of the tracking controllers C_t .

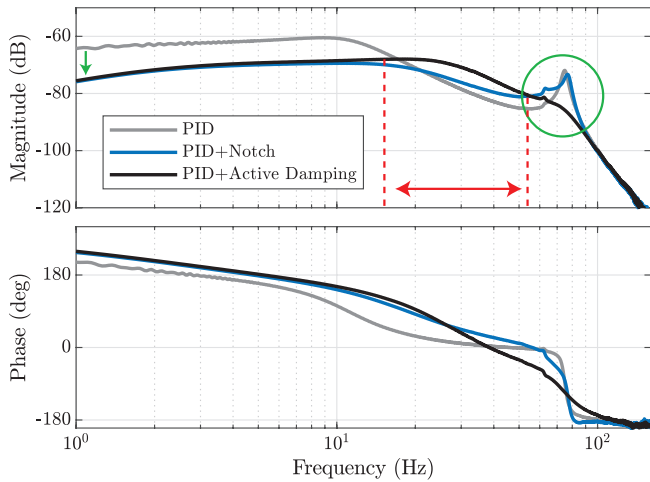


Figure 18: Experimentally identified closed-loop process sensitivity responses for three comparison cases

The active damping architecture demonstrates significantly reduced process sensitivity around the frequency of the parasitic mode, compared to the notch filter architecture. In multi-degree-of-freedom positioning stages that use multiple actuators and sensors (MIMO), actuation in one degree of freedom can introduce disturbances into the other degree of freedom of the system, particularly at this parasitic mode frequency (ω_2). This effect is evident in the cross-coupling transfer function of a MIMO positioning system, as illustrated in Figure 19.

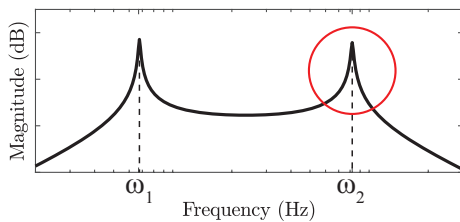


Figure 19: Magnitude of cross-coupling frequency response x_2/F_1 in MIMO positioning system; transfer function from actuator at m_1 to position of m_2

To replicate such cross-coupling disturbance, a multisine signal, composed of several frequencies around the parasitic mode, is applied as an external process disturbance to the

closed-loop system. This multisine signal includes components at 76 Hz and 80 Hz to illustrate the system's ability to reject disturbances at frequencies close to the parasitic mode. The multisine disturbance signal $d(t)$ can be expressed as:

$$d(t) = A\sin(2\pi \cdot 76t) + A\sin(2\pi \cdot 80t) \quad (23)$$

where A represents the amplitude of the sine waves. The resulting output response, normalized with the input amplitude A , depicted in Figure 20, clearly illustrates the superior disturbance rejection achieved with the implementation of active damping control.

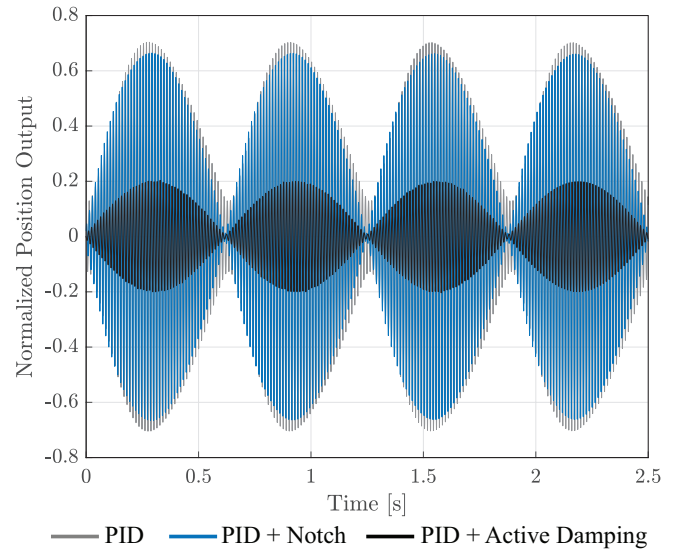


Figure 20: Process disturbance rejection of multisine signal $d(t)$ for three comparison cases

In the experimentally obtained sensitivity responses shown in Figure 21, there is a noticeable reduction in sensitivity around the frequency of the parasitic mode when using active damping control compared to the notch filter. This reduction indicates improved noise rejection near this frequency. While a deeper notch could enhance the noise rejection at this frequency, it would come at the expense of increased phase lag and reduced system robustness. To illustrate the noise rejection capability in this frequency region, a multisine signal is introduced as an output disturbance, in addition to the existing sensor noise n_s in the setup. The noise signal is defined as:

$$n(t) = n_s(t) + B\sin(2\pi \cdot 76t) + B\sin(2\pi \cdot 80t) \quad (24)$$

where B represents the amplitude of the sine waves. The rejection of this noise signal is depicted in Figure 22, which shows the normalized time-domain response to the noise signal. The active damping control architecture outperforms the notch filter architecture in rejecting noise near the second resonance mode.

The proposed HP-PPF active damping control architecture demonstrates superior disturbance and noise rejection around the frequency of the higher-order parasitic mode compared to the notch filter-based solution. However, as shown in Figures 18 and 21, there is an increase in gain of both the process

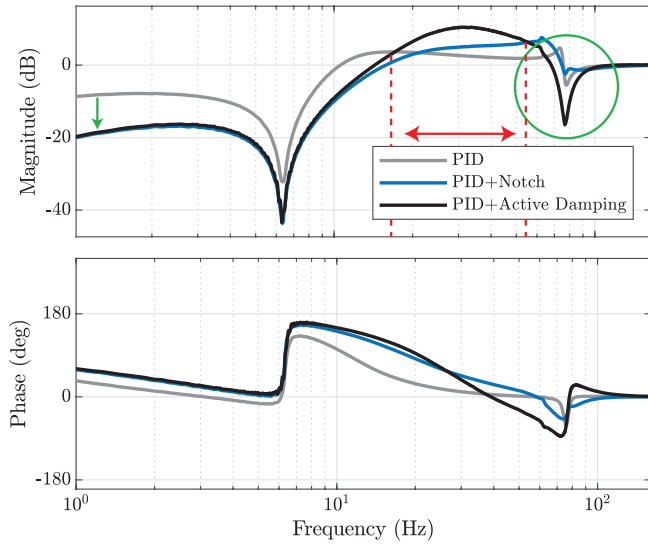


Figure 21: Experimentally identified closed-loop sensitivity responses for three comparison cases

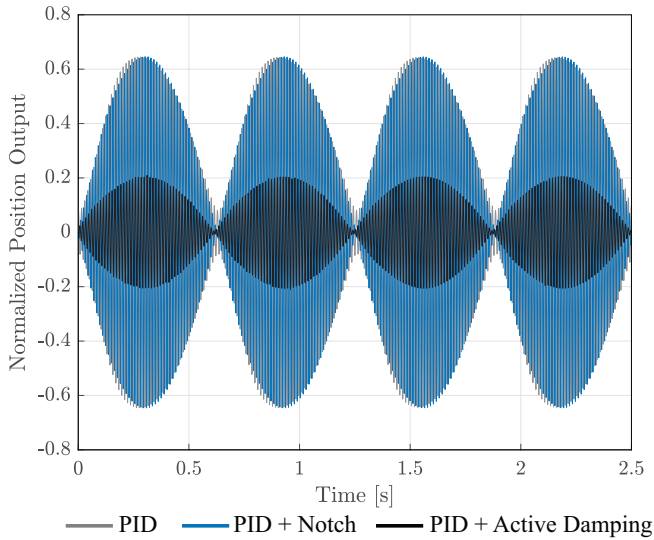


Figure 22: Rejection of noise signal $n(t)$ for three comparison cases

sensitivity and sensitivity functions in the frequency range between the rigid-body mode (ω_1) and the higher-order mode (ω_2) when using active damping control. This increase is attributed to spillover effects within the inner damping loop, which can be mitigated by reducing the gain g_k of the damping controller. Consequently, a trade-off arises between reducing the parasitic resonance peak and increasing (process) sensitivity in this frequency range. This suggests that in certain situations, depending on the disturbance and noise profiles, the active damping control approach may not always provide better disturbance and noise rejection.

B. Robustness to Model Uncertainty

A major drawback of the notch filter-based solution is its sensitivity to model uncertainties. The notch filter must be pre-

cisely tuned to the exact frequency of the parasitic resonance. Any deviation in the actual resonance frequency from the model can severely degrade the filter's performance, leading to increased disturbance errors, restricted control bandwidth, and potentially inducing instability.

In contrast, while the HP-PPF controller also requires alignment with the parasitic resonance mode, it achieves damping primarily through phase adjustment, as illustrated in Figure 8. This feedback approach offers greater robustness against parameter variations. The notch filter mitigates the resonance by attenuating its gain, making it more susceptible to parameter variations. Although increasing the damping ratio of a notch filter can enhance robustness, it introduces additional phase lag, further restricting control bandwidth. Therefore, a trade-off exists between robustness to model uncertainty and control bandwidth in the case of a notch filter-based architecture, a trade-off that is significantly less pronounced with the novel active damping approach.

Both the notch filter and active damping controller incorporate control parameters associated with their damping ratio, which can be increased to improve robustness. As illustrated in Figure 17, both controllers are tuned to achieve similar phase lag in their open-loop responses. Since both methods effectively attenuate the resonance peak, the introduced phase lag now becomes the limiting factor for the control bandwidth, rather than the resonance peak itself. It is important to note that increasing the damping ratio, whether for the notch filter or the active damping controller, intended to improve robustness leads to increased phase lag, ultimately reducing the achievable bandwidth.

The experimental setup includes fixed resonance modes that cannot be easily modified. However, resonance mode uncertainty can be simulated by adjusting the frequency location of the notch filter and HP-PPF controller. The target frequencies of both controllers (ω_c and ω_N), which are typically set equal to the frequency of the target mode (ω_2), are shifted by a factor δ :

$$\hat{\omega}_c = \omega_2 + \delta \cdot \omega_2, \quad \hat{\omega}_N = \omega_2 + \delta \cdot \omega_2 \quad (25)$$

The impact of this added uncertainty on the performance of the active damping control architecture and the notch-based approach can be observed using closed-loop system identification. Figure 23 presents the closed damping loop response ($CL_d(s)$) and the open-loop notch response ($N(s) \cdot G(s)$) under different levels of resonance uncertainty. The results demonstrate the superior robustness of the active damping controller compared to the notch filter when faced with resonance mode uncertainty.

The closed-loop tracking responses to a step reference in Figure 24 demonstrate that the control architecture with a notch filter tends towards instability as the mismatch between the notch frequency and the resonance grows. In contrast, the active damping controller maintains consistent performance, showing no signs of degradation under variations in the resonance frequency within the considered range.

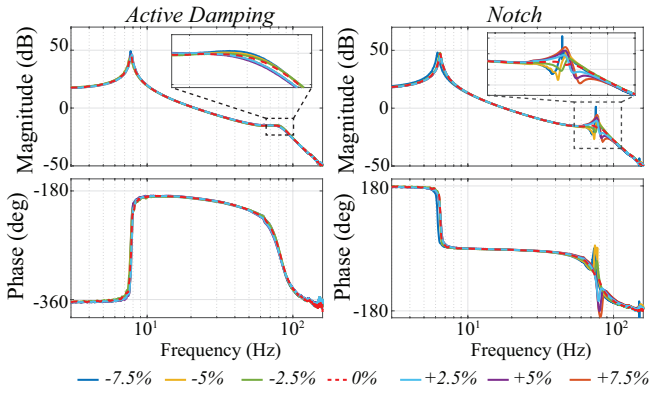


Figure 23: Effectiveness of active damping control and notch filter under varying percentages of resonance frequency uncertainty

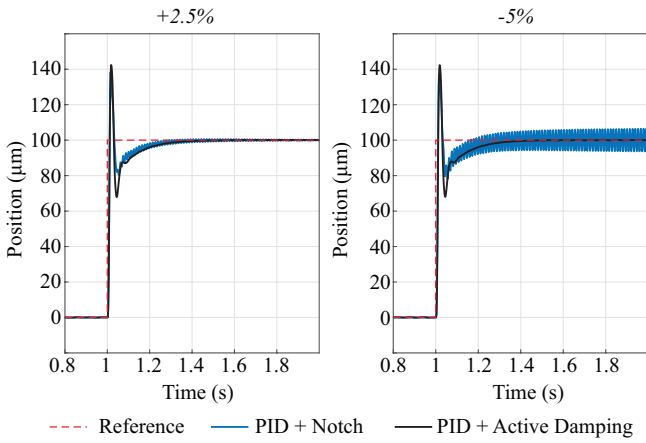


Figure 24: Two illustration cases of closed-loop step reference tracking under varying percentages of resonance frequency uncertainty δ

C. Reference Tracking Performance

The tracking response to a step reference signal on the closed-loop system is presented in Figure 25. Implementing the active damping control architecture allows for a significant bandwidth improvement compared to the undamped case, which is evident in the step response as it exhibits a 67% reduction in settling time. A similar bandwidth and reference tracking profile is achieved with the notch filter control architecture. It is important to note that the active damping and the notch responses yield a higher overshoot than the undamped response. This is attributed to the difference in phase margin (Table III); however, both responses maintain a sufficiently robust phase margin of 30° .

Triangular waves consist of a fundamental frequency component and its harmonics, making them widely used in several positioning applications [26, 34]. To evaluate the tracking performance of the system, triangular wave tracking experiments are conducted at different fundamental frequencies, as illustrated in Figure 26. The time delay between the reference signal $r(t)$ and the measured

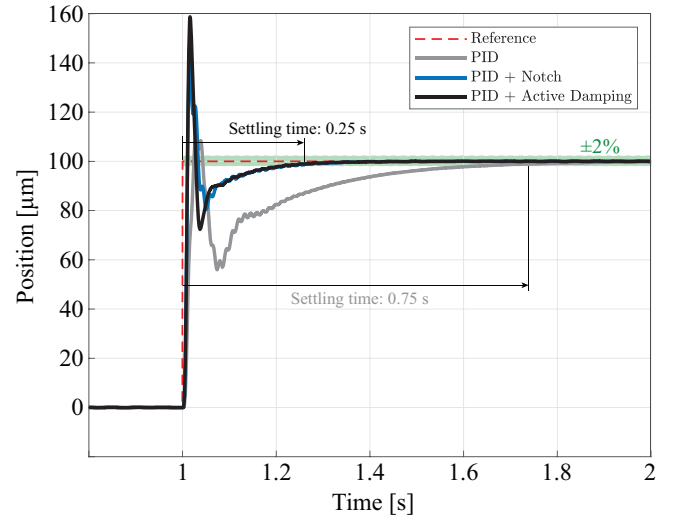


Figure 25: Experimental tracking response to step reference for three comparison cases

displacement $y(t)$ can be corrected through data post-processing [35]. The delay-compensated displacement $\hat{y}(t) = y(t - d)$ is used, where the delay d is determined by the closed-loop phase lag (ϕ), calculated as $d = \phi / (f \cdot 360)$. The calculated delay is multiplied by the sampling frequency and rounded to the nearest integer due to discrete sampling. Two performance metrics are introduced to quantify the tracking results, with the reference signal denoted by $r(t)$ and the shifted output by $\hat{y}(t)$: (1) maximum tracking error

$$e_{\max} = \frac{\max_{t \in [0, 2T]} |r(t) - \hat{y}(t)|}{\max(r(t)) - \min(r(t))} \times 100\% \quad (26)$$

and (2) root-mean-square (RMS) tracking error

$$e_{\text{RMS}} = \frac{\sqrt{\frac{1}{2T} \int_0^{2T} (r(t) - \hat{y}(t))^2 dt}}{\max(r(t)) - \min(r(t))} \times 100\% \quad (27)$$

Table IV provides a summary of the tracking errors for the three closed-loop architectures. The active damping control architecture achieves performance comparable to that of the notch architecture. However, since both control architectures are tuned to achieve maximum open-loop bandwidth, their implementations exhibit non-flat outer closed-loop responses. This non-flatness results in performance variations when compared to the undamped case. To enhance the tuning of the active damping controller, additional closed-loop flatness constraints can be incorporated into the cost function of the optimization algorithm. Nonetheless, this experiment serves as a proof-of-concept, showcasing the comparable performance of both the active damping control and notch filter architectures.

Table IV: Normalized triangular wave reference tracking errors for three comparison cases

	2Hz		5Hz		10Hz		15Hz	
	ϵ_{\max}	ϵ_{RMS}	ϵ_{\max}	ϵ_{RMS}	ϵ_{\max}	ϵ_{RMS}	ϵ_{\max}	ϵ_{RMS}
PID	12.0%	7.1%	11.0%	4.6%	13.1%	9.1%	6.8%	4.2%
PID + Notch	3.9%	2.5%	4.7%	2.7%	12.2%	6.0%	17.3%	10.9%
PID + Active Damping	4.0%	2.7%	5.1%	3.1%	12.6%	5.9%	18.5%	11.5%

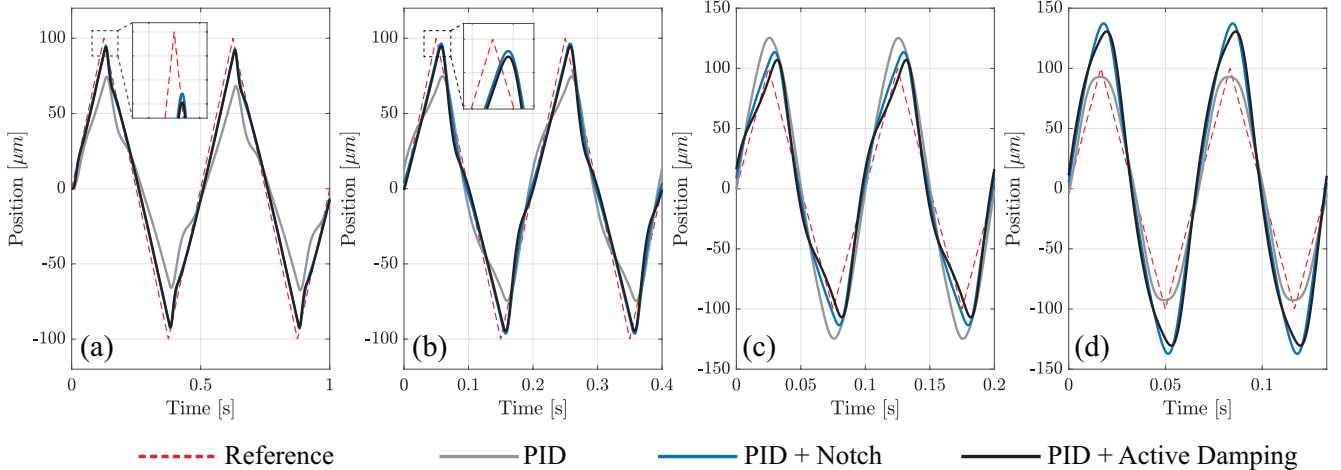


Figure 26: Triangular wave tracking results under fundamental frequencies of a.) 2 Hz, b.) 5 Hz, c.) 10 Hz and d.) 15 Hz

VI. CONCLUSION

This research introduces a novel active damping control method designed to suppress higher-order resonance modes in positioning systems. By incorporating a second-order high-pass filter within a positive feedback loop (HP-PPF), the approach specifically targets higher-order parasitic modes, which typically introduce unwanted vibrations and reduce positioning accuracy. The proposed method effectively enhances the damping characteristics of these undesired modes. To demonstrate the contributions of this work, the proposed active damping control is integrated into a dual-loop configuration that operates in parallel with a PID controller for tracking control. This configuration provides active damping for a non-collocated dual-stage positioning system, where the dominant higher-order non-collocated resonance not only contributes to disturbance errors but also significantly limits control bandwidth. Through simultaneous optimization of both the active damping and tracking controllers, the dual-loop architecture shows improved disturbance rejection and noise suppression at the frequency of the higher-order parasitic mode, as well as enhanced robustness against model uncertainties, overcoming the limitations of traditional notch filters. The active damping control solution achieves control bandwidth and tracking performance comparable to that of a notch filter-based architecture. A mathematical framework was developed to generalize these contributions, which were experimentally validated using a single-axis dual-stage compliant positioning system as a proof-of-concept setup.

The proposed active damping strategy can be further extended to provide effective damping for the second resonance mode

of any higher-order system. Although the experimental implementation shows successful feedback noise attenuation with a second-order low-pass filter, optimizing the tuning of the low-pass filter frequency is recommended. This optimization should account for the trade-off between damping performance and noise attenuation, which can be achieved using methods like dynamic error budgeting, particularly when application-specific disturbances and noise profiles are known. Additionally, the observed trade-off in process sensitivity and sensitivity reduction at the parasitic resonance frequency, resulting in increased sensitivity at lower frequencies, highlights the necessity for careful tuning of the active damping controller. This tuning should be guided by the specific disturbance and noise rejection requirements relevant to the application. Future research could investigate the broader application of this strategy across various systems, potentially enhancing performance and robustness in diverse applications.

APPENDIX A

The conditions for which the inner closed damping loop is stable can be derived using the Routh-Hurwitz criterion. Given the higher-order non-collocated mode in Equation (5), the HP-PPF controller in Equation (7) and the closed-loop architecture given in Figure 15 with positive or negative feedback, the

following characteristic equation can be derived:

$$1 \pm G_p(s)C_{d-HPF}(s) = \dots$$

$$1 \pm \frac{\omega_2^4}{s^2(s^2 + 2\zeta_2\omega_2s + \omega_2^2)} \frac{g_n s^2}{s^2 + 2\zeta_c\omega_2s + \omega_2^2} = 0$$

$$s^4 + 2\zeta_c\omega_2s^3 + \omega_2^2s^2 + 2\zeta_2\omega_2s^3 + 4\zeta_2\zeta_c\omega_2^2s^2 + 2\zeta_2\omega_2^3s + \dots$$

$$\omega_2^2s^2 + 2\zeta_c\omega_2^3s + \omega_2^4 \pm g_n\omega_2^4 = 0$$

$$s^4 + (2\zeta_c\omega_2 + 2\zeta_2\omega_2)s^3 + (2\omega_2^2 + 4\zeta_2\zeta_c\omega_2^2)s^2 + \dots$$

$$(2\zeta_2\omega_2^3 + 2\zeta_c\omega_2^3)s + (\omega_2^4 \pm g_n\omega_2^4) = 0$$

In a similar way, the characteristic equation can be derived when a second-order low-pass filter is used for active damping of the higher-order non-collocated mode. The second-order LPF active damping controller, as used in PPF, is given by:

$$C_{d-LPF} = \frac{g_n\omega_2^2}{s^2 + 2\zeta_c\omega_2s + \omega_2^2}$$

The resulting closed damping loop characteristic equation is given by:

$$1 \pm G_p(s)C_{d-LPF}(s) = \dots$$

$$1 \pm \frac{\omega_n^2}{s^2(s^2 + 2\zeta_2\omega_2s + \omega_2^2)} \frac{g_n\omega_2^2}{s^2 + 2\zeta_c\omega_2s + \omega_2^2} = 0$$

$$s^6 + 2\zeta_c\omega_2s^5 + \omega_2^2s^4 + 2\zeta_2\omega_2s^5 + 4\zeta_2\zeta_c\omega_2^2s^4 + \dots$$

$$2\zeta_2\omega_2^3s^3 + \omega_2^2s^4 + 2\zeta_c\omega_2^3s^3 + \omega_2^4s^2 \pm g_n\omega_2^4 = 0$$

$$s^6 + 2\omega_2(\zeta_c + \zeta_2)s^5 + 2\omega_2^2(1 + 2\zeta_c\zeta_2)s^4 + \dots$$

$$2\omega_2^3(\zeta_c + \zeta_2)s^3 + \omega_2^4 + 0 \cdot s \pm g_n\omega_2^4 = 0$$

The coefficients of both the characteristic equations are summarized in Table I. To ensure stability, it is not enough to meet the necessary condition alone; the sufficient condition of the Routh-Hurwitz criterion must also be satisfied. This sufficient condition is analyzed using the Routh array, which is constructed as follows:

$$\begin{array}{c|cccccc} s^n & a_n & a_{n-2} & a_{n-4} & \dots & \dots \\ s^{n-1} & a_{n-1} & a_{n-3} & a_{n-5} & \dots & \dots \\ s^{n-2} & b_1 & b_2 & b_3 & \dots & \dots \\ s^{n-3} & c_1 & c_2 & c_3 & \dots & \dots \\ \vdots & \vdots & \vdots & \vdots & \ddots & \vdots \\ 0 & 0 & 0 & 0 & \dots & 0 \end{array}$$

Where b_1, b_2, b_3, \dots and c_1, c_2, c_3, \dots are computed as:

$$b_i = \frac{a_{n-1} \times a_{n-2i} - a_n \times a_{n-(2i+1)}}{a_{n-1}}$$

$$c_i = \frac{b_1 \times a_{n-(2i+1)} - a_{n-1} \times b_{i+1}}{b_1}$$

The system is stable if and only if all elements in the first column of the Routh array are of the same sign. The Routh array for the second-order high-pass filter in a negative feedback loop is given by:

$$\begin{array}{c|ccc} s^4 & 1 & 2\omega_2^2(1 + 2\zeta_c\zeta_2) & \omega_2^4(g_n + 1) \\ s^3 & 2\omega_2(\zeta_2 + \zeta_c) & 2\omega_2^3(\zeta_2 + \zeta_c) & 0 \\ s^2 & \omega_2^2(4\zeta_2\zeta_c + 1) & \omega_2^4(g_n + 1) & 0 \\ s^1 & -\frac{2\omega_2^3(g_n - 4\zeta_2\zeta_c)(\zeta_2 + \zeta_c)}{4\zeta_2\zeta_c + 1} & 0 & 0 \\ s^0 & \omega_2^4(g_n + 1) & 0 & 0 \end{array}$$

The Routh array for the second-order high-pass filter in a positive feedback loop is given by:

$$\begin{array}{c|ccc} s^4 & 1 & 2\omega_2^2(1 + 2\zeta_c\zeta_2) & \omega_2^4(1 - g_n) \\ s^3 & 2\omega_2(\zeta_2 + \zeta_c) & 2\omega_2^3(\zeta_2 + \zeta_c) & 0 \\ s^2 & \omega_2^2(4\zeta_2\zeta_c + 1) & \omega_2^4(1 - g_n) & 0 \\ s^1 & \frac{2\omega_2^3(g_n + 4\zeta_2\zeta_c)(\zeta_2 + \zeta_c)}{4\zeta_2\zeta_c + 1} & 0 & 0 \\ s^0 & \omega_2^4(1 - g_n) & 0 & 0 \end{array}$$

The coefficients of the first column are summarized in Table II.

APPENDIX B

The magnitude of the higher-order non-collocated mode, from Equation (5), at the resonance frequency is given by:

$$|G_p(i\omega_2)| = \left| \frac{\omega_2^4}{-\omega_2^2(-\omega_2^2 + 2\zeta_2\omega_2^2i + \omega_2^2)} \right| = \frac{1}{2\zeta_2}$$

The magnitude of the closed damping loop response, given in Equation (8), at the resonance frequency, can be calculated in similar fashion as:

$$|CL_d(i\omega_2)| = \frac{2\zeta_c}{g + 4\zeta_c\zeta_2} = \frac{1}{2\left(\frac{g_n}{4\zeta_c} + \zeta_2\right)},$$

From these expressions, it can be derived that the damping ratio of the closed damping loop can be described as:

$$\zeta_{CL_d} = \zeta_2 + \frac{g_n}{4\zeta_c},$$

showing an increase of the damping ratio when $g_n > 0$ and $\zeta_c > 0$.

APPENDIX C

The generalized transfer function of a two-degree-of-freedom non-collocated system is given in Equation (3) and the HP-PPF damping controller is given in Equation (7). The inner closed damping loop transfer function is given by Equation (8). This results in the following closed-loop characteristic equation:

$$(s^2 + 2\zeta_1\omega_1s + \omega_1^2)(s^2 + 2\zeta_2\omega_2s + \omega_2^2)(s^2 + 2\zeta_c\omega_2s + \omega_2^2) - \omega_1^2\omega_2^2g_n s^2 = 0$$

The active damping controller is targeted at the higher-order resonance frequency, such that:

$$\omega_2 = n \cdot \omega_1 \quad \omega_c = \omega_2 = n \cdot \omega_1$$

Which simplifies the characteristic equation to the following:

$$\begin{aligned} & s^6 + [2\omega_1(\zeta_1 + \zeta_2 n + \zeta_c n)] s^5 + \dots \\ & [\omega_1^2(1 + 2n^2 + 4\zeta_1\zeta_2 n + 4\zeta_1\zeta_c n + 4\zeta_2\zeta_c n^2)] s^4 + \dots \\ & [2n\omega_1^3(2\zeta_1 n + \zeta_2 + 2\zeta_c n^2 + 4\zeta_1\zeta_2\zeta_c n + \zeta_2 n^2)] s^3 + \dots \\ & [n^2\omega_1^4(2 + 4\zeta_1\zeta_c n + 4\zeta_2\zeta_c + n^2 + 4\zeta_1\zeta_2 n) - g_n n^2\omega_1^4] s^2 + \dots \\ & [2n^3\omega_1^5(\zeta_c + \zeta_1 n + \zeta_2)] s + [n^4\omega_1^6] = 0 \end{aligned}$$

This results in the following coefficients of the characteristic equation defined in general form in Equation (6):

$$\begin{aligned} a_6 &= 1 \\ a_5 &= 2\omega_1(\zeta_1 + n\zeta_2 + n\zeta_c) \\ a_4 &= \omega_1^2(2n^2 + 4n^2\zeta_2\zeta_c + 4n\zeta_1\zeta_2 + 4n\zeta_1\zeta_c + 1) \\ a_3 &= 2n\omega_1^3(\zeta_2 + \zeta_c + 2n\zeta_1 + n^2\zeta_2 + n^2\zeta_c + 4n\zeta_1\zeta_2\zeta_c) \\ a_2 &= n^2\omega_1^4(4\zeta_2\zeta_c - g_n + n^2 + 4n\zeta_1\zeta_2 + 4n\zeta_1\zeta_c + 2) \\ a_1 &= 2n^3\omega_1^5(\zeta_2 + \zeta_c + n\zeta_1) \\ a_0 &= n^4\omega_1^6 \end{aligned}$$

According to the Routh-Hurwitz theorem all these coefficients must be of positive sign. Due to the positive nature of the parameters only the a_2 coefficient can be negative. From this the following stability condition arises:

$$0 < g_n < 4\zeta_2\zeta_c + n^2 + 4n\zeta_1\zeta_2 + 4n\zeta_1\zeta_c + 2 \approx n^2 + 2$$

In Equation (13) this condition is denoted with factor k , relating it to the relative modal gains of the rigid-body and parasitic mode. The controller in Equation (14) incorporates this factor k , which results in the following characteristic equation for the inner closed damping loop:

$$\begin{aligned} & s^6 + [2\omega_1(\zeta_1 + \zeta_2 n + \zeta_c n)] s^5 + \dots \\ & [\omega_1^2(1 + 2n^2 + 4\zeta_1\zeta_2 n + 4\zeta_1\zeta_c n + 4\zeta_2\zeta_c n^2)] s^4 + \dots \\ & [2n\omega_1^3(2\zeta_1 n + \zeta_2 + 2\zeta_c n^2 + 4\zeta_1\zeta_2\zeta_c n + \zeta_2 n^2)] s^3 + \dots \\ & [n^2\omega_1^4 k - k \cdot g_n n^2\omega_1^4] s^2 + \dots \\ & [2n^3\omega_1^5(\zeta_c + \zeta_1 n + \zeta_2)] s + [n^4\omega_1^6] = 0 \end{aligned}$$

This results in the following coefficients of the characteristic equation defined in general form in Equation (6):

$$\begin{aligned} a_6 &= 1 \\ a_5 &= 2\omega_1(\zeta_1 + n\zeta_2 + n\zeta_c) \\ a_4 &= \omega_1^2(2n^2 + 4n^2\zeta_2\zeta_c + 4n\zeta_1\zeta_2 + 4n\zeta_1\zeta_c + 1) \\ a_3 &= 2n\omega_1^3(\zeta_2 + \zeta_c + 2n\zeta_1 + n^2\zeta_2 + n^2\zeta_c + 4n\zeta_1\zeta_2\zeta_c) \\ a_2 &= n^2\omega_1^4(k - k \cdot g_n) \\ a_1 &= 2n^3\omega_1^5(\zeta_2 + \zeta_c + n\zeta_1) \\ a_0 &= n^4\omega_1^6 \end{aligned}$$

From this the following stability condition arises:

$$0 < g_k < 1 \quad (32)$$

APPENDIX D

Appendix B evidenced the magnitude reduction of the inner closed damping loop at resonance frequency, given by:

$$|CL_d(i\omega_2)| = \frac{1}{2\left(\frac{g_n}{4\zeta_c} + \zeta_2\right)}$$

When a second-order low-pass filter (LPF) is incorporated into the active damping controller for noise attenuation, the active damping controller is represented by Equation (16), with $m = 2$, $\omega_{LPF} = \alpha \cdot \omega_c$, neglecting the damping ratio of the LPF for mathematical simplicity. The magnitude of the closed damping loop response at the resonance frequency, considering only the higher-order mode as defined in Equation (5), can then be calculated as:

$$|CL_{d-BPF}(i\omega_2)| = \frac{2\zeta_c |\alpha^2 + 1|}{|a^2 g_n - 4\zeta_c \zeta_2 + 4\alpha^2 \zeta_c \zeta_2|}$$

This equation clearly illustrates the dependence of the effective damping on the width of the band-pass filter, denoted by α . When assuming $\alpha \gg 1$ the equation simplifies to:

$$|CL_{d-BPF}(i\omega_2)| = \frac{2\zeta_c |\alpha^2|}{|\alpha^2 g_n + 4\alpha^2 \zeta_c \zeta_2|} = \frac{1}{2\left(\frac{g_n}{4\zeta_c} + \zeta_2\right)}$$

This indicates that when the low-pass filter is sufficiently distant from the high-pass filter, the active damping remains unaffected. Conversely, if the LPF is positioned too close to the HPF, the magnitude reduction is influenced.

APPENDIX E

When the notch filter is tuned to achieve a level of resonance attenuation in the open-loop response comparable to that of the active damping controller, such that Equation (19) is satisfied, the respective process sensitivity functions are described by Equations (20) and (18). Based on this, the ratio of the two process sensitivities can be calculated as follows:

$$\begin{aligned}
\left| \frac{PS_{ADC}}{PS_N} \right|_{\omega=\omega_2} &= \left| \frac{G_d}{1+G_d C_t} \right| / \left| \frac{G}{1+G_d C_t} \right| \\
&= \left| \frac{G_d}{1+G_d C_t} \right| \cdot \left| \frac{1+G_d C_t}{G} \right| \\
&= \frac{|G_d|}{|G|} \approx \frac{|G \cdot N|}{|G|} = |N|_{\omega=\omega_2} \\
|N|_{\omega=\omega_2} = |N(i\omega_2)| &= \left| \frac{-\omega_2^2 + \frac{2\zeta_N \omega_2^2 i}{Q} + \omega_2^2}{-\omega_2^2 + 2\zeta_N \omega_2^2 i + \omega_2^2} \right| = \frac{1}{Q} < 1
\end{aligned}$$

Note that this expression holds only when Equation (19) is satisfied and both architectures utilize the same tracking controller (C_t) given in Equation (11) and tuned following the rule-of-thumb in Equation (12). It applies specifically to the process sensitivity ratio at the location of the higher-order parasitic resonance mode.

REFERENCES

- [1] Yin Zhang, Haisheng Zhao, and Lijun Zuo. “Contact dynamics of tapping mode atomic force microscopy”. In: *Journal of sound and vibration* 331.23 (2012), pp. 5141–5152.
- [2] Fujun Wang et al. “Design of a piezoelectric-actuated microgripper with a three-stage flexure-based amplification”. In: *IEEE/ASME Transactions on Mechatronics* 20.5 (2014), pp. 2205–2213.
- [3] Sebastian Polit and Jingyan Dong. “Development of a high-bandwidth XY nanopositioning stage for high-rate micro-/nanomanufacturing”. In: *IEEE/ASME Transactions on mechatronics* 16.4 (2010), pp. 724–733.
- [4] Allen J Bronowicki, Nandu S Abhyankar, and Steven F Griffin. “Active vibration control of large optical space structures”. In: *Smart materials and structures* 8.6 (1999), p. 740.
- [5] Yingxiang Liu, Jie Deng, and Qi Su. “Review on multi-degree-of-freedom piezoelectric motion stage”. In: *IEEE Access* 6 (2018), pp. 59986–60004.
- [6] Arnfinn A Eielsen et al. “Damping and tracking control schemes for nanopositioning”. In: *IEEE/ASME Transactions on Mechatronics* 19.2 (2013), pp. 432–444.
- [7] Jan Holterman. “Vibration control of high-precision machines with active structural elements”. In: (2002).
- [8] André Preumont. *Vibration control of active structures: an introduction*. Vol. 246. Springer, 2018.
- [9] Santosh Devasia, Evangelos Eleftheriou, and SO Reza Moheimani. “A survey of control issues in nanopositioning”. In: *IEEE Transactions on Control Systems Technology* 15.5 (2007), pp. 802–823.
- [10] Georg Schitter, Philipp J Thurner, and Paul K Hansma. “Design and input-shaping control of a novel scanner for high-speed atomic force microscopy”. In: *Mechatronics* 18.5-6 (2008), pp. 282–288.
- [11] Jeffrey A Butterworth, Lucy Y Pao, and Daniel Y Abramovitch. “Analysis and comparison of three discrete-time feedforward model-inverse control techniques for nonminimum-phase systems”. In: *Mechatronics* 22.5 (2012), pp. 577–587.
- [12] Makoto Iwasaki, Kenta Seki, and Yoshihiro Maeda. “High-precision motion control techniques: A promising approach to improving motion performance”. In: *IEEE Industrial Electronics Magazine* 6.1 (2012), pp. 32–40.
- [13] Guo-Ying Gu and Li-Min Zhu. “Motion control of piezoceramic actuators with creep, hysteresis and vibration compensation”. In: *Sensors and Actuators A: Physical* 197 (2013), pp. 76–87.
- [14] Yidan Tao et al. “High-bandwidth tracking control of piezoactuated nanopositioning stages via active modal control”. In: *IEEE Transactions on Automation Science and Engineering* 19.4 (2021), pp. 2998–3006.
- [15] A.M. Natu, M.B. Kaczmarek, and S.H. HosseinNia. “Overactuation for Active Damping in Compliant Positioning Stage using Piezoelectric Transducers”. In: *IFAC-PapersOnLine* 58.7 (2024). 4th IFAC Conference on Advances in Proportional-Integral-Derivate Control PID 2024, pp. 269–274. ISSN: 2405-8963. DOI: <https://doi.org/10.1016/j.ifacol.2024.08.073>. URL: <https://www.sciencedirect.com/science/article/pii/S2405896324007912>.
- [16] Marcin B Kaczmarek and Hassan HosseinNia. “Fractional-Order Negative Position Feedback for Vibration Attenuation”. In: *Fractal and Fractional* 7.3 (2023), p. 222.
- [17] Mark J Balas. “Direct velocity feedback control of large space structures”. In: *Journal of guidance and control* 2.3 (1979), pp. 252–253.
- [18] Sumeet S Aphale, Andrew J Fleming, and SO Reza Moheimani. “Integral resonant control of collocated smart structures”. In: *Smart materials and structures* 16.2 (2007), p. 439.
- [19] Andrew J Fleming. “Nanopositioning system with force feedback for high-performance tracking and vibration control”. In: *IEEE/Asme Transactions on Mechatronics* 15.3 (2009), pp. 433–447.
- [20] SO Reza Moheimani and Benjamin JG Vautier. “Resonant control of structural vibration using charge-driven piezoelectric actuators”. In: *IEEE Transactions on control systems technology* 13.6 (2005), pp. 1021–1035.
- [21] CJ Goh and TK Caughey. “On the stability problem caused by finite actuator dynamics in the collocated control of large space structures”. In: *International Journal of Control* 41.3 (1985), pp. 787–802.
- [22] Bharath Bhikkaji et al. “High-performance control of piezoelectric tube scanners”. In: *IEEE Transactions on Control Systems Technology* 15.5 (2007), pp. 853–866.
- [23] Linlin Li et al. “Positive acceleration, velocity and position feedback based damping control approach for piezo-actuated nanopositioning stages”. In: *Mechatronics* 47 (2017), pp. 97–104.

- [24] Jeffrey Dosch, Donald Leo, and Daniel Inman. “Modeling and control for vibration suppression of a flexible active structure”. In: *Journal of Guidance, Control, and Dynamics* 18.2 (1995), pp. 340–346.
- [25] Sang-Myeong Kim, Semyung Wang, and Michael J Brennan. “Comparison of negative and positive position feedback control of a flexible structure”. In: *Smart Materials and Structures* 20.1 (2010), p. 015011.
- [26] Xiangyuan Wang et al. “Simultaneous damping and tracking control of a normal-stressed electromagnetic actuated nano-positioning stage”. In: *Sensors and Actuators A: Physical* 338 (2022), p. 113467.
- [27] Sajal K Das, Hemanshu R Pota, and Ian R Petersen. “Damping controller design for nanopositioners: A mixed passivity, negative-imaginary, and small-gain approach”. In: *IEEE/ASME Transactions on Mechatronics* 20.1 (2014), pp. 416–426.
- [28] Fazhi Song et al. “Motion Control of Wafer Scanners in Lithography Systems: From Setpoint Generation to Multi-Stage Coordination”. In: *IEEE Transactions on Instrumentation and Measurement* (2024), pp. 1–1. DOI: 10.1109/TIM.2024.3413202.
- [29] R Munnig Schmidt, Georg Schitter, and Adrian Rankers. *The design of high performance mechatronics: high-Tech functionality by multidisciplinary system integration*. Ios Press, 2020.
- [30] Zi-Hui Zhu et al. “Triaxial fast tool servo using hybrid electromagnetic–piezoelectric actuation for diamond turning”. In: *IEEE Transactions on Industrial Electronics* 69.2 (2021), pp. 1728–1738.
- [31] S Hassan HosseinNia and Niranjana Saikumar. “Fractional-order precision motion control for mechatronic applications”. In: *Handbook of Fractional Calculus with Applications* 6 (2019), pp. 339–356.
- [32] Jorge Nocedal and Stephen J Wright. *Numerical optimization*. Springer, 1999.
- [33] Wouter Monkhorst. “Dynamic error budgeting: A design approach”. In: (2004).
- [34] Habib Habibullah, Hemanshu R Pota, and IR Petersen. “A robust control approach for high-speed nanopositioning applications”. In: *Sensors and Actuators A: Physical* 292 (2019), pp. 137–148.
- [35] Chun-Xia Li et al. “Damping control of piezo-actuated nanopositioning stages with recursive delayed position feedback”. In: *IEEE/ASME Transactions on Mechatronics* 22.2 (2016), pp. 855–864.

4

Results & Discussion

This chapter offers an in-depth discussion of some of the results highlighted in the previous chapter, which outlined the key findings of the research. It examines the implications of these results more closely, providing additional perspectives and insights beyond the initial analysis. By reflecting on the findings within a broader context, the chapter aims to deepen the understanding of their significance, identify potential limitations, and propose future directions for research.

4.1. Stability of Inner HP-PPF Active Damping Loop

As demonstrated in the previous chapter, while the active damping controller is designed to target the first higher-order resonance mode, it is essential to account for the dynamics of the rigid-body mode at lower frequencies. When these two modes are relatively close, the control effort of the active damping controller can spill over to the rigid-body mode, potentially destabilizing the poles associated with it. The stability of the inner damping loop ultimately depends on the spacing between the rigid-body mode and the higher-order non-collocated mode, denoted by n , as well as the two control parameters of the active damping controller: g_k and ζ_c . In turn, the stability of the outer closed-loop is also influenced by the parameters of the tracking controller used.

The inner closed damping loop responses and Nyquist plots in Figure 4.1 show that the same active damping controller, with the same control parameters, can lead to an unstable inner loop depending on the mode spacing.

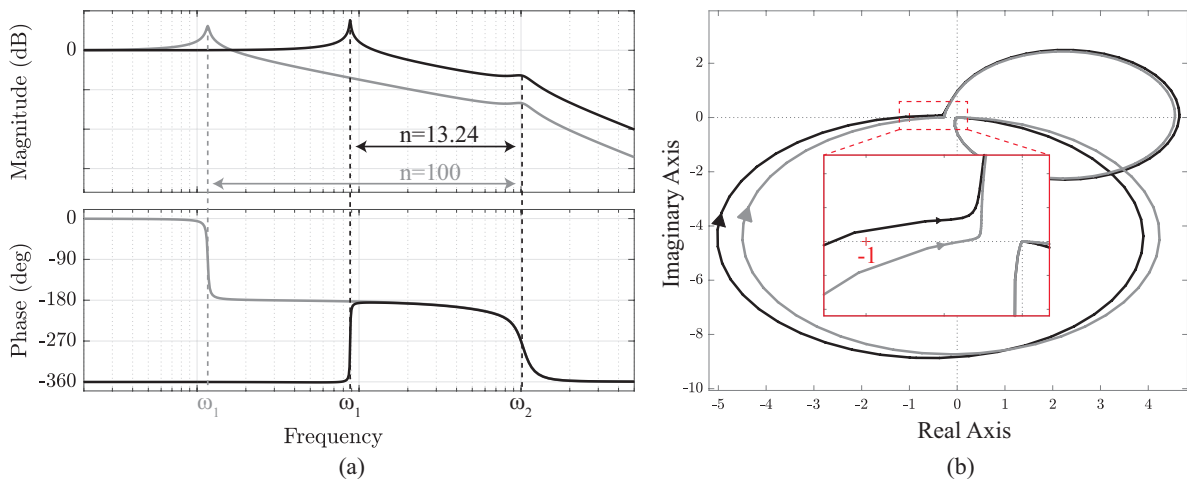


Figure 4.1: (a) Inner closed damping loop for $n = 13.24$ (black) as in experimental setup and $n = 100$ (grey) with same active damping control parameters, (b) Nyquist plot encircles -1 for $n = 13.24$ (black) and does not encircle -1 for $n = 100$ (grey), indicating unstable and stable closed-loops, respectively

As shown in the previous chapter with numerical and experimental results, the tracking controller in the outer loop can be tuned to achieve a stable closed-loop system. The commonly used PID controller adds 45° of phase at the crossover, which can stabilize the outer closed-loop, as observed in the open-loop response in 4.2.a. The PID controller effectively shifts the Nyquist plot, preventing the encirclement of the -1 point, as shown in Figure 4.2.b.

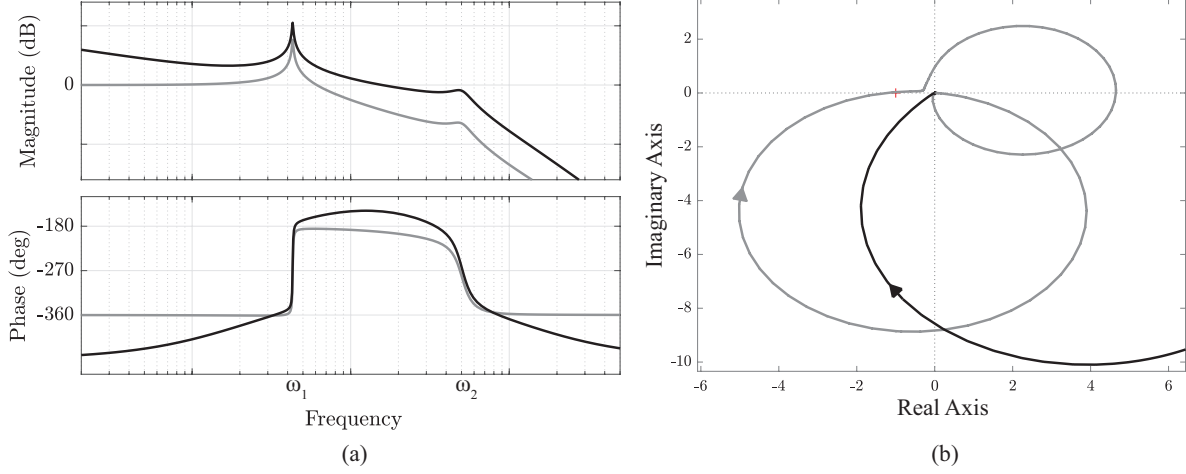


Figure 4.2: (a) Inner closed damping loop for $n = 13.24$ (grey) and tracking control open-loop $C_t(s) \cdot CL_d(s)$ (black), (b) Nyquist plot encircles -1 for inner damping loop (grey) and does not encircle -1 for outer loop when PID tracking control is added (black), indicating unstable and stable closed-loops, respectively

As derived, the Routh-Hurwitz criterion yields the following necessary condition for stability of the inner closed damping loop:

$$0 < g < 4\zeta_2\zeta_c + n^2 + 4n\zeta_1\zeta_2 + 4n\zeta_1\zeta_c + 2 = k \quad (4.1)$$

which simplifies to $0 < g_k < 1$ when the factor k is incorporated into the feedback gain of the active damping controller. This condition suggests that the stability of the inner damping loop should depend only on the active damping feedback gain g_k . However, as demonstrated in Figure 4.1, the inner closed-loop can still become unstable even when $0 < g_k < 1$. According to the Routh-Hurwitz criterion, this is a necessary condition for stability, meaning that satisfying the condition does not guarantee stability. To assess stability, the Routh array must be evaluated, where the system remains stable if and only if all elements in the first column are positive. However, due to the high order of the characteristic equation, the coefficients in the Routh array become large and complex analytical expressions. Consequently, a sufficient analytical condition for the stability of the inner damping loop using HP-PPF for the non-collocated fourth-order dynamics has not yet been determined.

However, the stability of the outer closed-loop is ultimately what matters, as it has been shown that an unstable inner loop can be stabilized by the outer control loop. Figure 4.3 illustrates how the stability of the inner closed-loop depends on the control parameters g_k and ζ_c , and how incorporating a PID tracking controller expands the stable region within the damping control parameter design space.

The possibility of having an unstable inner damping loop that can be stabilized by the outer closed-loop underscores the advantage of simultaneous design of both controllers. When designed separately, a damping controller might be dismissed if it results in an unstable inner damping loop, even though the outer tracking controller could stabilize the system. This approach limits the potential design space for control parameters and may overlook configurations that could offer better overall performance.

In the previous chapter, this was demonstrated through an optimization process aimed at maximizing open-loop bandwidth. The optimal combination of active damping control parameters resulted in an unstable inner loop, which was subsequently stabilized by the tracking controller in the outer loop. This highlights the need for simultaneous design of both controllers, particularly when the objective is to optimize the overall system performance.

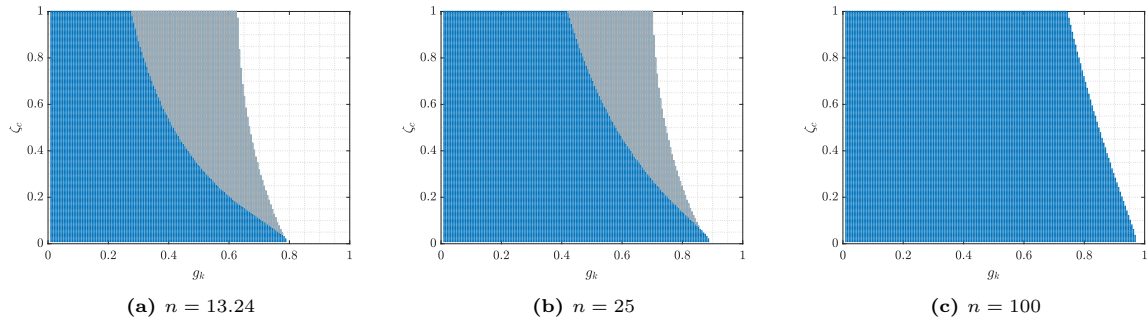


Figure 4.3: Stability regions as a function of g_k and ζ_c , indicating where both the inner damping loop and outer closed-loop are stable (blue), and the region where the inner damping loop is unstable but the outer closed-loop with the PID tracking controller becomes stable (grey). In (a) mode spacing $n = 13.24$ as in the experimental setup, in (b) the mode spacing $n = 25$ and in (c) mode spacing $n = 100$

4.1.1. Attenuating Feedback Noise using Band-Pass Filter

To prevent high-frequency noise from being fed back through the inner damping loop to the current amplifier and actuator, it is crucial to incorporate high-frequency roll-off in the active damping controller. This feedback of noise, if not properly addressed, can lead to several undesirable effects such as actuator saturation, interference with the system's intended dynamic response, and potential instability. High-frequency noise can also introduce additional stress on the amplifier, increasing power consumption and reducing overall system efficiency. To achieve this desired high-frequency roll-off, a low-pass filter is added after the second-order high-pass filter, effectively forming a band-pass filter. This configuration ensures that while the desired damping control frequencies are maintained, the high-frequency components, which are typically dominated by noise, are attenuated. Increasing the order of the low-pass filter enhances the high-frequency roll-off, and to maximize this effect, it is recommended to position the low-pass filter as close as possible to the high-pass filter.

However, the placement of the low-pass filter introduces a trade-off. While proximity to the high-pass filter improves noise attenuation at higher frequencies, it also introduces phase lag, which can negatively impact the phase of the high-pass filter. This, in turn, can degrade the damping performance of the active damping controller. Figure 4.4 illustrates this relationship, showing the effect of placing a second-order low-pass filter at different multiples of the second-order high-pass filter's cut-off frequency ($\omega_{LPF} = \alpha \cdot \omega_{HPF}$), resulting in varying band-pass widths. The figure demonstrates that when the low-pass filter is placed too close to the high-pass filter, the peak attenuation decreases, thereby reducing the overall damping performance. This highlights the importance of carefully balancing noise suppression and damping performance in the design of the active damping controller and additional low-pass filter.

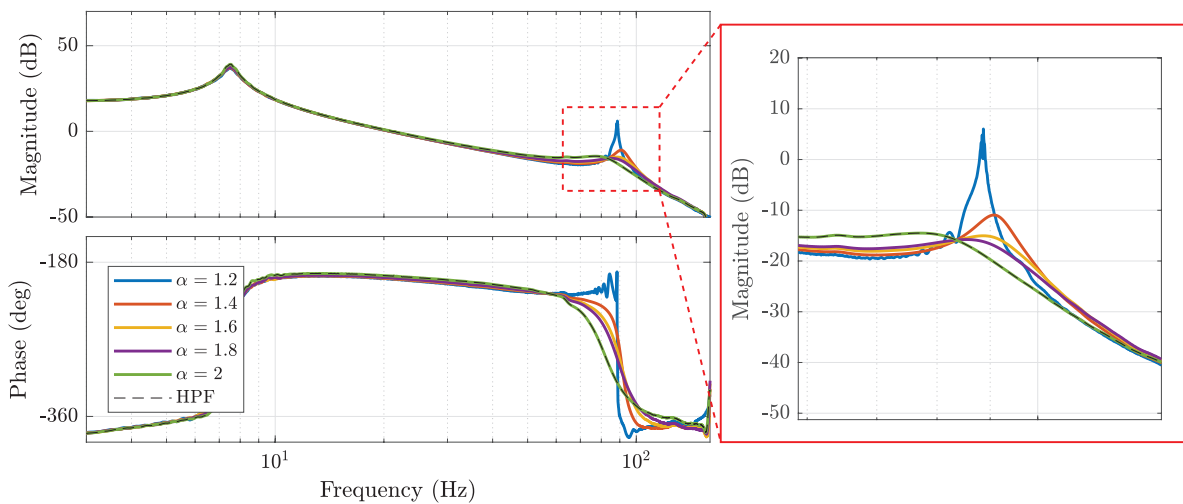


Figure 4.4: Experimentally identified inner closed damping loop for different band-pass filter widths α , consisting of a second-order high-pass filter and a second-order low-pass filter is at $\omega_{LPF} = \alpha \cdot \omega_{HPF}$

4.2. Closed-Loop Disturbance Rejection

One of the key limitations of using a notch filter to target higher-order modes is that the resonance peak remains in the closed-loop process sensitivity function. This means that even though the mode is attenuated in the complementary closed-loop response and open-loop response, allowing greater control bandwidths, it can still be excited by disturbances in the resonant frequency range, potentially inducing unwanted vibrations. In Figure 4.5 it can be observed that the active damping controller effectively attenuates the parasitic resonance in the process sensitivity function, addressing this limitation of the notch filter approach. The resonance peak is suppressed by approximately 13 dB, significantly improving the system's ability to reject process disturbances at this frequency, which in turn enhances the position accuracy of the end-effector platform.

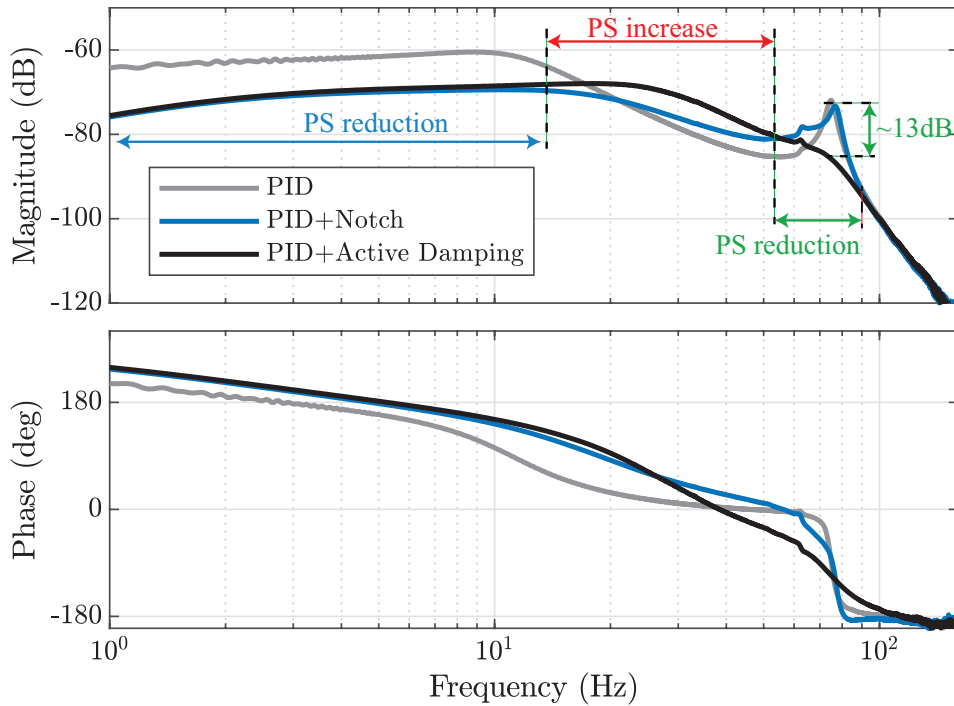


Figure 4.5: Experimentally identified closed-loop process sensitivity frequency responses for three comparison cases. The reduction achieved by the high-gain tracking controller is indicated in blue, while the reduction due to active damping is highlighted in green

The higher control bandwidth of the active damping control- and notch-based architectures, compared to that of the undamped control architecture, is a result of the increased gain of the PID controller tuned for these cases. This higher gain leads to a lower process sensitivity gain at frequencies below the control bandwidth, as illustrated in Figure 4.5. The frequency response indicates comparable disturbance rejection performance at low frequencies between the active damping control- and notch filter-based architecture.

However, between the first mode (6 Hz) and the parasitic mode (78 Hz), the active damping control architecture shows an increase in process sensitivity compared to the notch filter architecture. This rise in process sensitivity is attributed to spillover effects within the inner damping loop, which can be mitigated by reducing the gain g_k of the active damping controller, as illustrated in Figure 4.6.

This dual closed-loop process sensitivity response for varying feedback gains clearly highlights the trade-off between reducing process disturbances around the parasitic resonance and sacrificing disturbance rejection in the frequency range between the first two resonance modes. Specifically, as the feedback gain is increased to suppress the parasitic resonance, the sensitivity is effectively reduced in that targeted frequency region, improving system performance by attenuating vibrations and disturbances near the parasitic mode. However, this gain adjustment simultaneously leads to an increase in process sensitivity at intermediate frequencies, between the first and parasitic mode, which results in less effective disturbance rejection in this range.

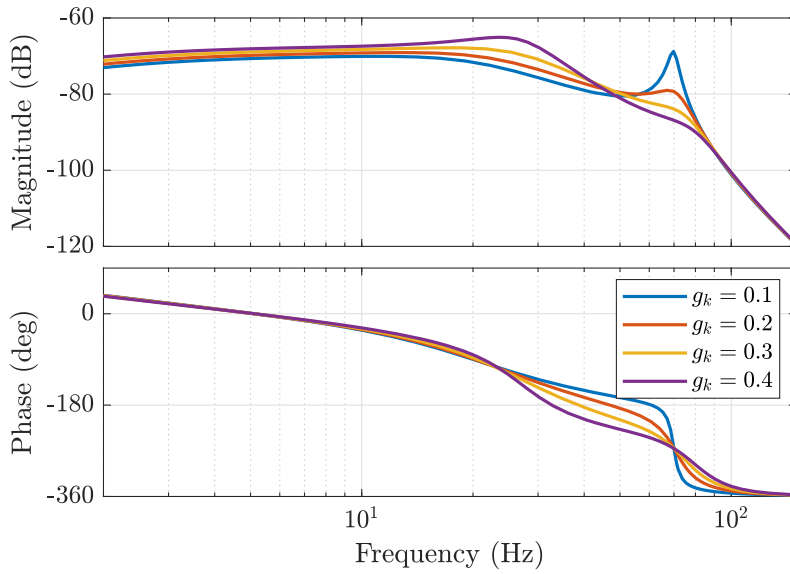


Figure 4.6: Dual closed-loop process sensitivity frequency response for varying active damping controller gain g_k

This trade-off becomes crucial when tuning the active damping controller, as the performance is highly application-specific. Depending on the operating environment and the nature of the disturbances, the control strategy must prioritize which frequency range to focus on for process sensitivity reduction. For instance, in applications where the dominant disturbances occur near the parasitic resonance, such as from cross-coupling effects in multi-degree-of-freedom systems, maximizing damping of this mode is critical for increasing accuracy and precision. On the other hand, if significant disturbances are present at lower frequencies, such as from environmental factors like floor vibrations or slow, low-frequency perturbations, increasing process sensitivity at those intermediate frequencies may compromise performance.

4.2.1. Case Study: Floor Vibration Disturbances

A common source of disturbances in positioning systems is floor vibrations. In the experimental setup, these vibrations are mitigated by a vibration isolation table. However, as a case study, the performance of the active damping control architecture is evaluated in terms of its ability to reject a floor disturbance profile, compared with the two other control architectures, using dynamic error budgeting.

For the setup presented in [129] and [130], the noise spectrum of floor vibrations was measured, with the corresponding Power Spectral Density (PSD) illustrated in Figure 4.7 [131]. While the experimental setup benefits from a vibration isolation platform to minimize disturbances, the PSD provides a representative example of floor vibration disturbances for systems that do not have such isolation. This case study highlights how the active damping controller must be tuned to manage process sensitivity in specific frequency ranges.

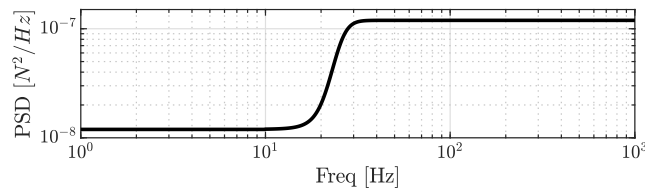


Figure 4.7: PSD of typical floor vibration profile [131]

The provided PSD of floor vibrations, which acts as a process disturbance to the system, can be utilized to perform dynamic error budgeting (DEB) using the measured process sensitivity functions for the three compared control architectures. The resulting PSD and Cumulative Power Spectrum (CPS) are illustrated in Figure A.11. It is evident that the control architecture with active damping results in a higher total error due to floor vibration disturbances compared to the notch filter architecture. This is mainly due to the increased gain in the process sensitivity between the first two resonance modes, where the floor vibrations are dominant. However, at the frequency of the higher-order parasitic mode (ω_2), the undamped and notch filter architectures display a sharp rise in error, which is absent with the implementation of active damping control. The improvement seen here is due to the suppression of the parasitic resonance in the active damping control's process sensitivity, something that the notch filter fails to achieve.

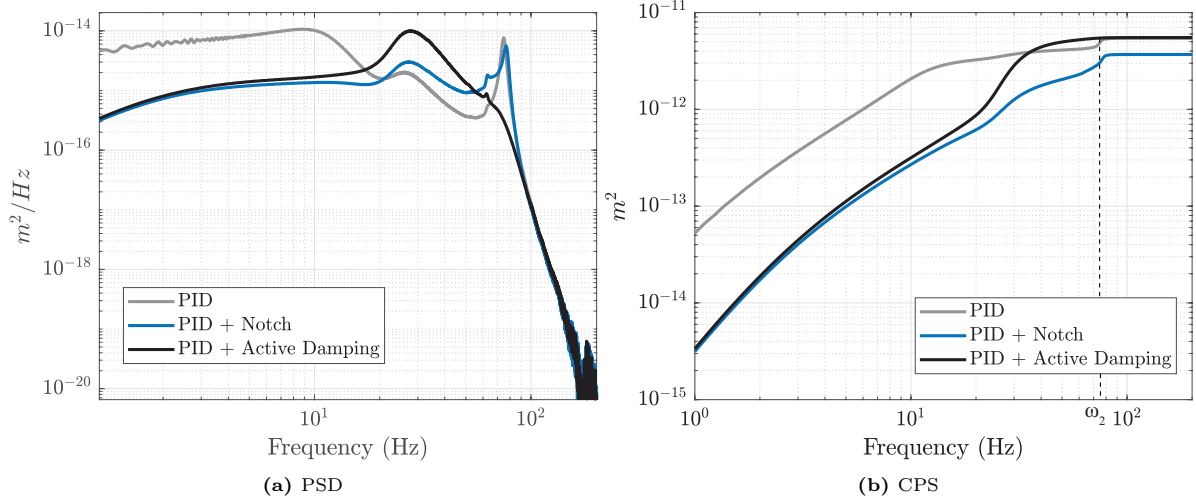


Figure 4.8: Dynamic error budgeting of floor disturbance profile for three comparison cases

As discussed in the previous chapter, cross-coupling effects can introduce disturbances around the frequency of the parasitic resonance. Figure 4.9 presents the dynamic error budgeting for a disturbance input that combines the floor vibration profile with a multisine signal designed to simulate cross-coupling disturbances at the parasitic resonance (ω_2), given by:

$$d(t) = d_{floor}(t) + A \sin(2\pi \cdot \omega_2 t) \quad (4.2)$$

In this scenario, the persistence of the resonance peak in the process sensitivity for the notch filter architecture becomes much more apparent. Both the notch filter and undamped architectures show a significant increase in error around the parasitic mode frequency, leading to a higher total error compared to the active damping architecture.

It is important to note that this disturbance signal is arbitrary, with no representative scaling between the combined disturbance components. It serves merely as an illustrative example to highlight how errors can increase around the parasitic resonance. The actual impact of such disturbances will vary depending on the specific magnitudes of the disturbance signals in a given application.

4.3. Real Error Contributions

In control system analysis, it is common to use the Complementary Sensitivity ($T(s)$), Process Sensitivity ($PS(s)$), and Sensitivity (S) functions to assess the impact of various inputs on the measured output y . However, the real focus should be on the errors related to the actual position x , rather than the measured position, as these errors directly affect system performance. Although the actual errors are not directly measurable, it is essential to numerically evaluate the sensitivity of the true feedback error, which is the difference between the reference signal r and the actual position x . In a standard

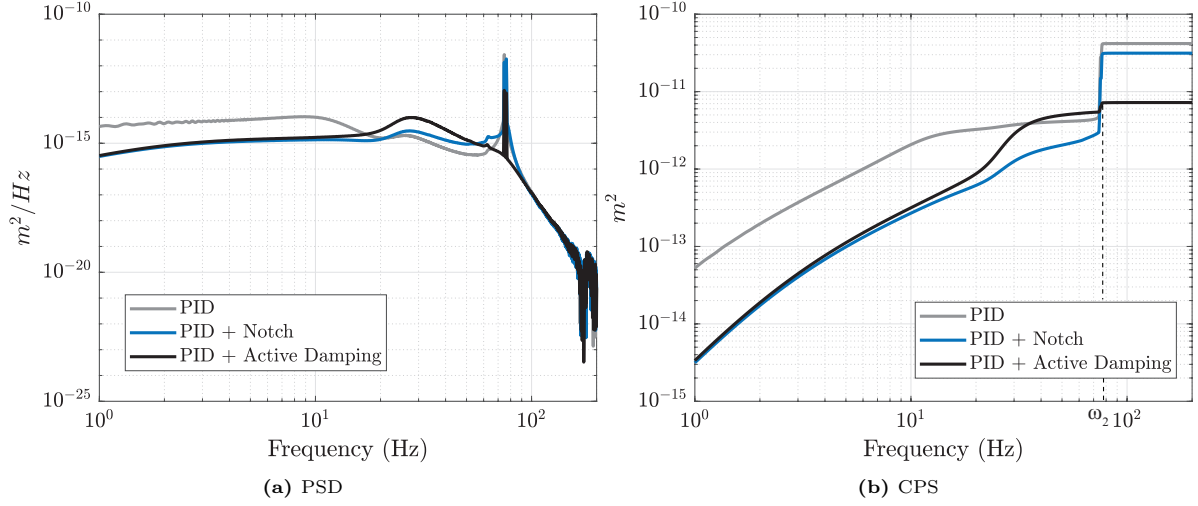


Figure 4.9: Dynamic error budgeting of floor disturbance profile combined with multiisine representing cross-coupling disturbance, for three comparison cases

feedback loop, the real error can be expressed as follows [33]:

$$e_{real}^2 = (r - x)^2 = \left(\frac{1}{1 + GC_t} r \right)^2 - \left(\frac{G}{1 + GC_t} d \right)^2 + \left(\frac{GC_t}{1 + GC_t} n \right)^2 \quad (4.3a)$$

$$e_{real} = r - x = \sqrt{(S(s)r)^2 + (PS(s)d)^2 + (T(s)n)^2} \quad (4.3b)$$

However, this formulation is no longer valid in a dual-loop control architecture that combines active damping control and motion control. The inner damping loop introduces additional error components that must be accounted for. The contribution of different input signals to the actual position x in a dual-loop system can be expressed as:

$$\frac{x}{r} = \frac{GC_t}{1 + G(C_t - C_d)} \quad \frac{x}{d} = \frac{G}{1 + G(C_t - C_d)} \quad \frac{x}{n} = \frac{G(C_d - C_t)}{1 + G(C_t - C_d)} \quad (4.4)$$

$$x = \frac{GC_t}{1 + G(C_t - C_d)} r + \frac{G}{1 + G(C_t - C_d)} d + \frac{G(C_d - C_t)}{1 + G(C_t - C_d)} n \quad (4.5)$$

Given these transfer functions, and assuming the inputs are uncorrelated, the real feedback error in the dual-loop architecture can be calculated as:

$$e_{real_{dual}} = r - x = r - \frac{GC_t}{1 + G(C_t - C_d)} r + \frac{G}{1 + G(C_t - C_d)} d + \frac{G(C_d - C_t)}{1 + G(C_t - C_d)} n \quad (4.6a)$$

$$e_{real_{dual}}^2 = (r - x)^2 = \left(\frac{(r - x)}{r} r \right)^2 + \left(\frac{(r - x)}{d} d \right)^2 + \left(\frac{(r - x)}{n} n \right)^2 \quad (4.6b)$$

$$= \left(r - \frac{GC_t}{1 + G(C_t - C_d)} r \right)^2 + \left(\frac{G}{1 + G(C_t - C_d)} d \right)^2 + \left(\frac{G(C_d - C_t)}{1 + G(C_t - C_d)} n \right)^2 \quad (4.6c)$$

$$= \left(\frac{1 - GC_d}{1 + G(C_t - C_d)} r \right)^2 + \left(\frac{G}{1 + G(C_t - C_d)} d \right)^2 + \left(\frac{G(C_d - C_t)}{1 + G(C_t - C_d)} n \right)^2 \quad (4.6d)$$

$$e_{real_{dual}} = r - x = \sqrt{\left(\frac{1 - GC_d}{1 + G(C_t - C_d)} r \right)^2 + \left(\frac{G}{1 + G(C_t - C_d)} d \right)^2 + \left(\frac{G(C_d - C_t)}{1 + G(C_t - C_d)} n \right)^2} \quad (4.6e)$$

Here, C_t denotes the tracking controller, and C_d represents the HP-PPF active damping controller. The transfer functions from Equation (4.6).e illustrate how each input signal contributes to the total

real error. Figure 4.10 presents these error contributions for the numerical control architectures used in the experimental setup, with (a) showing the error due to reference signals r , (b) due to process disturbances d , and (c) due to noise n .

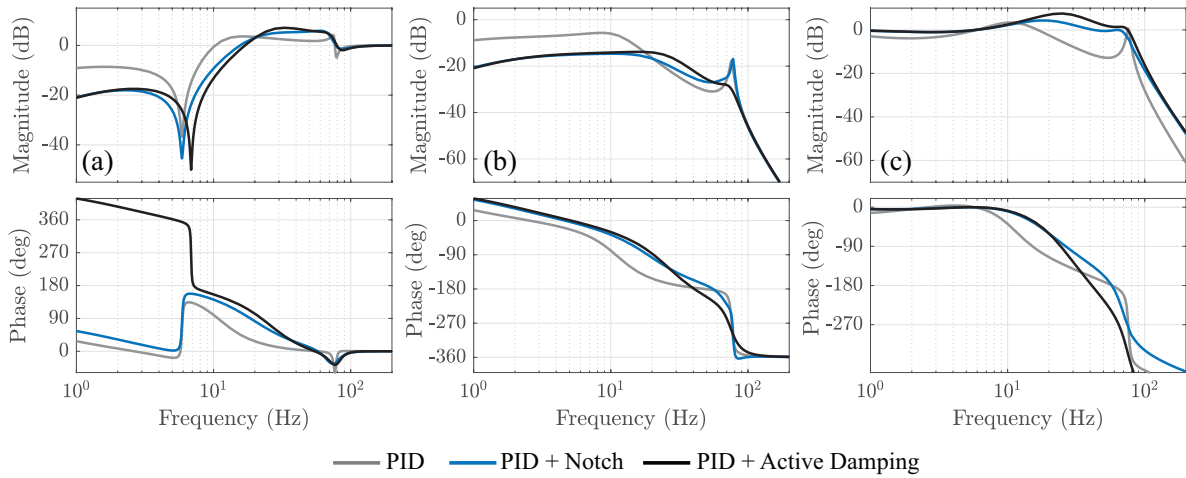


Figure 4.10: Real feedback error contributions related to (a) reference r , (b) process disturbance d , and (c) noise n for three comparison cases

The active damping controller clearly outperforms the notch filter in reducing errors caused by process disturbances around the parasitic resonance frequency, as shown by the process sensitivity function in both the single- and dual-loop control architectures. Both the notch filter and active damping architectures enable higher control bandwidths, reducing error contributions from reference signals and process disturbances at lower frequencies. However, this increased control bandwidth also amplifies the errors associated with noise, as illustrated in Figure 4.10.c.

Moreover, the reduction of errors at certain frequencies can lead to increased error contributions at other frequencies, due to the Bode waterbed effect. This phenomenon implies that while the active damping control architecture can significantly reduce errors in some frequency ranges compared to a notch filter-based solution, it may inadvertently increase real errors in other regions.

Overall, the performance of the active damping controller depends on the specific characteristics of the reference, disturbance, and noise signals present in a given application. Although it offers notable advantages in suppressing parasitic resonance and enhancing disturbance rejection in this region, these benefits must be weighed against potential increases of error in other frequency regions. This highlights the need for application-specific tuning to achieve optimal performance.

4.4. Exploration of Non-minimum Phase Filters

This chapter presents a preliminary exploration of using a non-minimum phase filter to stabilize the inner active damping loop. While initial results show promise, further research is required to refine this approach.

This research introduced the High-Pass Positive Position Feedback (HP-PPF) active damping controller, which uses positive feedback to provide active damping of higher-order non-collocated modes. However, a challenge arises when the rigid-body mode is not sufficiently separated from the target mode, as the active damping controller can destabilize the rigid-body mode if the modes are too close.

While it has been shown that this inner instability can be resolved through the tracking controller in the outer feedback loop, an alternative approach for achieving a stable inner damping loop may involve the use of selective positive feedback. Currently, the position signal in the inner damping loop is fed back across the entire frequency range, including the region around the rigid-body mode, even though positive feedback is only necessary for active damping of the higher-order non-collocated mode. By using a non-minimum phase (NMP) filter, it is possible to invert the feedback signal in a specific controllable frequency range, effectively applying a phase shift of -180° without affecting the magnitude.

In non-minimum phase systems, the phase shift may exceed the expected value based on the slope of

the magnitude in the Bode plot, resulting in more negative phase shifts than anticipated [33]. This behaviour, caused by right-half-plane zeros, often complicates control design [132]. However, in this application, the non-minimum phase characteristics can be exploited to achieve the desired feedback effect. The transfer function for a first-order non-minimum phase filter is defined as follows:

$$NMP(s) = \frac{p - s}{p + s} \quad (4.7)$$

At low frequencies, where $s \ll p$, the transfer function simplifies to $p/p = 1$. At high frequencies, $s \gg p$, the transfer function simplifies to $-s/s = -1$, effectively inverting the filter's phase. This selective phase reversal can be controlled by adjusting the parameter p , allowing precise tuning of the frequency range where the inversion occurs. The filter's magnitude remains $|1|$ across the entire frequency range, meaning it does not affect the magnitude of the control loop at any frequency. The frequency response of the non-minimum phase filter in Equation (4.7) is depicted in Figure 4.11.

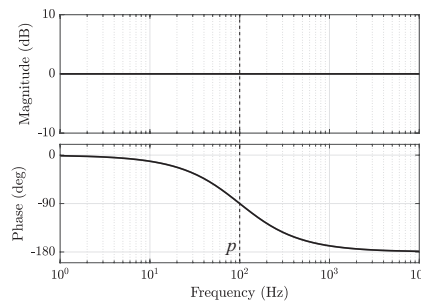


Figure 4.11: Non-minimum phase filter targeted at $p = 100$

This non-minimum phase (NMP) filter can be integrated into the active damping feedback loop, as shown in Figure 4.12. When applied to damp the higher-order non-collocated mode, where positive feedback is needed for stability, the filter's parameter p can be tuned to lie between the rigid-body mode and the higher-order parasitic mode. In doing so, the NMP filter effectively inverts the feedback signal (multiplies by -1) for frequencies above p , while maintaining the original phase for frequencies below p . Placed in a negative feedback loop, this setup provides positive feedback in the frequency range of the higher-order mode and negative feedback in the range of the rigid-body mode.

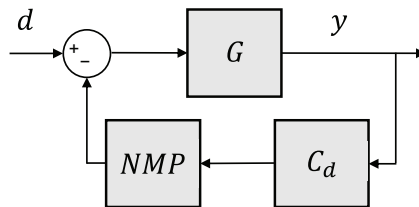


Figure 4.12: Active damping negative feedback loop with non-minimum phase filter (NMP)

Numerical simulations, based on control parameters from the experimental setup where inner loop instability was observed, show the potential of this approach. The NMP filter was tuned to lie between the first and second resonance modes, and the results are compared with the HP-PPF control architecture in Figure 4.13.

As can be observed in closed-loop response in Figure 4.13b, and the Nyquist plots in Figure 4.14, the implementation of the non-minimum phase filter along with negative feedback leads to a stable inner active damping feedback loop, which was previously unstable with the HP-PPF approach. Furthermore, the inner closed-loop response reveals that the non-minimum phase filter architecture introduces a slight phase lead between the two resonance modes. This phase lead can be advantageous for enhancing tracking control performance.

In Figure 4.15 a standard rule-of-thumb PID tracking controller is employed within the dual-loop control architecture to facilitate tracking control. The implementation of this configuration yields a

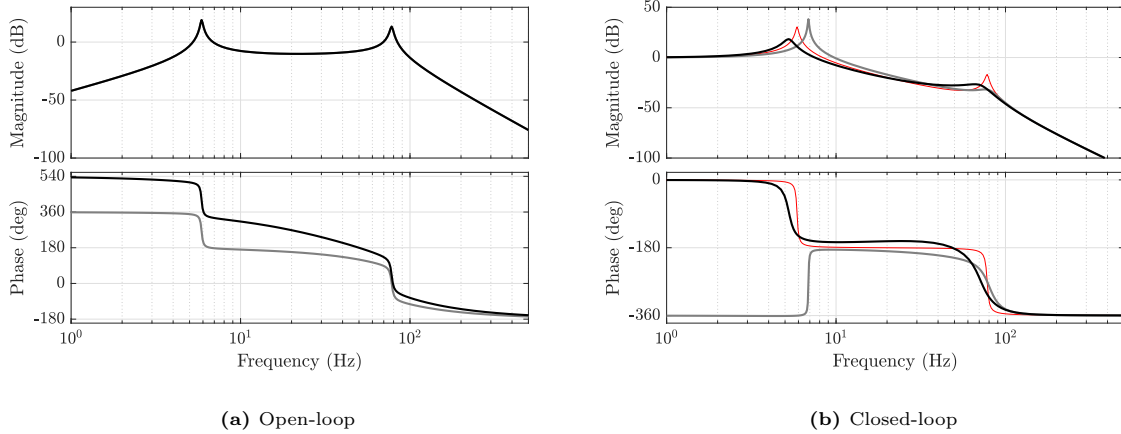


Figure 4.13: Active damping control of the higher-order non-located mode (red) using a second-order high-pass filter combined with a non-minimum phase (NMP) filter (black), compared to the HP-PPF control architecture (grey)

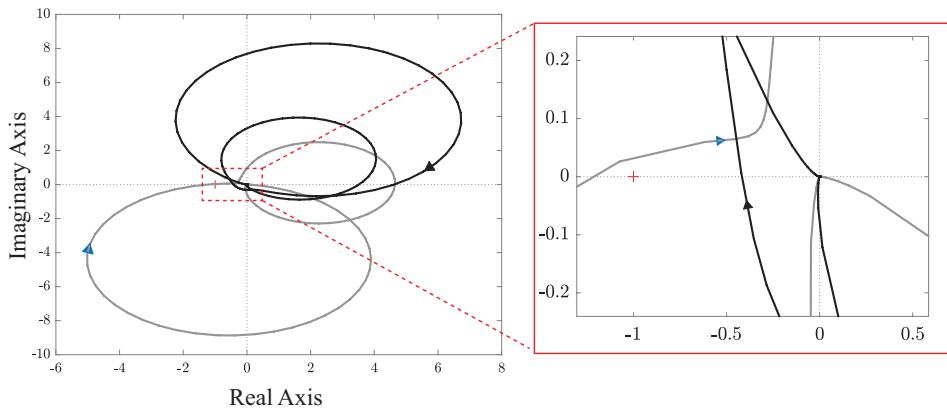


Figure 4.14: Nyquist of active damping using a second-order high-pass filter combined with a non-minimum phase (NMP) filter (black) showing stability, compared to the unstable HP-PPF control architecture (grey)

stable reference tracking response, showcasing the effectiveness of the control strategy. Importantly, it should be noted that neither of the control parameters has been optimized in this scenario, instead, this serves as a proof-of-concept. The primary aim is to illustrate the potential benefits of integrating a non-minimum phase filter into the inner active damping loop.

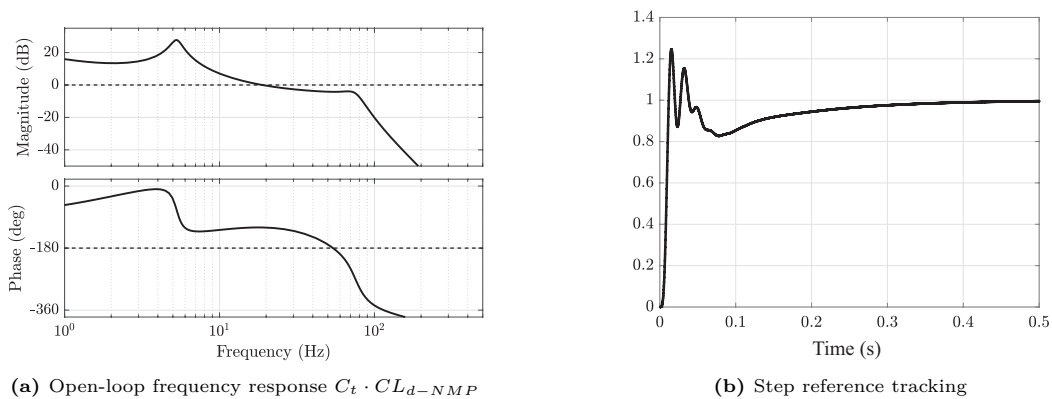


Figure 4.15: Dual-loop tracking control with non-minimum phase active damping control

5

Conclusions & Recommendations

5.1. Conclusions

In positioning systems, higher-order resonance modes can lead to undesired vibrations that reduce positioning accuracy. This research introduces a novel active damping control method designed specifically to suppress these higher-order resonance modes. The proposed method integrates a second-order high-pass filter within a positive feedback loop, referred to as High-Pass Positive Position Feedback (HP-PPF), aimed at mitigating the effects of higher-order parasitic resonance.

This study has explored the limitations of existing control techniques in addressing higher-order modes, particularly when the rigid-body dynamics interfere with the target mode. These limitations make direct application of traditional active damping control methods ineffective in certain configurations. The HP-PPF method, however, addresses this challenge by successfully enhancing damping of the higher-order mode.

In motion control applications, the proposed active damping method can be integrated into a dual-loop architecture with a tracking controller, both utilizing the same actuator and sensor. This eliminates the need for additional actuators and sensors for active damping, addressing the challenges associated with overactuation and modal decomposition techniques. In non-collocated dual-stage positioning systems the dominant higher-order parasitic resonance not only contributes to disturbance errors but also significantly restricts control bandwidth, highlighting the need for damping this mode. To experimentally validate the contributions and the underlying mathematical framework, this dual-loop architecture was implemented in a single-axis dual-stage compliant positioning system as a proof-of-concept setup.

Potential instability in the inner damping loop can arise when the rigid-body mode and the targeted higher-order mode are closely spaced. In such cases, the tracking controller can be tuned to provide the necessary phase at the open-loop crossover frequency, thereby stabilizing the outer loop and ensuring overall system stability. To address feedback of high-frequency noise in the inner damping loop, a second-order low-pass filter is applied after the HP-PPF controller, enhancing high-frequency roll-off. However, careful tuning of this low-pass filter is crucial, as it introduces a trade-off between noise attenuation and damping performance.

Simultaneous optimization of the HP-PPF active damping controller and the PID tracking controller to maximize open-loop bandwidth has shown improved disturbance rejection and noise suppression around the higher-order parasitic mode when compared to a traditional notch filter-based architecture. This results in enhanced rejection of disturbances, such as cross-coupling effects. However, reducing disturbance and noise sensitivity around the parasitic resonance frequency leads to increased sensitivity at lower frequencies, requiring careful tuning of the active damping controller based on specific disturbance and noise profiles relevant to the application.

A notable distinction between the HP-PPF and notch filter approaches lies in their methods of resonance peak attenuation. The HP-PPF method achieves attenuation through phase compensation, while notch filters use gain reduction. This phase-based attenuation makes the HP-PPF approach significantly more robust to model uncertainties, as experimentally proven, addressing one of the major limitations

of notch filters.

Since the higher-order resonance modes typically limit the control bandwidth in non-collocated dual-stage positioning systems, the implementation of the dual-loop HP-PPF architecture results in substantial bandwidth improvements. This enables faster and more accurate tracking of input references. The dual-loop system achieves similar control bandwidth and stability margins as notch filter-based architectures, with comparable performance in step and triangular wave reference tracking.

In conclusion, this research introduces a novel active damping control method designed to suppress higher-order resonance modes. The HP-PPF approach, implemented within a dual-loop architecture alongside a PID tracking controller, demonstrates improved disturbance rejection, noise suppression, and robustness against model uncertainties compared to traditional notch filters. It achieves comparable tracking performance to a notch filter-based solution, but demonstrates greater robustness to model uncertainties, making it a more reliable alternative to notch filters. The active damping strategy can be extended to provide effective damping for the second resonance mode of any higher-order system. These contributions were validated experimentally through a proof-of-concept using a single-axis dual-stage compliant positioning system, supported by a mathematical framework that generalizes the findings.

5.2. Recommendations

While the proposed HP-PPF control method has demonstrated clear advantages, further research is needed to address certain trade-offs and explore additional areas for improvement. The following recommendations outline potential directions for future work:

The trade-off between reducing disturbance and noise sensitivity around the parasitic resonance mode and increasing sensitivity at lower frequencies calls for precise tuning of the active damping controller. Instead of focusing solely on open-loop bandwidth, dynamic error budgeting (DEB) for control parameter optimization could be a more effective approach. This approach minimizes the overall error by balancing disturbance rejection and noise amplification, providing a more comprehensive evaluation of control performance [133]. Tuning based on application-specific disturbance and noise profiles could further enhance the controller's performance across diverse environments. Additionally, exploring other optimization techniques could lead to further improvements.

Integrating the HP-PPF damping controller with advanced tracking control methods may also yield significant performance gains. Techniques like reset control [134, 135], or other nonlinear control strategies that mitigate limitations of linear control (such as the waterbed effect), could enhance disturbance rejection and positioning accuracy, especially in high-precision applications.

Although the HP-PPF control method was validated in positioning systems, it has the potential for broader applications in other mechanical systems exhibiting higher-order parasitic resonance modes. Future studies should explore its use in flexible structures and other fields where damping of higher-order modes is critical. Investigating the performance of the HP-PPF method in these diverse applications may uncover new insights into its versatility and further optimize its design for various applications. Tuning the parameters to specific system dynamics could unlock additional performance improvements, particularly in terms of bandwidth, noise suppression, and disturbance rejection.

This research offered a thorough comparison with traditional notch filter-based solutions. However, to fully assess the benefits of the proposed method, future studies should include more extensive comparisons with alternative approaches. This includes vibration control techniques based on modal decomposition [136], as well as the application of optimal control strategies such as H_2 [112] and H_∞ [85, 137]. These approaches provide different perspectives on control performance, potentially revealing further advantages or trade-offs when compared to the proposed method.

Incorporating a non-minimum phase filter within the damping control loop could address some of the limitations associated with the HP-PPF controller. This filter would stabilize the inner damping loop and introduce phase lead, potentially offering improved phase margins and control bandwidth. Exploring the use of such filters could lead to more robust damping solutions with better overall performance, especially in systems where phase margin is critical.

References

- [1] Gordon E Moore. “Lithography and the future of Moore’s law”. In: *Integrated Circuit Metrology, Inspection, and Process Control IX*. Vol. 2439. SPIE. 1995, pp. 2–17.
- [2] Michael Babb. “Extreme motion control”. In: *Computing and Control Engineering* 14.5 (2003), pp. 6–9.
- [3] Gerard de Zwart et al. “Performance of a step-and-scan system for DUV lithography”. In: *Optical Microlithography X*. Vol. 3051. SPIE. 1997, pp. 817–835.
- [4] Enzo Evers, Marc van de Wal, and Tom Oomen. “Beyond decentralized wafer/reticle stage control design: A double-Youla approach for enhancing synchronized motion”. In: *Control Engineering Practice* 83 (2019), pp. 21–32.
- [5] Fazhi Song et al. “Motion Control of Wafer Scanners in Lithography Systems: From Setpoint Generation to Multi-Stage Coordination”. In: *IEEE Transactions on Instrumentation and Measurement* (2024).
- [6] Nader Jalili and Karthik Laxminarayana. “A review of atomic force microscopy imaging systems: application to molecular metrology and biological sciences”. In: *Mechatronics* 14.8 (2004), pp. 907–945.
- [7] Yin Zhang, Haisheng Zhao, and Lijun Zuo. “Contact dynamics of tapping mode atomic force microscopy”. In: *Journal of sound and vibration* 331.23 (2012), pp. 5141–5152.
- [8] Fujun Wang et al. “Design of a piezoelectric-actuated microgripper with a three-stage flexure-based amplification”. In: *IEEE/ASME Transactions on Mechatronics* 20.5 (2014), pp. 2205–2213.
- [9] Sang-Soon Ku et al. “Design, fabrication, and real-time neural network control of a three-degrees-of-freedom nanopositioner”. In: *IEEE/ASME transactions on mechatronics* 5.3 (2000), pp. 273–280.
- [10] Tien-Fu Lu et al. “A three-DOF compliant micromotion stage with flexure hinges”. In: *Industrial Robot: An International Journal* 31.4 (2004), pp. 355–361.
- [11] Sebastian Polit and Jingyan Dong. “Development of a high-bandwidth XY nanopositioning stage for high-rate micro-/nanomanufacturing”. In: *IEEE/ASME Transactions on mechatronics* 16.4 (2010), pp. 724–733.
- [12] L Vaillon and Christian Philippe. “Passive and active microvibration control for very high pointing accuracy space systems”. In: *Smart materials and structures* 8.6 (1999), p. 719.
- [13] Allen J Bronowicki, Nandu S Abhyankar, and Steven F Griffin. “Active vibration control of large optical space structures”. In: *Smart materials and structures* 8.6 (1999), p. 740.
- [14] Xianlei Shan et al. “Residual vibration reduction of high-speed pick-and-place parallel robot using input shaping”. In: *Chinese Journal of Mechanical Engineering* 35.1 (2022), p. 16.
- [15] Yingxiang Liu, Jie Deng, and Qi Su. “Review on multi-degree-of-freedom piezoelectric motion stage”. In: *IEEE Access* 6 (2018), pp. 59986–60004.
- [16] S Hassan HosseinNia and Niranjan Saikumar. “Fractional-order precision motion control for mechatronic applications”. In: *Handbook of Fractional Calculus with Applications* 6 (2019), pp. 339–356.
- [17] Santosh Devasia, Evangelos Eleftheriou, and SO Reza Moheimani. “A survey of control issues in nanopositioning”. In: *IEEE Transactions on Control Systems Technology* 15.5 (2007), pp. 802–823.
- [18] Arnfinn A Eielsen et al. “Damping and tracking control schemes for nanopositioning”. In: *IEEE/ASME Transactions on Mechatronics* 19.2 (2013), pp. 432–444.

- [19] Piyu Wang and Qingsong Xu. “Design of a flexure-based constant-force XY precision positioning stage”. In: *Mechanism and Machine Theory* 108 (2017), pp. 1–13.
- [20] Qingsong Xu. “Design and development of a compact flexure-based XY precision positioning system with centimeter range”. In: *IEEE Transactions on Industrial Electronics* 61.2 (2013), pp. 893–903.
- [21] Jan Holterman and WA Groen. *An Introduction to piezoelectric materials and applications*. Stichting Applied Piezo, 2013.
- [22] Runze Ding et al. “An optimal actuator placement method for direct-drive stages to maximize control bandwidth”. In: *IECON 2020 The 46th Annual Conference of the IEEE Industrial Electronics Society*. IEEE. 2020, pp. 556–561.
- [23] Jan Holterman. “Vibration control of high-precision machines with active structural elements”. In: (2002).
- [24] André Preumont. *Vibration control of active structures: an introduction*. Vol. 246. Springer, 2018.
- [25] A.M. Natu, M.B. Kaczmarek, and S.H. HosseinNia. “Overactuation for Active Damping in Compliant Positioning Stage using Piezoelectric Transducers”. In: *IFAC-PapersOnLine* 58.7 (2024). 4th IFAC Conference on Advances in Proportional-Integral-Derivate Control PID 2024, pp. 269–274. ISSN: 2405-8963. DOI: <https://doi.org/10.1016/j.ifacol.2024.08.073>. URL: <https://www.sciencedirect.com/science/article/pii/S2405896324007912>.
- [26] Yoshifumi Kawamoto et al. “The Outlook for Semiconductor Processes and Manufacturing Technologies in the 0.1- μm Age”. In: *Hitachi Review* 48.6 (1999), p. 335.
- [27] Jiadong Zhang et al. “Recent advancements in artificial intelligence for breast cancer: Image augmentation, segmentation, diagnosis, and prognosis approaches”. In: *Seminars in Cancer Biology*. Elsevier. 2023.
- [28] John Thompson et al. “5G wireless communication systems: Prospects and challenges [Guest Editorial]”. In: *IEEE communications Magazine* 52.2 (2014), pp. 62–64.
- [29] Eric Aboussouan and Sylvain Martel. “High-precision absolute positioning of medical instruments in MRI systems”. In: *2006 International Conference of the IEEE Engineering in Medicine and Biology Society*. IEEE. 2006, pp. 743–746.
- [30] Christine Connolly. “Precision assembly systems for medical devices”. In: *Assembly Automation* 29.4 (2009), pp. 326–331.
- [31] Jean-Philippe Bacher, Cédric Joseph, and Reymond Clavel. “Flexures for high precision robotics”. In: *Industrial Robot: An International Journal* 29.4 (2002), pp. 349–353.
- [32] Amirhossein Sajadi et al. “Integration of renewable energy systems and challenges for dynamics, control, and automation of electrical power systems”. In: *Wiley Interdisciplinary Reviews: Energy and Environment* 8.1 (2019), e321.
- [33] R Munnig Schmidt, Georg Schitter, and Adrian Rankers. *The design of high performance mechatronics: high-Tech functionality by multidisciplinary system integration*. Ios Press, 2020.
- [34] Rabih Alkhatib and MF Golnaraghi. “Active structural vibration control: a review”. In: *Shock and Vibration Digest* 35.5 (2003), p. 367.
- [35] Georg Schitter, Philipp J Thurner, and Paul K Hansma. “Design and input-shaping control of a novel scanner for high-speed atomic force microscopy”. In: *Mechatronics* 18.5-6 (2008), pp. 282–288.
- [36] Jeffrey A Butterworth, Lucy Y Pao, and Daniel Y Abramovitch. “Analysis and comparison of three discrete-time feedforward model-inverse control techniques for nonminimum-phase systems”. In: *Mechatronics* 22.5 (2012), pp. 577–587.
- [37] Makoto Iwasaki, Kenta Seki, and Yoshihiro Maeda. “High-precision motion control techniques: A promising approach to improving motion performance”. In: *IEEE Industrial Electronics Magazine* 6.1 (2012), pp. 32–40.
- [38] Maarten Steinbuch and Meindert L Norg. “Advanced motion control: An industrial perspective”. In: *European Journal of Control* 4.4 (1998), pp. 278–293.

- [39] Guo-Ying Gu and Li-Min Zhu. “Motion control of piezoceramic actuators with creep, hysteresis and vibration compensation”. In: *Sensors and Actuators A: Physical* 197 (2013), pp. 76–87.
- [40] Yidan Tao et al. “High-bandwidth tracking control of piezoactuated nanopositioning stages via active modal control”. In: *IEEE Transactions on Automation Science and Engineering* 19.4 (2021), pp. 2998–3006.
- [41] Daniel Y Abramovitch, Storrs Hoen, and Richard Workman. “Semi-automatic tuning of PID gains for atomic force microscopes”. In: *2008 American Control Conference*. IEEE. 2008, pp. 2684–2689.
- [42] D.J. Mead. *Passive Vibration Control*. John Wiley Sons, 1998.
- [43] Benjamin M Shafer. “An overview of constrained-layer damping theory and application”. In: *Proceedings of Meetings on Acoustics*. Vol. 19. 1. AIP Publishing. 2013.
- [44] Kees Verbaan, Nick Rosielle, and Maarten Steinbuch. “Bandwidth increase by shaping the plant in combination with the controller—The role of damping in positioning tables”. In: *2013 IEEE International Conference on Control Applications (CCA)*. IEEE. 2013, pp. 1099–1104.
- [45] Thomas van der Graaf. “Active Vibration Control: using over-sensing and over-actuation”. In: (2021).
- [46] Vineet Sethi, Matthew A Franchek, and Gangbing Song. “Multimodal active vibration suppression of a flexible structure by loop shaping”. In: *Smart Structures and Materials 2005: Smart Structures and Integrated Systems*. Vol. 5764. SPIE. 2005, pp. 348–359.
- [47] Marcin B Kaczmarek and Hassan HosseinNia. “Fractional-Order Negative Position Feedback for Vibration Attenuation”. In: *Fractal and Fractional* 7.3 (2023), p. 222.
- [48] Mark J Balas. “Direct velocity feedback control of large space structures”. In: *Journal of guidance and control* 2.3 (1979), pp. 252–253.
- [49] Sumeet S Aphale, Andrew J Fleming, and SO Reza Moheimani. “Integral resonant control of collocated smart structures”. In: *Smart materials and structures* 16.2 (2007), p. 439.
- [50] Andrew J Fleming. “Nanopositioning system with force feedback for high-performance tracking and vibration control”. In: *IEEE/Asme Transactions on Mechatronics* 15.3 (2009), pp. 433–447.
- [51] SO Reza Moheimani and Benjamin JG Vautier. “Resonant control of structural vibration using charge-driven piezoelectric actuators”. In: *IEEE Transactions on control systems technology* 13.6 (2005), pp. 1021–1035.
- [52] CJ Goh and TK Caughey. “On the stability problem caused by finite actuator dynamics in the collocated control of large space structures”. In: *International Journal of Control* 41.3 (1985), pp. 787–802.
- [53] Bharath Bhikkaji et al. “High-performance control of piezoelectric tube scanners”. In: *IEEE Transactions on Control Systems Technology* 15.5 (2007), pp. 853–866.
- [54] Linlin Li et al. “Positive acceleration, velocity and position feedback based damping control approach for piezo-actuated nanopositioning stages”. In: *Mechatronics* 47 (2017), pp. 97–104.
- [55] Jeffrey Dosch, Donald Leo, and Daniel Inman. “Modeling and control for vibration suppression of a flexible active structure”. In: *Journal of Guidance, Control, and Dynamics* 18.2 (1995), pp. 340–346.
- [56] Sang-Myeong Kim, Semyung Wang, and Michael J Brennan. “Comparison of negative and positive position feedback control of a flexible structure”. In: *Smart Materials and Structures* 20.1 (2010), p. 015011.
- [57] Xiangyuan Wang et al. “Simultaneous damping and tracking control of a normal-stressed electromagnetic actuated nano-positioning stage”. In: *Sensors and Actuators A: Physical* 338 (2022), p. 113467.
- [58] Zi-Hui Zhu et al. “Triaxial fast tool servo using hybrid electromagnetic–piezoelectric actuation for diamond turning”. In: *IEEE Transactions on Industrial Electronics* 69.2 (2021), pp. 1728–1738.

- [59] Andrew J Fleming, Sumeet S Aphale, and SO Reza Moheimani. “A new method for robust damping and tracking control of scanning probe microscope positioning stages”. In: *IEEE Transactions on nanotechnology* 9.4 (2009), pp. 438–448.
- [60] Yuen Kuan Yong, Sumeet S Aphale, and SO Reza Moheimani. “Design, identification, and control of a flexure-based XY stage for fast nanoscale positioning”. In: *IEEE Transactions on Nanotechnology* 8.1 (2008), pp. 46–54.
- [61] Bayan Babakhani and Theo JA de Vries. “Active damping of the 1D rocking mode”. In: *2010 IEEE International Conference on Mechatronics and Automation*. IEEE. 2010, pp. 1370–1375.
- [62] Jan Holterman and Theo JA De Vries. “Active damping within an advanced microlithography system using piezoelectric smart discs”. In: *Mechatronics* 14.1 (2004), pp. 15–34.
- [63] Yik R Teo et al. “Optimal integral force feedback and structured PI tracking control: Application for objective lens positioner”. In: *Mechatronics* 24.6 (2014), pp. 701–711.
- [64] IA Mahmood and SO Moheimani. “Making a commercial atomic force microscope more accurate and faster using positive position feedback control”. In: *Review of Scientific Instruments* 80.6 (2009).
- [65] Jerzy Warminski et al. “Active suppression of nonlinear composite beam vibrations by selected control algorithms”. In: *Communications in Nonlinear Science and Numerical Simulation* 16.5 (2011), pp. 2237–2248.
- [66] Giovanni Ferrari and Marco Amabili. “Active vibration control of a sandwich plate by non-collocated positive position feedback”. In: *Journal of Sound and Vibration* 342 (2015), pp. 44–56.
- [67] Sumeet S Aphale, Bharath Bhikkaji, and SO Reza Moheimani. “Minimizing scanning errors in piezoelectric stack-actuated nanopositioning platforms”. In: *IEEE Transactions on Nanotechnology* 7.1 (2008), pp. 79–90.
- [68] Jie Ling et al. “Bandwidth enhancement in damping control for piezoelectric nanopositioning stages with load uncertainty: Design and implementation”. In: *Journal of Vibration and Control* 27.11-12 (2021), pp. 1382–1394.
- [69] Sajal K Das, Hemanshu R Pota, and Ian R Petersen. “Damping controller design for nanopositioners: A mixed passivity, negative-imaginary, and small-gain approach”. In: *IEEE/ASME Transactions on Mechatronics* 20.1 (2014), pp. 416–426.
- [70] Guo-Ying Gu et al. “Motion control of piezoelectric positioning stages: modeling, controller design, and experimental evaluation”. In: *IEEE/ASME Transactions on Mechatronics* 18.5 (2012), pp. 1459–1471.
- [71] Bayan Babakhani, Theo JA de Vries, and Job van Amerongen. “A comparison of the performance improvement by collocated and noncollocated active damping in motion systems”. In: *IEEE/ASME transactions on mechatronics* 18.3 (2012), pp. 905–913.
- [72] SM Seltzer et al. *An application of high authority/low authority control and positivity*. Tech. rep. 1988.
- [73] Sang-Myeong Kim and Jae-Eung Oh. “A modal filter approach to non-collocated vibration control of structures”. In: *Journal of Sound and Vibration* 332.9 (2013), pp. 2207–2221.
- [74] André Preumont et al. “Spatial filters in structural control”. In: *Journal of sound and vibration* 265.1 (2003), pp. 61–79.
- [75] Jinjun Jiang et al. “Active vibration control based on modal controller considering structure-actuator interaction”. In: *Journal of Mechanical Science and Technology* 32 (2018), pp. 3515–3521.
- [76] Aleksandr V Fedotov. “Shape control and modal control strategies for active vibration suppression of a cantilever beam”. In: *International Summer School-Conference “Advanced Problems in Mechanics”*. Springer. 2020, pp. 234–244.
- [77] Robbert van Herpen et al. “Exploiting additional actuators and sensors for nano-positioning robust motion control”. In: *Mechatronics* 24.6 (2014), pp. 619–631.

- [78] Aditya Natu. “Overactuation for Active Damping in Compliant Positioning Stage using Piezoelectric Transducers”. In: (2023).
- [79] Ager Paul, Ibrahim Küçükdemiral, and Geraint Bevan. “Improving Positioning Performance of Positive Position Feedback Scheme with Delay Compensation”. In: *2023 9th International Conference on Control, Decision and Information Technologies (CoDIT)*. IEEE. 2023, pp. 809–815.
- [80] Zhong Chen et al. “Damping-enabling technologies for broadband control of piezo-stages: A survey”. In: *Annual Reviews in Control* 52 (2021), pp. 120–134.
- [81] Iskandar A Mahmood, SO Reza Moheimani, and Bharath Bhikkaji. “Precise tip positioning of a flexible manipulator using resonant control”. In: *IEEE/ASME Transactions on Mechatronics* 13.2 (2008), pp. 180–186.
- [82] Giovanni Cherubini et al. “Control methods in data-storage systems”. In: *IEEE Transactions on control systems technology* 20.2 (2011), pp. 296–322.
- [83] Ian R Petersen and Himanshu R Pota. “Minimax LQG optimal control of a flexible beam”. In: *Control Engineering Practice* 11.11 (2003), pp. 1273–1287.
- [84] Dunant Halim and SO Moheimani. “Spatial control of a piezoelectric laminate beam: experimental implementation”. In: (2002).
- [85] Dunant Halim and SO Reza Moheimani. “Experimental implementation of spatial H/sub/spl infin//control on a piezoelectric-laminate beam”. In: *IEEE/Asme Transactions On Mechatronics* 7.3 (2002), pp. 346–356.
- [86] Robert L Clark, William R Saunders, and Gary P Gibbs. *Adaptive structures: dynamics and control*. 2001.
- [87] Qibo Mao and Stanislaw Pietrzko. *Control of noise and structural vibration*. Springer, 2013.
- [88] SO Reza Moheimani and Andrew J Fleming. *Piezoelectric transducers for vibration control and damping*. Springer Science & Business Media, 2006.
- [89] SO Reza Moheimani, Benjamin JG Vautier, and Bharath Bhikkaji. “Experimental implementation of extended multivariable PPF control on an active structure”. In: *IEEE Transactions on Control Systems Technology* 14.3 (2006), pp. 443–455.
- [90] Yik R Teo and Andrew J Fleming. “Optimal integral force feedback for active vibration control”. In: *Journal of Sound and Vibration* 356 (2015), pp. 20–33.
- [91] Douglas Russell, Andrew J Fleming, and Sumeet S Aphale. “Simultaneous optimization of damping and tracking controller parameters via selective pole placement for enhanced positioning bandwidth of nanopositioners”. In: *Journal of Dynamic Systems, Measurement, and Control* 137.10 (2015), p. 101004.
- [92] RL Clark. “Accounting for out-of-bandwidth modes in the assumed modes approach: Implications on colocated output feedback control”. In: (1997).
- [93] Sumeet S Aphale, Andrew J Fleming, and SO Moheimani. “A second-order controller for resonance damping and tracking control of nanopositioning systems”. In: *Proc. of the International Conference on Adaptive Structures and Technologies, Ascona, Switzerland*. 2008.
- [94] Mohammad Namavar et al. “An analytical approach to integral resonant control of second-order systems”. In: *IEEE/ASME Transactions on Mechatronics* 19.2 (2013), pp. 651–659.
- [95] B Bhikkaji and SO Reza Moheimani. “Integral resonant control of a piezoelectric tube actuator for fast nanoscale positioning”. In: *IEEE/ASME Transactions on mechatronics* 13.5 (2008), pp. 530–537.
- [96] Luca Marinangeli, Farbod Alijani, and S Hassan HosseinNia. “Fractional-order positive position feedback compensator for active vibration control of a smart composite plate”. In: *Journal of Sound and Vibration* 412 (2018), pp. 1–16.
- [97] Gabriele Cazzulani et al. “Negative derivative feedback for vibration control of flexible structures”. In: *Smart Materials and Structures* 21.7 (2012), p. 075024.

- [98] James L Fanson. “An experimental investigation of vibration suppression in large space structures using positive position feedback”. PhD thesis. California Institute of Technology, 1987.
- [99] Moon-Kyu Kwak, Sang-Bo Han, and Seok Heo. “The stability conditions, performance and design methodology for the positive position feedback controller”. In: *Transactions of the Korean Society for Noise and Vibration Engineering* 14.3 (2004), pp. 208–213.
- [100] Changjoo Shin, Chinsuk Hong, and Weui Bong Jeong. “Active vibration control of clamped beams using positive position feedback controllers with moment pair”. In: *Journal of mechanical science and technology* 26 (2012), pp. 731–740.
- [101] G Song, SP Schmidt, and BN Agrawal. “Experimental robustness study of positive position feedback control for active vibration suppression”. In: *Journal of guidance, control, and dynamics* 25.1 (2002), 179a–182.
- [102] Mark McEver and Donald Leo. “Adaptive low-authority control algorithms for precision space structures”. In: *Space Technology Conference and Exposition*. 1999, p. 4585.
- [103] Michael I Friswell and Daniel J Inman. “The relationship between positive position feedback and output feedback controllers”. In: *Smart Materials and Structures* 8.3 (1999), p. 285.
- [104] Ryan Orszulik and Jinjun Shan. “Multi-mode adaptive positive position feedback: An experimental study”. In: *Proceedings of the 2011 American Control Conference*. IEEE. 2011, pp. 3315–3319.
- [105] S Poh and A Baz. “Active control of a flexible structure using a modal positive position feedback controller”. In: *Journal of Intelligent Material Systems and Structures* 1.3 (1990), pp. 273–288.
- [106] A Baz, S Poh, and J Fedor. “Independent modal space control with positive position feedback”. In: (1992).
- [107] A Baz and JONG-TAI HONG. “Adaptive control of flexible structures using modal positive position feedback”. In: *International journal of adaptive control and signal processing* 11.3 (1997), pp. 231–253.
- [108] Ehsan Omid and Nima Mahmoodi. “Hybrid positive feedback control for active vibration attenuation of flexible structures”. In: *IEEE/ASME Transactions on Mechatronics* 20.4 (2014), pp. 1790–1797.
- [109] S Nima Mahmoodi and Mehdi Ahmadian. “Active vibration control with modified positive position feedback”. In: (2009).
- [110] Ehsan Omid and S Nima Mahmoodi. “Multimode modified positive position feedback to control a collocated structure”. In: *Journal of Dynamic Systems, Measurement, and Control* 137.5 (2015), p. 051003.
- [111] Ehsan Omid and S Nima Mahmoodi. “Vibration control of collocated smart structures using H_{∞} modified positive position and velocity feedback”. In: *Journal of Vibration and Control* 22.10 (2016), pp. 2434–2442.
- [112] Ahmad Paknejad et al. “A novel design of positive position feedback controller based on maximum damping and h_2 optimization”. In: *Journal of Vibration and Control* 26.15-16 (2020), pp. 1155–1164.
- [113] Giovanni Ferrari et al. “Active vibration control of a composite sandwich plate”. In: *ASME International Mechanical Engineering Congress and Exposition*. Vol. 46483. American Society of Mechanical Engineers. 2014, V04BT04A075.
- [114] Yongsheng Wu et al. “Compensated positive position feedback for active control of piezoelectric structures”. In: *Journal of Intelligent Material Systems and Structures* 29.3 (2018), pp. 397–410.
- [115] Andres San-Millan, Vicente Feliu-Batlle, and Sumeet S Aphale. “Application of a Fractional Order Integral Resonant Control to increase the achievable bandwidth of a nanopositioner.” In: *IFAC-PapersOnLine* 50.1 (2017), pp. 14539–14544.
- [116] Daniel Feliu-Talegon, A San-Millan, and Vicente Feliu-Batlle. “Fractional-order integral resonant control of collocated smart structures”. In: *Control Engineering Practice* 56 (2016), pp. 210–223.

- [117] ZH Wang and YG Zheng. “The optimal form of the fractional-order difference feedbacks in enhancing the stability of a sdof vibration system”. In: *Journal of Sound and Vibration* 326.3-5 (2009), pp. 476–488.
- [118] Ahmed G Radwan, Ahmed S Elwakil, and Ahmed M Soliman. “On the generalization of second-order filters to the fractional-order domain”. In: *Journal of Circuits, Systems, and Computers* 18.02 (2009), pp. 361–386.
- [119] Sumeet S Aphale, Antoine Ferreira, and SO Reza Moheimani. “A robust loop-shaping approach to fast and accurate nanopositioning”. In: *Sensors and Actuators A: Physical* 204 (2013), pp. 88–96.
- [120] Firdaus E Udwadia, Hubertus Von Bremen, and Phailaung Phohomsiri. “Time-delayed control design for active control of structures: principles and applications”. In: *Structural Control and Health Monitoring: The Official Journal of the International Association for Structural Control and Monitoring and of the European Association for the Control of Structures* 14.1 (2007), pp. 27–61.
- [121] Mei-Ju Yang et al. “High-bandwidth control of nanopositioning stages via an inner-loop delayed position feedback”. In: *IEEE Transactions on Automation Science and Engineering* 12.4 (2015), pp. 1357–1368.
- [122] Chun-Xia Li et al. “Damping control of piezo-actuated nanopositioning stages with recursive delayed position feedback”. In: *IEEE/ASME Transactions on Mechatronics* 22.2 (2016), pp. 855–864.
- [123] S Chatterjee. “Vibration control by recursive time-delayed acceleration feedback”. In: *Journal of Sound and Vibration* 317.1-2 (2008), pp. 67–90.
- [124] Bayan Babakhani and Theo JA de Vries. “On the stability properties of P (I) D-controlled motion systems”. In: *IFAC Proceedings Volumes* 43.18 (2010), pp. 473–477.
- [125] Chang-Ik Kang and Chang-Hwan Kim. “An adaptive notch filter for suppressing mechanical resonance in high track density disk drives”. In: *Microsystem Technologies* 11 (2005), pp. 638–652.
- [126] Shang-Teh Wu, Sing-Han Lian, and Sheng-Han Chen. “Vibration control of a flexible beam driven by a ball-screw stage with adaptive notch filters and a line enhancer”. In: *Journal of Sound and Vibration* 348 (2015), pp. 71–87.
- [127] Sachin P Wadikhaye et al. “Control of a piezoelectrically actuated high-speed serial-kinematic AFM nanopositioner”. In: *Smart materials and structures* 23.2 (2014), p. 025030.
- [128] Wei Teng et al. “Iterative tuning notch filter for suppressing resonance in ultra-precision motion control”. In: *Advances in Mechanical Engineering* 8.11 (2016), p. 1687814016674097.
- [129] Gerrit Wijnand van der Poel. “An exploration of active hard mount vibration isolation for precision equipment”. In: (2010).
- [130] MA Beijen et al. “Self-tuning MIMO disturbance feedforward control for active hard-mounted vibration isolators”. In: *Control engineering practice* 72 (2018), pp. 90–103.
- [131] ST Spanjer and WBJ Hakvoort. “Optimal Active Vibration Isolation System Design using Constrained H2 control.” In: *IFAC-papersonline* 55.27 (2022), pp. 160–165.
- [132] Sigurd Skogestad and Ian Postlethwaite. *Multivariable feedback control: analysis and design*. John Wiley & sons, 2005.
- [133] Wouter Monkhorst. “Dynamic error budgeting: A design approach”. In: (2004).
- [134] Nima Karbasizadeh and S Hassan HosseinNia. “Continuous reset element: Transient and steady-state analysis for precision motion systems”. In: *Control Engineering Practice* 126 (2022), p. 105232.
- [135] Orhan Beker, Christopher V Hollot, and Yossi Chait. “Plant with integrator: an example of reset control overcoming limitations of linear feedback”. In: *IEEE Transactions on Automatic Control* 46.11 (2001), pp. 1797–1799.
- [136] AK Belyaev et al. “Experimental study of local and modal approaches to active vibration control of elastic systems”. In: *Structural Control and Health Monitoring* 25.2 (2018), e2105.

-
- [137] Guoying Zhao et al. “ H_∞ optimization of positive position feedback control for mitigation of nonlinear vibrations”. In: *ISMA 2018-28th international conference on Noise and Vibration Engineering*. KU Leuven, Leuven, Belgium. 2018.

A

A.1. Experimental Setup

The experimental setup used in this research is illustrated in Figure A.1, with the main components labeled. This setup was previously employed in studies on active damping through overactuation [25], where its components and software are described in detail [78]. This appendix focuses on the modifications made to both the setup and its software. For a more comprehensive description of the setup, please refer to [78].

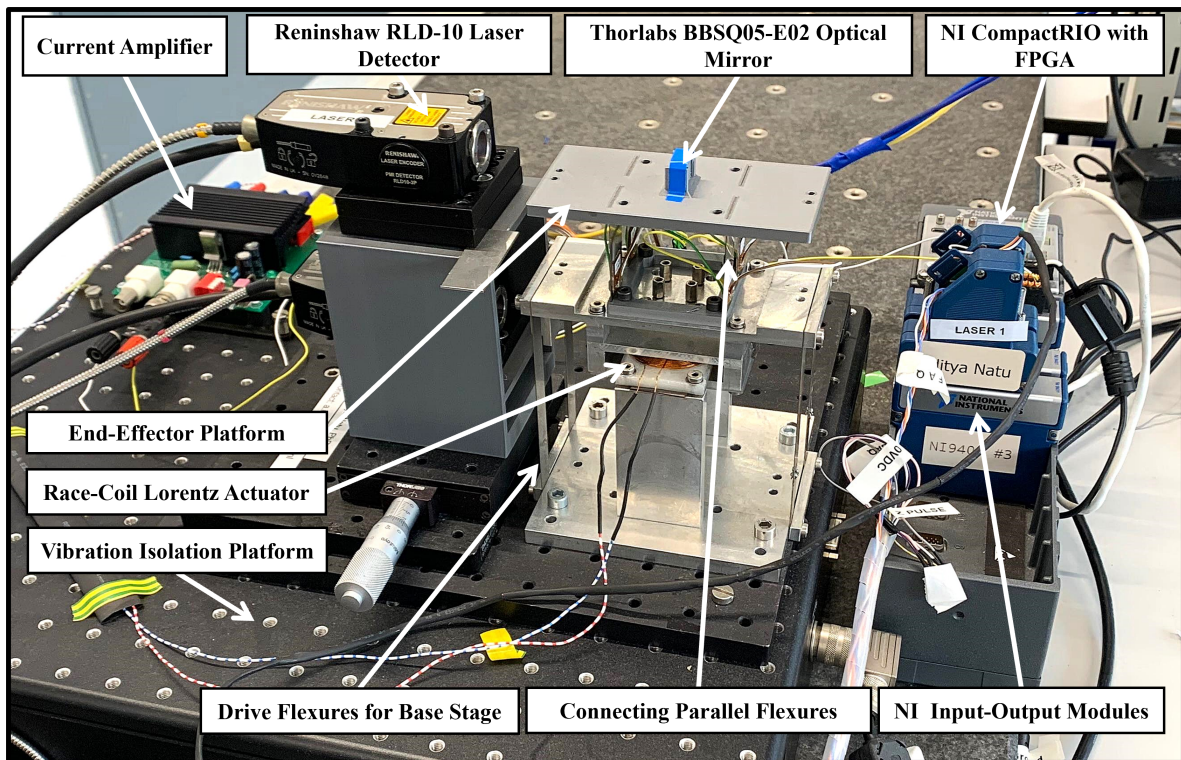


Figure A.1: Experimental Setup

In [78], piezo transducers were attached to the flexures between the base stage and the end-effector stage for active vibration control. To avoid significant changes to the experimental setup, these transducers remain on the flexures in this research, though they are not in use. The transducers are disconnected from both the voltage amplifier and the CompactRIO controller. While the bonded piezo patches slightly affect the stiffness of the flexures and the resonance frequencies, accurate frequency response

measurements were obtained through system identification. Therefore, the unused piezo patches do not interfere with the current research setup.

A.2. LabVIEW Project

This section provides an overview of the real-time control implementation and data acquisition using LabVIEW, focusing specifically on the modifications made to the LabVIEW project. For additional details, refer to [78]. The LabVIEW project is centered around three key Virtual Instrument (vi) files: FPGA.vi, RT_Main.vi, and Host.vi, which are discussed in the following subsections.

A.2.1. FPGA.vi

The FPGA.vi file contains the complete signal generation and control algorithm, running on the CompactRIO chassis with the integrated FPGA, and is compiled using the Xilinx compiler. Any modifications to this file require recompilation, which typically takes 15-30 minutes. Therefore, it is important to plan changes carefully to minimize recompilation time.

This section outlines the modifications made to the FPGA file from [78] for implementing High-Pass Positive Position Feedback (HP-PPF). For details on data collection using the FPGA, please refer to [78].

Measurement Data to FIFO

In LabVIEW, input and output signals are written to a First-In, First-Out (FIFO) structure for real-time data acquisition and synchronization, as shown in Figure A.2. The signals are stored in onboard FIFO memory and later saved to a file. Actuator signals are sent to the NI 9264 Analog Output Module, with data converted to I16 (16-bit integer) format, as required by the module's configuration.

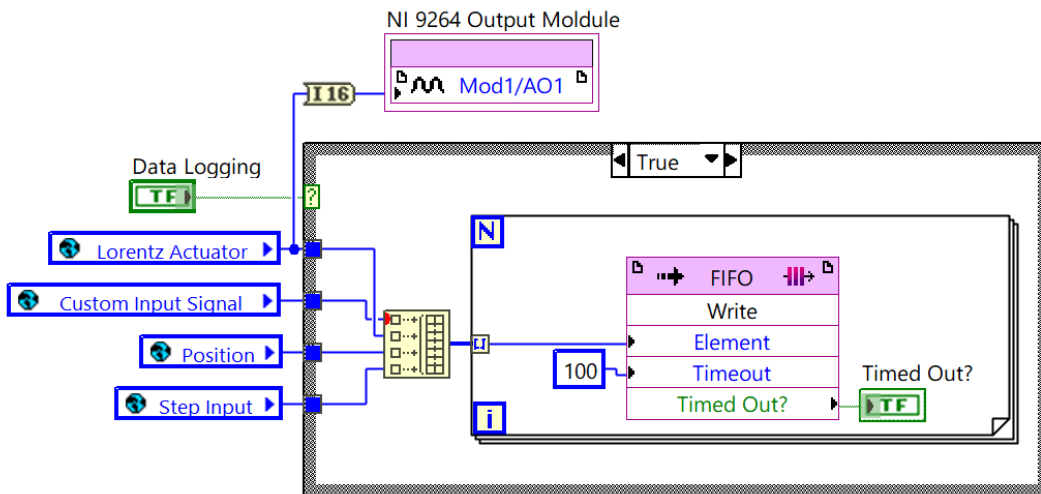


Figure A.2: LabVIEW block diagram for writing measurement data to FIFO

Dual-Loop Control Architecture

The proposed HP-PPF active damping control is implemented on the experimental setup following the dual-loop control architecture depicted in Figure A.3. This architecture combines active damping and tracking control, utilizing the same actuator and position sensor.

The LabVIEW implementation of this architecture is shown in Figure A.4. This diagram allows for several inputs in the control loop that can be selected using the Boolean operators. The diagram outputs a voltage signal sent to the actuator: *Lorentz Actuator*, and uses the measured position signal to close the loop. When the Boolean *Open Loop* is set to true, the position feedback is disabled, enabling open-loop identification.

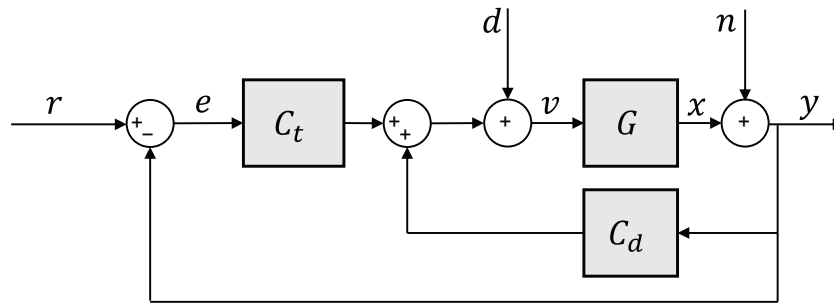


Figure A.3: Schematic block diagram of dual-loop control architecture combining motion control C_t and active damping control C_d

The diagram also supports step reference signals through the *Step Up* parameter, with adjustable amplitude. The *Step Down* parameter is typically set to zero. To activate the step signal for reference tracking, the *Step ON* Boolean must be set to true.

Additionally, a custom reference signal can be selected by setting the *Custom Reference* Boolean to true. Disturbance and noise inputs can be activated via the *Process Disturbance* and *Output Disturbance* Booleans. By selecting *Chirp to Plant*, a custom signal is sent directly to the plant for system identification without controller measurements. The *Lorentz Direct* operator allows direct input to the Lorentz actuator for testing purposes.

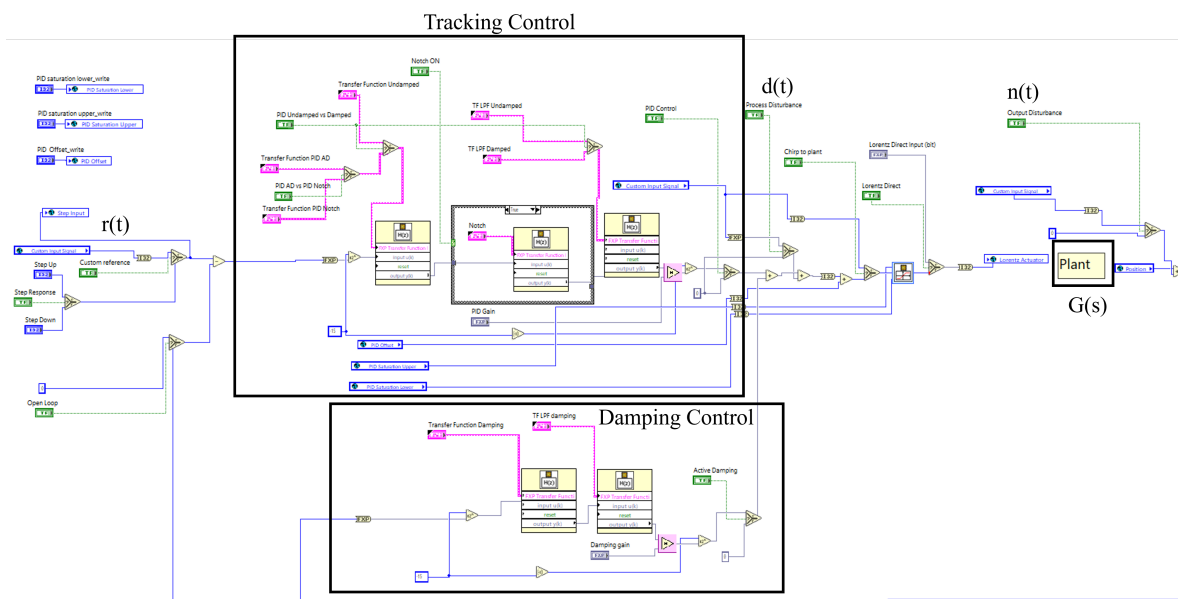


Figure A.4: LabVIEW block diagram for dual-loop control architecture

Tracking Control

The LabVIEW code implementing tracking control is shown in Figure A.5. The input signal is the error between the measured position and the optional reference signal. This error passes through a digitally implemented PID controller when the *PID Control* Boolean is set to true. If the *Notch ON* Boolean is enabled, the signal also passes through a digitally implemented notch filter, followed by a low-pass filter for noise reduction.

The Booleans *PID Undamped vs Damped* and *PID AD vs PID Notch* allow selection between different PID controllers, each tuned for different cases: undamped (no peak attenuation), with the notch filter, or with active damping control. To ensure safe operation, saturation limits are applied to prevent excessive motion of the system masses and avoid overheating of the race track coil actuator, keeping

the control output within a predefined range.

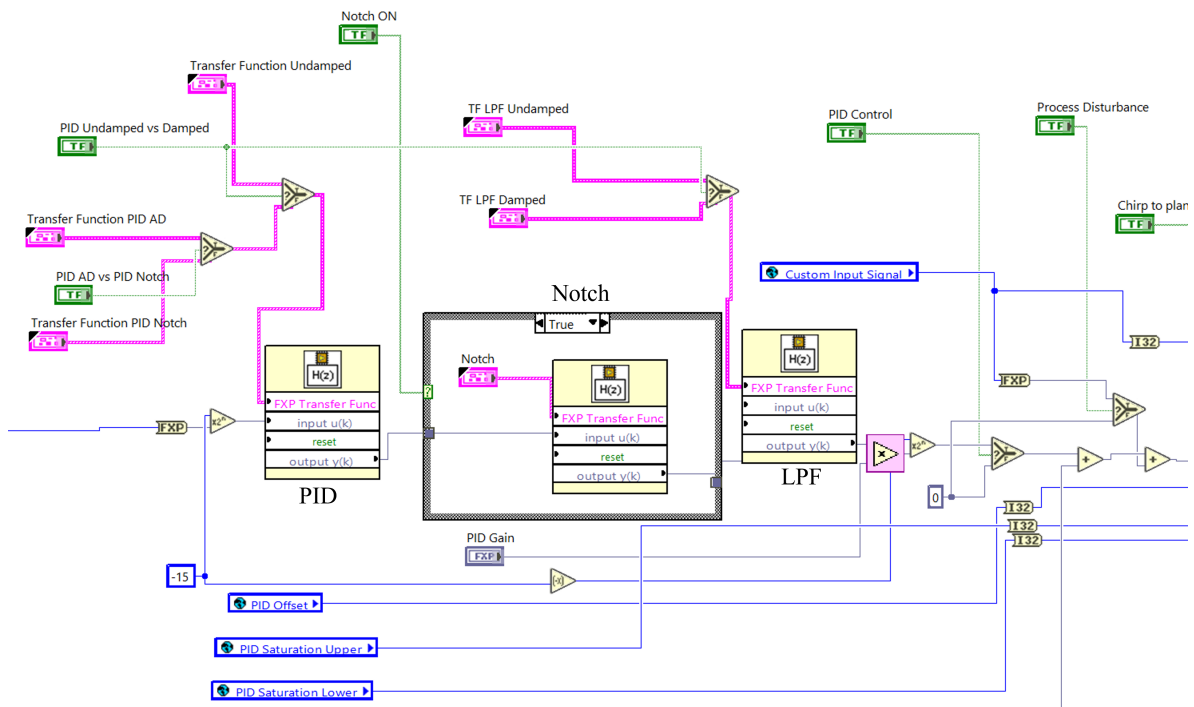


Figure A.5: LabVIEW block diagram for PID tracking control

Active Damping Control

The LabVIEW code implementing active damping control is shown in Figure A.6. The input signal, which is the measured position, is fed back through the digitally implemented active damping controller (HP-PPF). A second-order low-pass filter is added in series for noise attenuation. The active damping loop is enabled by setting the *Active Damping* Boolean to true. The output from this loop is then combined with the motion control loop signal to form the voltage signal sent to the Lorentz actuator.

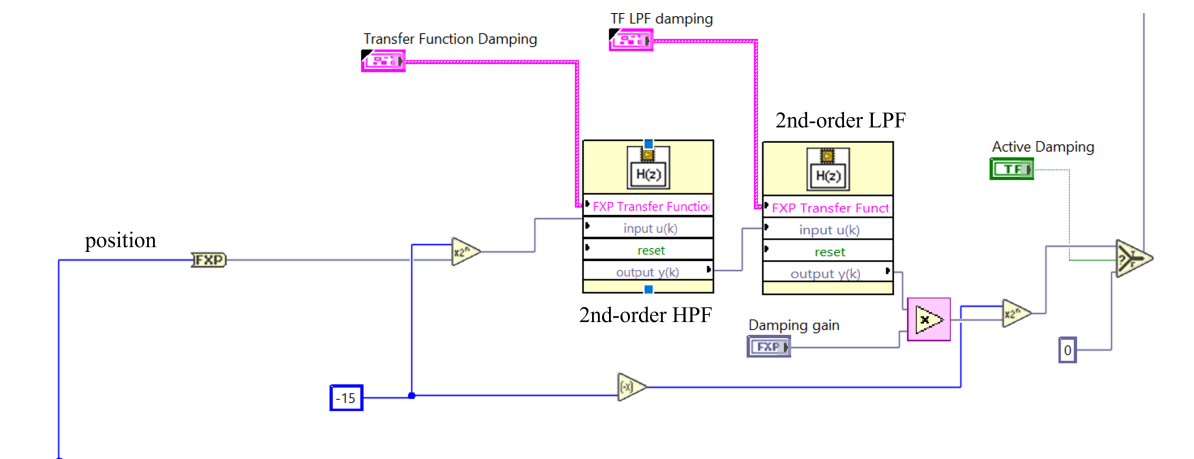


Figure A.6: LabVIEW block diagram for HP-PPF active damping control

Custom Input Signal

The block diagram in Figure A.7 illustrates how a custom FIFO signal from the Host.vi file is implemented in the FPGA and stored in the global variable *Custom Input Signal*. This signal can be utilized as an input at various locations within the control loop, enabling measurements with custom reference

or disturbance signals.

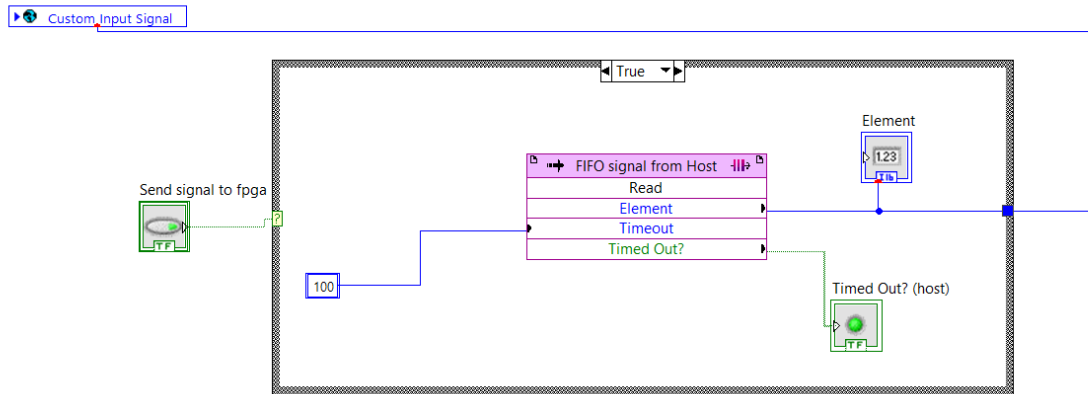


Figure A.7: LabVIEW block diagram for loading FIFO input signal from Host

A.2.2. RT_Main.VI

The RT_Main.vi file acts as the interface between the user’s laptop and the CompactRIO. The project contains a global variable file, 'FPGA_Globals.vi,' which allows shared variables to be accessed across different files in the project. This enables users to easily adjust any variables requiring manual modification through RT_Main.vi. The front panel shown in Figure A.8 displays the user interface of the RT_Main.vi file, allowing manual control of actuators, input signals, and the configuration of key parameters necessary for the effective operation of the FPGA.vi file.

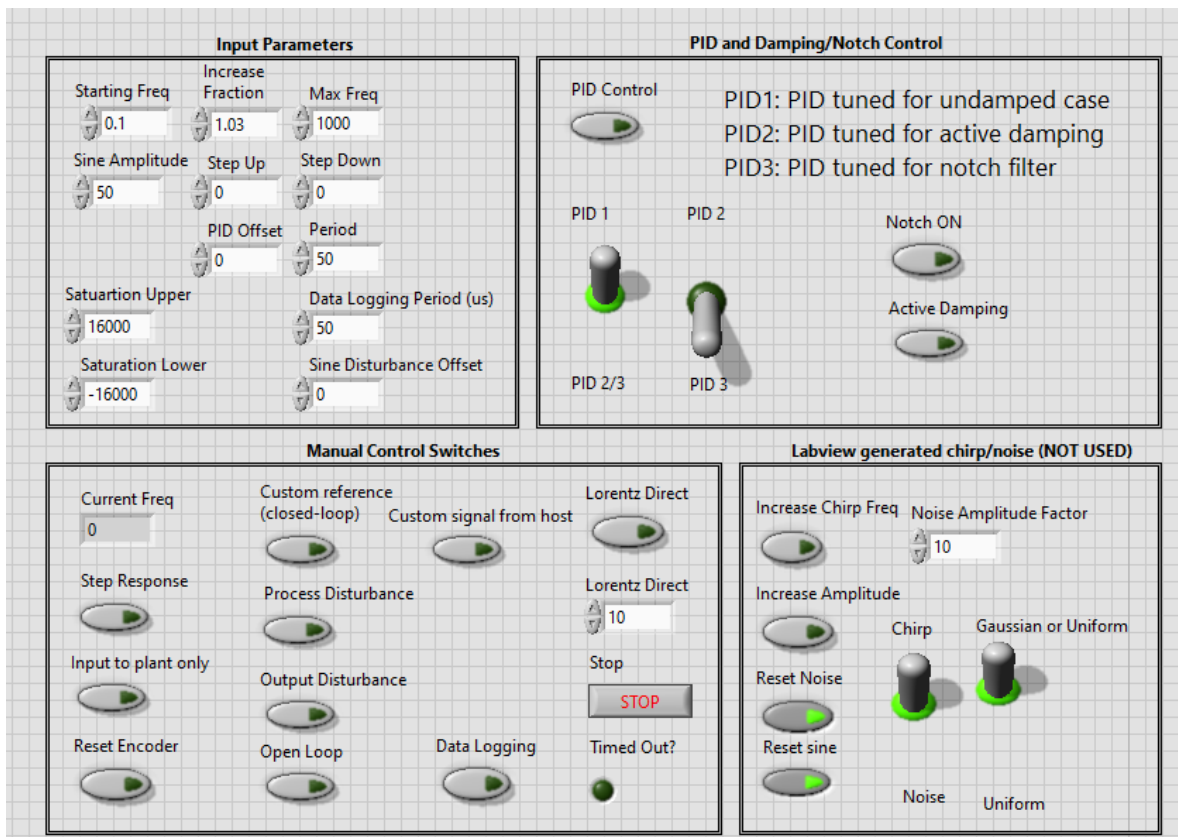


Figure A.8: Control panel of RT_main file in LabVIEW

The control parameters *Starting Freq*, *Increase Fraction*, *Max Freq*, *Sine Amplitude* are part of the LabVIEW code used to generate a chirp signal within LabVIEW, which is not used in this research. For more information, please refer to [78].

- **Data Logging Period** (μs): sets the data logging period in microseconds, which determines the sampling frequency of the experiments.
- **Saturation Upper**: Establishes the upper saturation value in bits for the input signal to the Lorentz actuator.
- **Saturation Lower**: Establishes the lower saturation value in bits for the input signal to the Lorentz actuator.
- **PID Offset**: Specifies the offset value in bits for the PID controller signal.
- **Step Up**: Sets the desired amplitude for the step reference signal.
- **Step Response**: Activates or deactivates the step reference signal with the desired amplitude specified in *Step Up*.
- **Input to plant only**: Sends the custom input signal directly to the plant, to avoid the controllers in the control loop.
- **Reset Encoder**: Sets the measured signal by the encoder to 0.
- **Custom Reference**: Triggers custom signal as reference input to the closed-loop.
- **Process Disturbance**: Triggers custom signal as process disturbance input to the closed-loop.
- **Output Disturbance**: Triggers custom signal as output disturbance input to the closed-loop.
- **Open-Loop**: Disables the position feedback, allowing for open-loop identifications.
- **Custom signal from host**: Takes the custom input signal loaded in the Host.vi.
- **Data Logging**: Determines whether data is logged to the Host.vi file.
- **Lorentz Direct**: Allows for setting a direct voltage signal to the Lorentz actuator.
- **PID Control**: Enables or disables the motion control loop.
- **PID 1/2/3**: Allows for selecting the desired PID controller, which are tuned for different cases.
- **Notch ON**: Enables or disables the notch filter in the motion control loop
- **Active Damping**: Enables or disables the inner damping control loop employing HP-PPF.

The Matlab code below describes the calculation and discretization of the active damping controller, notch filter, and tracking controllers. For details about the implementation in LabVIEW please refer to [78].

```

1  % Load the identified frequency response of the system
2  load('syst_ident_14_06.mat');
3  s = tf('s');
4  G_exp = Gfrd_bit; % Experimental frequency response of system
5
6  % Calculate gain of the system at 1 rad/s
7  zero_gain = abs(freqresp(G_exp, 1, 'rad/s'));
8
9  Fs = 20000; % Sampling frequency
10 ts = 1 / Fs; % Sampling time
11
12 %% Active Damping Controller
13 wn1 = 37; % Frequency of the 1st resonance (rad/s)
14 wn2 = 490; % Frequency of the 2nd resonance (rad/s)
15 n = wn2 / wn1; % Ratio of the resonance frequencies
16
17 % Compensation for system DC gain and spacing between modes
18 gain_compensation = 1 / zero_gain * (n^2 + 2);
19
20 g = 0.2618; % Optimized gain value
21 zeta_HPF = 0.7185; % Optimized damping ratio
22 % High-Pass Filter (HPF) transfer function for HP-PPF active damping placed at
   wn2
23 HPF = -g * gain_compensation * (s^2 / (s^2 + 2 * zeta_HPF * wn2 * s + wn2^2));
24
25 a = 10; % Band-pass width factor
26 zeta_LPF = 0.3; % Damping ratio for the low-pass filter
27 w_LPF = a * wn2; % Corner frequency of the low-pass filter

```

```

28 % Bandpass filter transfer function
29 LPF_bandpass = (w_LPF^2 / (s^2 + 2 * zeta_LPF * w_LPF * s + w_LPF^2));
30
31 % Discretize the continuous-time filters using the Tustin method
32 CdHPF = c2d(HPF, ts, 'tustin');
33 CdLPF_bandpass = c2d(LPF_bandpass, ts, 'tustin');
34
35 % Extract and flip numerator and denominator coefficients
36 HPFnumd = flip(vpa(cell2mat(CdHPF.Numerator), 20));
37 HPFdend = flip(vpa(cell2mat(CdHPF.Denominator), 20));
38
39 LPF_bandpassnumd = flip(vpa(cell2mat(CdLPF_bandpass.Numerator), 20));
40 LPF_bandpassdend = flip(vpa(cell2mat(CdLPF_bandpass.Denominator), 20));
41
42 % Inner closed damping loop transfer function
43 CL_damping = G_exp / (1 - G_exp * CdHPF * CdLPF_bandpass);
44
45 %% Notch Filter
46 omega_N = wn2; % Notch frequency (rad/s)
47 zeta_N = 0.15; % Damping ratio for notch filter
48 Q = 7; % Quality factor
49
50 % Notch filter transfer function
51 numerator_n = [1 2 * zeta_N * omega_N / Q omega_N^2];
52 denominator_n = [1 2 * zeta_N * omega_N omega_N^2];
53 N = tf(numerator_n, denominator_n);
54
55 % Discretize the notch filter
56 CdN = c2d(N, ts, 'tustin');
57
58 % Extract and flip numerator and denominator coefficients for the notch filter
59 Nnumd = flip(vpa(cell2mat(CdN.Numerator), 20));
60 Ndend = flip(vpa(cell2mat(CdN.Denominator), 20));
61
62 %% PID Controller (No Damping)
63 wc = 80; % Optimized bandwidth (rad/s)
64 wi = wc / 10; % Integral bandwidth
65 wd = wc / 3; % Derivative bandwidth
66 wt = 3 * wc; % Tamed derivative bandwidth
67 % Proportional gain for PID controller
68 kp = 0.33 * (1 / abs(freqresp(G_exp, wc, 'rad/s')));
69
70 % Low pass filter after PID
71 LPF = (1 / ((s / (wc * 10)) + 1));
72 % PID controller transfer function
73 PID = -kp * (1 + (wi / (s + 0.001))) * ((s / wd + 1) / (s / wt + 1));
74
75 %% PID Controller with Active Damping
76 wc = 159; % Optimized bandwidth (rad/s)
77 wi = wc / 10;
78 wd = wc / 3;
79 wt = 3 * wc;
80 % Proportional gain for PID controller with damping
81 kp = 0.33 * (1 / abs(freqresp(CL_damping, wc, 'rad/s')));
82
83 % Low pass filter after PID
84 LPF = (1 / ((s / (wc * 10)) + 1));
85 % PID controller transfer function
86 PID = -kp * (1 + (wi / (s + 0.001))) * ((s / wd + 1) / (s / wt + 1));
87
88
89 %% PID Controller with Notch
90 wc = 141; % Bandwidth (rad/s)
91 wi = wc / 10;
92 wd = wc / 3;
93 wt = 3 * wc;
94 % Proportional gain for PID controller with notch
95 kp = 0.33 * (1 / abs(freqresp(G_exp * CdN, wc, 'rad/s')));
96
97 % Low pass filter after PID
98 LPF = (1 / ((s / (wc * 10)) + 1));

```

```

99 % PID controller transfer function
100 PID = -kp * (1 + (wi / (s + 0.001))) * ((s / wd + 1) / (s / wt + 1));
101
102 %% Discretize the PID controller and low pass filter
103 CdPID = c2d(PID, ts, 'tustin');
104 CdLPF = c2d(LPF, ts, 'tustin');
105
106 % Extract and flip numerator and denominator coefficients
107 PIDnumd = flip(vpa(cell2mat(CdPID.Numerator), 20));
108 PIDdend = flip(vpa(cell2mat(CdPID.Denominator), 20));
109
110 LPFnumd = flip(vpa(cell2mat(CdLPF.Numerator), 20));
111 LPFdend = flip(vpa(cell2mat(CdLPF.Denominator), 20));

```

A.2.3. Host.VI

The Host.vi file functions as a tool for observing and storing data collected from the experimental setup. Its front panel, shown in Figure A.9, features multiple waveform charts that provide real-time visualizations of sensor measurements and signals sent to the actuators. The *Save Data* Boolean enables users to save the measurement data to a selected file; for more details, see [78].

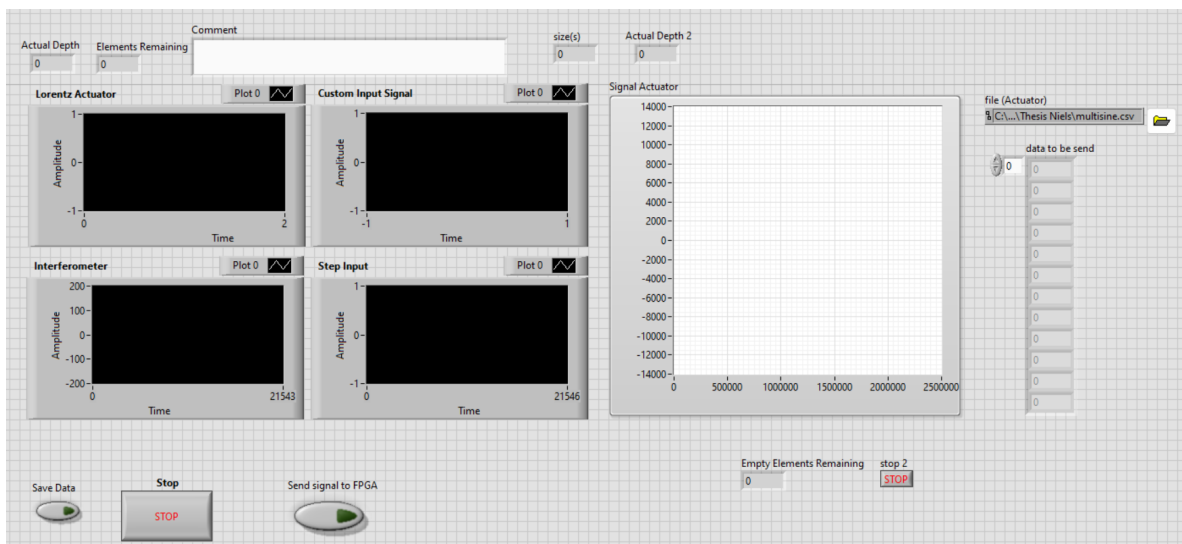


Figure A.9: Front panel of Host.vi file in LabVIEW

The block diagram depicted in Figure A.10 enables signals generated in MATLAB to be loaded into the Host.vi file in LabVIEW. By setting the *Send Signal to FPGA* Boolean to true, these signals can be sent to the FPGA for use as input signals at the desired location. The .csv file location can be selected on the front panel of the Host.vi, which also graphically displays the loaded signal.

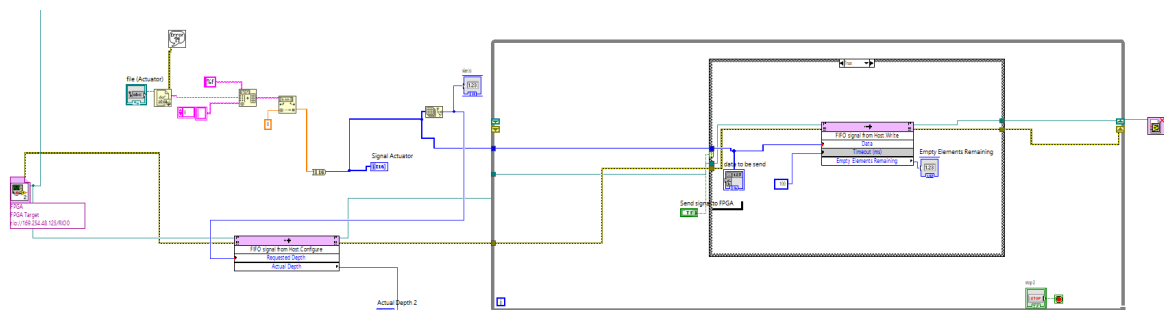


Figure A.10: LabVIEW block diagram in Host.vi to load custom input signals and send to FPGA

The Matlab code below illustrates how a custom multisine signal can be generated and saved as a .csv file, to be loaded in the Host.vi file in LabVIEW. Note that the amplitude of the input signal needs to be scaled to account for the bit values of the signals in LabVIEW.

```
1 fs = 20000; % Sampling frequency (Hz)
2 T = 20; % Duration of the signal (s)
3 N = fs * T; % Number of samples
4 frequencies = [470, 480]; % Frequencies of the sinusoids (rad/s)
5 amplitude_factors = [(2^15)/20, (2^15)/20]; % Amplitudes of the sinusoids in bits
6
7 % Generate time vector
8 t = (0:N-1) / fs;
9
10 % Generate multisine signal
11 multisine = zeros(1, N);
12 for i = 1:length(frequencies)
13     multisine = multisine + (amplitude_factors(i)) * sin(frequencies(i) * t);
14 end
15
16 % Save multisine signal at specified location
17 writematrix(multisine, 'C:\Users\niels\OneDrive - \Thesis\Labview\multisine.csv',
    'Delimiter','tab');
```

A.3. System Identification

Accurate system knowledge is essential for effective control, making system identification a critical component of this research. The identification process was carried out using LabVIEW, where predefined input signals were applied to the actuator, and the resulting time-domain data was measured by the position sensor.

The goal of system identification is to calculate the transfer function by measuring the system's output response to a known input. Achieving a high signal-to-noise (s-to-n) ratio is crucial for obtaining reliable results. While signals such as noise or step inputs can be used, chirp signals have proven to deliver the most accurate system identification. A chirp signal is a sinusoidal wave with a frequency that increases over time A.11a. This characteristic makes it highly effective for system identification since it excites each frequency individually. The signal amplitude can be adjusted to optimize the s-to-n ratio, though it is important to limit the amplitude to avoid over-exciting system modes, which could lead to damage.

In this setup, chirp signals with frequencies ranging from 0.1 to 1000 Hz were employed. The maximum frequency was chosen to be within one-tenth of the sampling frequency to comply with the Nyquist theorem. It was observed that generating chirp signals in MATLAB and importing them into the Host.vi file in LabVIEW produced significantly better s-to-n ratios compared to generating them directly within the LabVIEW FPGA.vi file. The best results were achieved by using four repeated chirp signals with increasing amplitude at higher frequencies accounting for the lower magnitudes in the system's frequency response to further improve the s-to-n ratio.

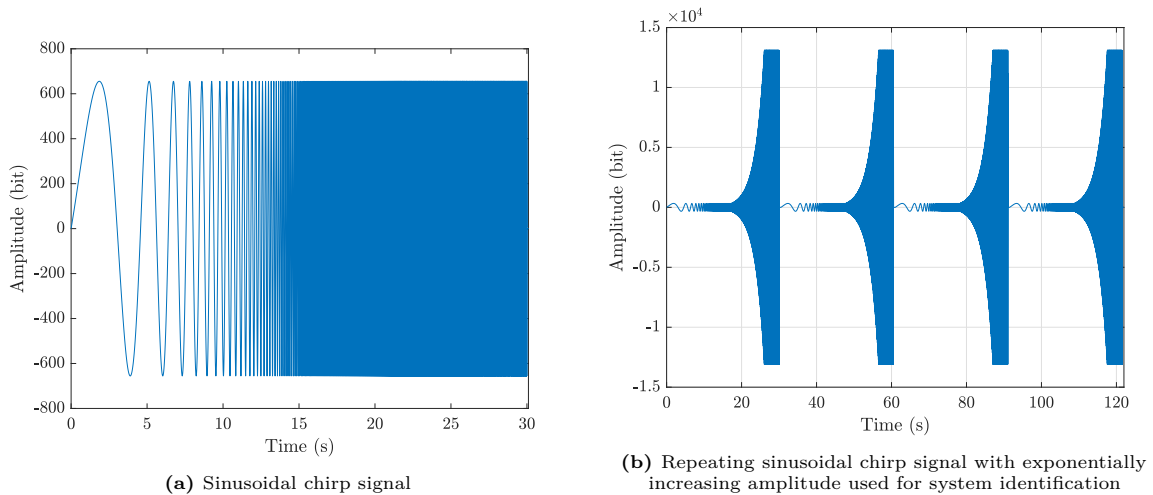


Figure A.11

The repeating chirp signal with increasing amplitude is generated using the MATLAB code shown below:

```

1 % Parameters
2 Fs = 20000; % Sampling frequency (Hz)
3 duration = 30; % Chirp duration (seconds)
4 f0 = 0.1; % Start frequency (Hz)
5 f1 = 1000; % End frequency (Hz)
6 amplitude_start = 2^15 / 100; % Starting amplitude
7 amplitude_end = 2^15 / 2.5; % Ending amplitude
8 f_cutoff = 300; % Cutoff frequency (Hz)
9 interval = 0.5; % Silence interval duration (seconds)
10 n = 4; % Number of repetitions
11
12 % Time vector
13 t = 0:1/Fs:duration;
14 chirp_freq = f0 * exp(log(f1/f0) * t / duration); % Frequency vector
15 amplitude_envelope = amplitude_start * ones(size(t)); % Initialize amplitude
   envelope
16
17 % Find indices for amplitude adjustment
18 start_index = find(chirp_freq > 20, 1); % Start increasing amplitude
19 cutoff_index = find(chirp_freq > f_cutoff, 1); % Stop increasing amplitude
20 % Logarithmic amplitude increase until cutoff frequency
21 if ~isempty(cutoff_index)
22     amplitude_envelope(start_index:cutoff_index) = ...
23         logspace(log10(amplitude_start), log10(amplitude_end), cutoff_index -
   start_index + 1);
24     amplitude_envelope(cutoff_index:end) = amplitude_end; % Constant amplitude
   after cutoff
25 end
26
27 amplitude_envelope(end-15:end) = 0; % Fade out last 15 samples
28 % Generate chirp signal
29 y = amplitude_envelope .* chirp(t, f0, duration, f1, 'logarithmic', -90);
30 % Silence segment
31 silence = zeros(1, Fs * interval);
32 % Create full signal by repeating chirp with silence
33 full_signal = repmat([y, silence], 1, n);
34 % Time vector for full signal
35 t_full = 0:1/Fs:(length(full_signal) - 1) / Fs;
36
37 % Save the signal to a CSV file
38 writematrix(full_signal, 'chirps.csv', 'Delimiter', 'tab'); % Update path as
   needed

```

After collecting the time-domain response data, the system's frequency response was estimated using

MATLAB's *tftestimate* function from the System Identification Toolbox. To reduce noise and improve clarity, a Hanning window was applied during the estimation process. The system's frequency response is illustrated in Figure A.12. The identified transfer function between the input and output values, both in bits, is shown in grey. By converting the bit values of the interferometer's encoder and the current amplifier, and incorporating the dynamics of both the amplifier and actuator, the frequency response in black is derived. This represents the transfer function from the actuator's force input, measured in Newtons (N), to the system's position output in meters (m). The magnitude of the black frequency response converges to -150 dB, which approximately corresponds to the resolution of the interferometer (39.5 nm). The MATLAB code provided below illustrates the system identification process using measured input and output signals, including the conversion of input signals from bits to force and output signals from bits to position.

```

1 load('Input.mat')
2 load('Output.mat')
3 Fs = 2e4;
4 Input_V = Input./(2^15)*10; % From input value in bits to voltage (V)
5 Input_I = Input_V*0.333 + 0.00095; % From voltage to current using amplifier
  dynamics
6 Motor_constant = 1.61; %N/A
7 Input_F = Input_I*Motor_constant; % From input current to force using actuator
  dynamics
8 resolution = 39.5e-9; % resolution of interferometer sensor in m
9 Output_m = Output.*resolution; % From output value in bits to meter (m)
10
11 L = length(Input);
12 wind = hann(L/8); % Hanning window
13 t = L/Fs;
14 time = linspace(0, t, length(Input));
15
16 [Gest, f] = tftestimate(Input_F, Output_m, wind, [], [], Fs);
17 [Gest_bit, ~] = tftestimate(Input, Output, wind, [], [], Fs);
18 coherence = mscohere(Input_F, Output_m, wind, [], [], Fs);
19
20 Gfrd = frd(Gest, f*pi*2, 1/Fs);
21 Gfrd_bit = frd(Gest_bit, 2*pi*f, 1/Fs);
22 Coherence = frd(coherence, 2*pi*f, 1/Fs);

```

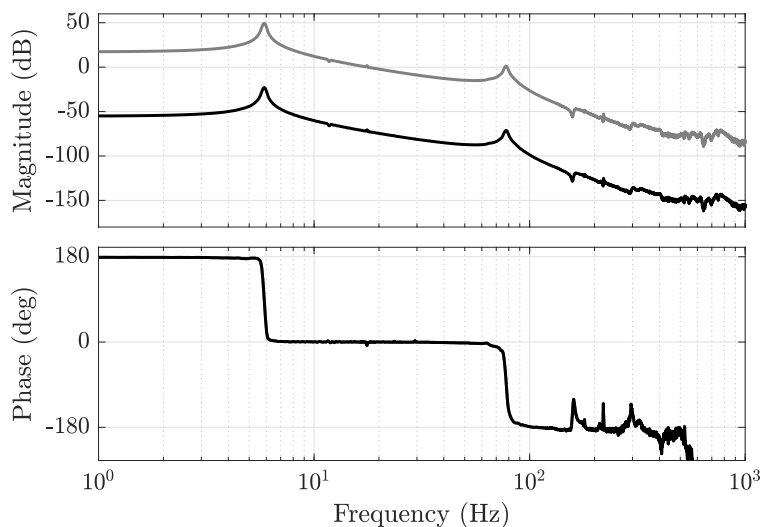


Figure A.12: Identified frequency response of system's transfer function; *bit/bit* in grey and $x[m]/F_a[N]$ in black

B

Optimization Algorithm

To determine the control parameters in the dual-loop control architecture, an optimization algorithm is employed. This algorithm aims to find the optimal values for the active damping controller parameters g_k and ζ_c , as well as the crossover frequency ω_x of the PID controller. The primary goal of the optimization process is to maximize the open-loop bandwidth, represented by the crossover frequency ω_x , while ensuring that the system maintains adequate gain and phase margins. To achieve this, the objective function is normalized by scaling ω_x relative to the frequency of the higher-order parasitic mode ω_2 , making the objective function dimensionless. The optimization problem is formulated as follows:

$$\begin{aligned} \min_{\mathbf{x}} \quad & - \frac{\omega_x(\mathbf{x})}{\omega_2} \\ \text{subject to} \quad & GM(\mathbf{x}) - 6dB \geq 0 \\ & PM(\mathbf{x}) - 30 \geq 0 \\ \text{and} \quad & 0 < g_k < 1 \\ & 0 < \zeta_c < 1 \\ & \omega_1 < \omega_x < \omega_2 \\ \text{where} \quad & \mathbf{x} = (g_k, \zeta_c, \omega_x)^T \\ & |L(\omega_x, \mathbf{x})| = |C_t(\omega_x, \mathbf{x}) \cdot CL_d(\omega_x, \mathbf{x})| = 0 \end{aligned}$$

The accompanying MATLAB script implements this optimization algorithm. Initially, the code defines the system parameters, including the natural frequencies and damping ratios, as well as the bounds for the controller gain g_k , controller damping ratio ζ_c , and crossover frequency ω_x . The objective function, referred to as *Objective_func*, calculates the negative crossover frequency of the closed-loop transfer function, which is the value to be minimized. The constraints are evaluated using the function *ineqcon*, which checks whether the design meets specified stability requirements, such as gain and phase margins.

```
1 % Define system parameters
2 zeta1 = 0.015;           % Damping ratio for mode 1
3 zeta2 = 0.02;           % Damping ratio for mode 2
4 wn1 = 37;               % Natural frequency for mode 1 (rad/s)
5 n = 13.2432;           % Mode spacing factor
6 g_k_bounds = [0.01, 1]; % Bounds for controller gain (g_k)
7 zeta_c_bounds = [0.01, 1]; % Bounds for damping ratio (zeta_c)
8 bw_bounds = [wn1, n * wn1]; % Bounds for bandwidth (crossover frequency)
9 initial_guess = [0.1, 0.1, 60]; % Initial guesses for [g_k, zeta_c, bw]
10
11 % Define minimum phase and gain requirements
12 min_phase = 30;        % Minimum phase margin (degrees)
13 min_gain = 6;          % Minimum gain (dB)
14
15 % Objective function and constraints for optimization
16 objective_function = @(minimizer) Objective_func(minimizer);
```

```

17 constraint_function = @(minimizer) ineqcon(minimizer);
18
19 % Optimization options
20 options = optimoptions('fmincon', 'Algorithm', 'sqp', 'Display', 'iter', '
    MaxFunctionEvaluations', 10e3);
21
22 % Run the optimization process
23 [optimal_params, objective_value, exit_flag, output, lambda, grad, hessian] =
    fmincon( ...
24     objective_function, initial_guess, [], [], [], [], ...
25     [g_k_bounds(1), zeta_c_bounds(1), bw_bounds(1)], ...
26     [g_k_bounds(2), zeta_c_bounds(2), bw_bounds(2)], ...
27     constraint_function, options);
28
29 % Extract optimized parameters
30 g_k = optimal_params(1) % Optimized controller gain
31 zeta_c = optimal_params(2) % Optimized damping ratio
32 bandwidth = optimal_params(3) % Optimized bandwidth
33
34 %% Constraint function for inequality constraints
35 function [inequality_constraints, equality_constraints] = ineqcon(params)
36     n = evalin('base', 'n'); % Retrieve mode spacing factor from base
    workspace
37     wn1 = evalin('base', 'wn1'); % Retrieve natural frequency for mode 1
38     zeta1 = evalin('base', 'zeta1'); % Retrieve damping ratio for mode 1
39     zeta2 = evalin('base', 'zeta2'); % Retrieve damping ratio for mode 2
40
41     g_k = params(1); % Controller gain from optimization
42     zeta_c = params(2); % Damping ratio from optimization
43     bandwidth = params(3); % Bandwidth from optimization
44
45     wn2 = n * wn1; % Second natural frequency
46     wc_c = wn2; % Controller frequency
47     s = tf('s'); % Define Laplace variable
48
49 % Define transfer function of the system
50 G = (wn1^2 * wn2^2) / ((s^2 + 2 * zeta2 * wn2 * s + wn2^2) * (s^2 + 2 * zeta1
    * wn1 * s + wn1^2));
51
52 % Calculate gain correction for active damping controller
53 gain_correction = (n^2 + 4 * zeta1 * zeta2 * n + 4 * zeta1 * zeta_c * n + 4 *
    zeta2 * zeta_c + 2);
54 Cd = gain_correction * (g_k * s^2) / (s^2 + 2 * zeta_c * wc_c * s + wc_c^2);
    % Damping controller
55
56 % Closed-loop transfer function with damping controller
57 L_Cd = Cd * G;
58 CL_Cd = G / (1 - L_Cd);
59
60 % Define bandwidth parameters for PID controller
61 wd = bandwidth / 3;
62 wt = 3 * bandwidth;
63 wi = bandwidth / 10;
64 % Calculate proportional gain for PID controller
65 kp = 0.33 * (1 / abs(evalfr(CL_Cd, bandwidth * j)));
66 w_LPF = 10 * bandwidth;
67 LPF = (1 / ((s / w_LPF) + 1)); % Low-pass filter
68 % Define PID controller
69 C_PID = kp * (1 + (wi / s)) * (((s / wd) + 1) / ((s / wt) + 1)) * LPF;
70
71 % Closed-loop transfer function with PID controller
72 L_Ct = C_PID * CL_Cd;
73 CL_Ct = L_Ct / (1 + L_Ct);
74
75 % Calculate stability margins
76 all_margins = allmargin(L_Ct);
77 phase_margin = all_margins.PhaseMargin(1);
78 gain_margin = max(all_margins.GainMargin);
79 crossover_frequency = all_margins.PMFrequency(1);
80 poles = pole(minreal(CL_Ct));
81

```

```

82 % Inequality constraints
83 g1 = db2mag(min_gain) - gain_margin; % Gain constraint
84 g2 = min_phase - phase_margin; % Phase margin constraint
85 g3 = max(real(poles)); % Pole location constraint for stability
86
87 inequality_constraints = [g1, g2, g3];
88 equality_constraints = 0; % No equality constraints
89 end
90
91 %% Objective function for optimization
92 function [objective_value] = Objective_func(params)
93 bandwidth = params(3); % Bandwidth from optimization
94 zeta_c = params(2); % Damping ratio from optimization
95 g_k = params(1); % Controller gain from optimization
96
97 % Retrieve parameters from base workspace
98 n = evalin('base', 'n');
99 wn1 = evalin('base', 'wn1');
100 zeta1 = evalin('base', 'zeta1');
101 zeta2 = evalin('base', 'zeta2');
102 wn2 = n * wn1;
103 wc_c = wn2;
104 s = tf('s');
105 % Define transfer function of the system
106 G = (wn1^2 * wn2^2) / ((s^2 + 2 * zeta2 * wn2 * s + wn2^2) * (s^2 + 2 * zeta1
    * wn1 * s + wn1^2));
107
108 % Calculate gain correction for controller stability
109 gain_correction = (n^2 + 4 * zeta1 * zeta2 * n + 4 * zeta1 * zeta_c * n + 4 *
    zeta2 * zeta_c + 2);
110 Cd = gain_correction * (g_k * s^2) / (s^2 + 2 * zeta_c * wc_c * s + wc_c^2);
111 % Damping controller
112 % Closed-loop transfer function with damping controller
113 L_Cd = Cd * G;
114 CL_Cd = G / (1 - L_Cd);
115
116 % Define bandwidth parameters for PID controller
117 wd = bandwidth / 3;
118 wt = 3 * bandwidth;
119 wi = bandwidth / 10;
120 % Calculate proportional gain for PID controller
121 kp = 0.33 * (1 / abs(evalfr(CL_Cd, bandwidth * j)));
122 w_LPF = 10 * bandwidth;
123 LPF = (1 / ((s / w_LPF) + 1)); % Low-pass filter
124 % Define PID controller
125 C_PID = kp * (1 + (wi / s)) * (((s / wd) + 1) / ((s / wt) + 1)) * LPF;
126
127 % Closed-loop transfer function with PID controller
128 L_Ct = C_PID * CL_Cd;
129 CL_Ct = L_Ct / (1 + L_Ct);
130
131 % Calculate stability margins
132 all_margins = allmargin(L_Ct);
133 crossover_frequency = all_margins.PMFrequency(1);
134
135 % Objective function value (negative crossover frequency for minimization)
136 objective_value = -crossover_frequency;
137 end

```

One of the primary benefits of Sequential Quadratic Programming (SQP) is its ability to handle complex constraints effectively, often leading to fast convergence to a local optimum. Additionally, it is known for its robustness in providing high-quality solutions in practical applications. However, SQP can be sensitive to the choice of starting points and may struggle with poorly scaled problems or when the objective has many local optima. Therefore, it might be reasonable to consider other optimization algorithms, such as Genetic Algorithms or Particle Swarm Optimization, which can offer more global search capabilities and are less likely to get trapped in local minima, especially in highly nonlinear or complex problem spaces. Employing a combination of different methods or using hybrid algorithms could enhance the optimization process, providing more comprehensive solutions.